LRP 684/00 November 2000

Papers Presented at the 18th IAEA Fusion Energy Conference

Sorrento, Italy, October 19-24, 2000

ISSN 0458-5895

LIST OF CONTENTS

OVERVIEW OF RECENT JET RESULTS

J. Paméla
CRPP co-authors:
F. Hofmann, R.A. Pitts, A. Pochelon, O. Sauter

Overview of TCV Results

H. Weisen, S. Alberti, C. Angioni, K. Appert, J. Bakos[1], R. Behn, P. Blanchard, P. Bosshard, R. Chavan, S. Coda, I. Condrea, A. Degeling, B. P. Duval, D. Fasel, J.-Y. Favez, A. Favre, I. Furno, P. Gomez, T.P. Goodman, M. A. Henderson, F. Hofmann, R.R. Kayruthdinov[2], P. Lavanchy, J. B. Lister, X. Llobet, A. Loarte[3], V.E. Lukash[4], P. Gorgerat, J.-P. Hogge, P.-F. Isoz, B. Joye, J.-C. Magnin, A. Manini, B. Marlétaz, P. Marmillod, Y. Martin, An. Martynov, J.-M. Mayor, E. Minardi[5], J. Mlynar, J.-M. Moret, P. Nikkola, P. J. Paris, A. Perez, Y. Peysson[6], Z.A. Pietrzyk, V. Piffl[7], R.A. Pitts, A. Pochelon, H. Reimerdes, J.H. Rommers, O. Sauter, E. Scavino, A. Sushkov[2], G. Tonetti, M.Q. Tran and A. Zabolotsky

Centre de Recherches en Physique des Plasmas
Association EURATOM-Confédération Suisse
École Polytechnique Fédérale de Lausanne
CH-1015 Lausanne, Switzerland

[1] KFKI, Budapest, HU; [2]RRC, Moscow, RUS; [3]EFDA-CSU, Garching, D;
[4]TRINITI, Troisk, RUS; [5]Istituto di Fisica del Plasma "P.Caldirola", Milano, I;
[6]CEA, Cadarache, F; [7]IPP, Prague, CZ

E-mail address of main author: Henri.Weisen@epfl.ch

Abstract. The TCV tokamak (R=0.88m, a<0.25m, B_T<1.54T) is equipped with six 0.5MW gyrotron sources operating at 82.7 GHz for second harmonic X-mode ECH. By distributing the ECCD current sources over the discharge cross section, fully driven stationary plasmas with I_p=210kA, n_{e0}=2·10^{19}m^{-3}, T_{e0}≈4keV, were obtained for the full discharge duration of 2s. Highly peaked electron temperature profiles with T_{e0} up to 12keV were obtained in central counter current drive scenarios with off-axis ECH. Absorption measurements using a 118 GHz gyrotron have demonstrated the importance of suprathermal electrons for third harmonic absorption. A coupled heat-particle transport phenomenon known as "density pumpout", which leads to the expulsion of particles from the plasma core, has been linked to the presence of m=1 modes, suggesting that it is due to the existence of locally trapped particles associated with the loss of axisymmetry. Highly elongated discharges have been developed with Ohmic heating (κ<2.8) and off-axis ECH. The latter exhibit considerably improved vertical stability due to current profile broadening. A "gateway" for Elmy H-modes has been discovered, which allows stationary Ohmic ELMy H-mode operation in over wide range of elongation, triangularity and density. Divertor detachment experiments suggest the existence of recombination pathways other than three-body or radiative processes.

1. Recent Advances

The TCV (Tokamak à Configuration Variable, R=0.88m, a<0.25m, B_T<1.54T) with a vessel elongation of 3, was designed to be a highly versatile facility destined for the investigation of the effects of plasma shaping on confinement and stability [1]. Following the installation of a flexible ECH heating and current drive system, now totalling 2.8MW of power available to the plasma at the second cyclotron harmonic (82.7GHz), TCV has delivered significant achievements to the fusion community. One of the most important of these is probably the first demonstration of steady-state fully non-inductive ECCD operation for 2s at plasma currents of up to 210 kA [2,3]. These experiments also established the necessity of tailoring the driven current profile by suitably distributing the six available sources over the plasma cross section in order to avoid disruptive MHD instabilities and have provided a first validation of theoretical predictions for ECCD efficiencies in steady-state conditions.

ECCD and ECH also have proven to be powerful tools for current profile modification for the purpose of establishing and controlling improved core confinement (ICC) modes and for improving vertical stability at high elongation. Reversed or weak central shear discharges at moderate elongation (κ~1.7), produced by central counter-current drive (CNTR-ECCD) in combination with off-axis ECH for improving MHD stability, have lead to stable electron confinement enhancements H_{RLW}=3.5 over Rebut-Lallia-Watkins scaling, limited in duration by the length of the ECH pulse. With Ohmic heating alone, the most elongated plasmas can only be vertically stabilized at high plasma current and the highest elongation achieved so far is 2.8 with an edge safety factor q_{95}=2.5. The addition of a moderate level of off-axis ECH power (1MW) has recently allowed the minimum stable plasma current for κ_a=2.4 to be reduced three-fold to 300kA, corresponding to q_{95}=8.2. These experiments open up a wide and promising operational domain for future investigation of improved confinement modes at high elongation.

Investigations of the scaling of sawtooth inversion radii and profile shapes have revealed that these depend solely on the parameter $\langle j \rangle / q_0 j_0$ (defined in section 6) in Ohmic plasmas and both on this parameter and the deposition profile with ECH/ECCD. The results show that, due to the significant effect of the central elongation, current profile width and inversion radii do not become excessive at high elongation. A study of sawtooth behaviour as a function of elongation revealed a marked decrease of sawtooth periods and crash amplitudes for κ_a>2, both with ECH and in purely Ohmic plasmas, attributed to a reduced internal kink stability margin.

The first of three gyrotrons, destined for operation at the third harmonic X-mode (118GHz), has been brought into service for physics investigations of the role of target plasma conditions on wave absorption. These experiments have demonstrated that absorption of X3 power is vastly enhanced when a suprathermal electron population produced by X2-ECCD is present in the plasma. Total absorption (within 10% error bars) was achieved for the 470kW of injected X3 power with as little as 350kW of X2-ECCD for target plasma conditioning, as compared to 25% absorption with the same power of X2-ECH.

Although Ohmic H-modes are easy to obtain in TCV, even with the ion ∇B drift direction away from the X-point, transitions to steady-state ELMy H-modes are only obtained in a narrow region of the operational domain. Remarkably, after such a transition this attractive confinement mode is very resilient to subsequent changes of elongation and density.

Detachment in open divertor geometries and pure deuterium is found to be easier than expected from simulations, suggesting important contributions from recombination pathways other than three-body and radiative processes.

TCV has also been used as a test-bench for the non-linear evolution code DINA [2] with the purpose of validating it for ITER poloidal field coil feedback controller design.

2. Fully Non-Inductive Operation with ECCD

The six ECH launchers in TCV allow independent steering of the heating sources in both the poloidal and toroidal directions; this high flexibility matches that of the TCV control system, permitting the entire vast range of shapes that can be created to be heated in an accurately localized manner. The six sources can be employed to tailor the current profile in a stationary manner, as will be required in a prospective reactor for MHD stabilization and optimization of performance. Crucial to the stationarity requirement is the ECH pulse length capability which substantially exceeds the current redistribution time from Ohmic to non-inductively driven profiles (typically < 0.5 s).

Studies have been carried out over the past year in TCV at increasing power levels to demonstrate stable, steady-state current profile control and to validate ECCD physics. After the first demonstration of fully non-inductive operation in steady state with ECCD in a tokamak was performed in TCV [3], work has progressed to a present record non-inductively driven current of 210 kA [4], shown in Fig. 1. The current is sustained non-inductively for 2 s, while plasma conditions relax over a time scale of less than 0.5 s. The current in the Ohmic transformer primary is kept constant by feedback throughout the ECCD pulse; thus, in the stationary phase during which the currents in all the shaping coils are also constant, no flux supplied to the plasma. The bootstrap current fraction is calculated to be 8% in this discharge. The conventional normalized ECCD efficiency of the discharge in Fig. 1 corresponds to 0.0073 [10^{20}A/W/m^2]. Higher efficiencies, up to 0.016 in the same units, have been obtained by concentrating all sources in the centre, but such discharges become MHD unstable and disrupt.It was experimentally found that at each power level there is a minimum stable driven current profile width, below which such MHD instabilities develop and lead to disruption. As these instabilities are driven by current or pressure gradients, which increase with power for constant profile shape, the deposition width must be increased with increasing power. This results in an effective degradation of the maximum global ECCD efficiency with power. By way of illustration of this effect, Fig. 2 shows the power and current deposition profiles calculated by the linear ray tracing code TORAY [5] (with the Cohen package [6] for current drive estimation) for the case of Fig. 1 and for a case with similar plasma conditions but only three sources (1.35 MW) and a steady-state non-inductive current of 160 kA. Each case corresponds to the narrowest stable deposition profile identified over a series of discharges at each power level.

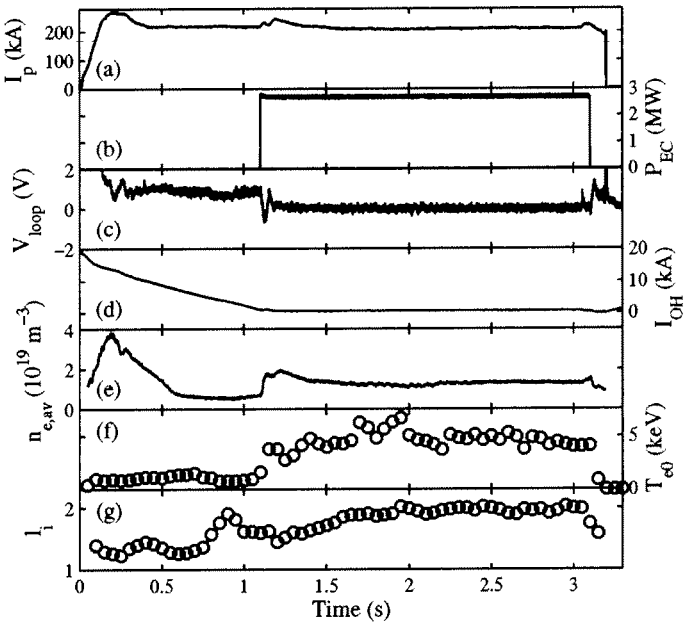

Fig. 1 Steady-state, fully non-inductive 210 kA discharge in a single-null diverted plasma with 2.8 MW of distributed ECCD: time histories of (a) plasma current, (b) EC power, (c) edge loop voltage, (d) current in the Ohmic transformer primary, (e) line-averaged density, (f) peak electron temperature, (g) internal inductance

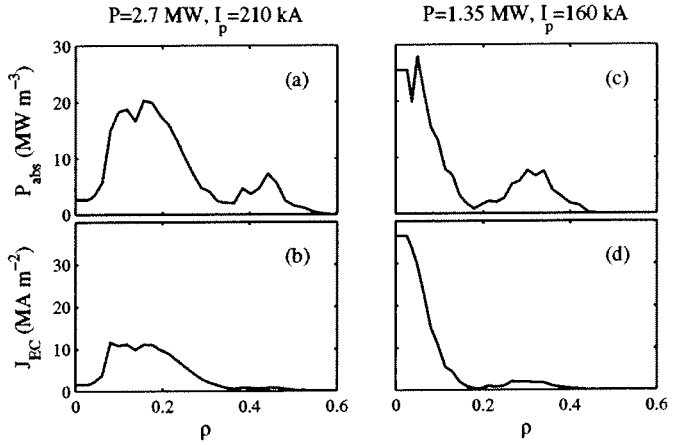

Fig. 2 Flux-surface-averaged (a)-(c) absorbed power and (b)-(d) driven current density as functions of a normalized radial coordinate proportional to the square root of the plasma volume, for two different discharges. All profiles are calculated by TORAY. Line-averaged density $1x10^{19}$ m^{-3} (a-b) and $1.2x10^{19}$ m^{-3} (c-d), central electron temperature 3.1 keV (a-b) and 3.7 keV (c-d).

The fundamental principles of ECCD have been known for twenty years [7] but a thorough experimental validation is still missing. One of the principal aims of the ongoing experiments on TCV is to provide that validation, particularly through measurements of the ECCD efficiency $\eta = I_{EC}/P$. I_{EC} is the driven current and P the EC power, has the theoretical dependence $\eta = T_e \eta_T' / [R n_e (Z_{eff} + 5)]$, where T_e is the electron temperature, R is the major radius, n_e is the density, Z_{eff} is the effective ion charge and η_T' is a function of the trapped particle fraction and of the parallel wave number [7]. The dependence on the trapped particle fraction in particular is predicted to be strong and to result in a rapid reduction of η_T' with increasing minor radius. The average efficiencies measured on TCV in a series of fully non-inductive discharges with varying deposition profile widths have shown up a dependence on the minor radius of the magnitude predicted by theory, giving a clear indication of the existence of trapped particle effects [4]. Furthermore, the absolute value of η_T' agrees with predictions by the linear **TORAY** code to within 30%, over a range of profiles resulting in a variation in η_T' of a factor of 3.5. Nonlinear effects thus do not appear to be significant in the present conditions.

3. Quasi-Stationary Improved Core Confinement by Shear Optimization

An Improved Core Confinement (ICC) regime has been obtained by current profile tailoring with ECH and ECCD in quasi-steady state conditions [9]. The intense central counter current drive (CNTR-ECCD) produced in the ICC regime and related equilibrium modelling suggest the presence of a strong reverse shear profile in the plasma core. In most tokamak experiments reversed shear profiles are obtained only transiently by heating during the ramp-up phase of the plasma current. Taking advantage of the very localized power deposition, which is typical of ECH, and making use of the flexibility of the beam launching system on TCV, an optimized current density profile could be established and maintained for the duration of the heating pulse, corresponding to 200 energy confinement times and several current redistribution times. For this purpose a combination of 4-5 X2 heating beams was used to deliver a total power in the range 1.8-2.3 MW to the plasma. The optimized scenario begins with off-axis heating just outside the q=1 surface using two or three X2 beams followed 300 ms later by central power deposition with a strong counter current drive (CNTR-ECCD) component using two beams. The discharge evolution is shown in Fig. 3 for two examples with central CNTR-ECCD and for central ECH. Typical plasma parameters were $\delta_{95} \approx 0.2$, $\kappa_{95} \approx 1.6$, $q_{95} \approx 6$, $I_p \approx 200$kA and $\langle n_e \rangle \approx 1.5 \times 10^{19} m^{-3}$. Central CNTR-ECCD leads to significantly higher peak electron temperatures (8-12 keV) than central ECH (~4keV) and better global plasma performance. The delay between the beginning of the off-axis ECH and the on-axis CNTR-ECCD, which is of the order of the current redistribution time, is necessary to establish a suitably broad and MHD stable target current profile for the central CNTR-ECCD pulse. If the delay is reduced to zero, or if the off-axis ECH is altogether omitted [9], high temperatures (~10keV) can also be obtained, although these discharges are often violently sawtoothing and disruptive.

The achieved electron energy confinement times exceed the one predicted by the Rebut-Lallia-Watkins (RLW) scaling law by a factor of 3.5, as seen in Fig. 3b. Unlike discharges with central CNTR-ECCD only, these ICC plasmas are MHD quiescent, like #18639 in Fig. 3 and #18518 in Fig. 4, or else only exhibit benign levels of sawtooth activity, like #18635 in Fig. 3, with crash amplitudes of ~3keV and periods of ~20ms, which far exceed the global energy confinement time of ~5ms. In the absence of direct measurements of the current density profile, the evolution of the q-profile and its relation to the reduction in transport coefficients is inferred from time dependent simulations [11] using the PRETOR code [12] and the RLW local transport model. The RLW transport parameters depend strongly on the magnitude of the

magnetic shear, but are assumed not to depend on its sign. An example is presented in Fig. 4a, with simulated temperature profiles for the Ohmic, off-axis ECH and high performance ICC phases, together with the experimental data from Thomson scattering, showing good agreement. Within the framework of the local RLW heat diffusivity model, used in these calculations, the negative shear zone near the center is essential for the confinement enhancement [11]. The corresponding q-profiles in Fig. 4b show reversed shear during the central counter ECCD phase. The central CNTR-ECCD current is calculated to be 125kA. The range of plausible q-profiles has been computed by PRETOR used as a fixed-boundary equilibrium solver (without transport model) constrained by the experimental density and temperature profiles, the effective ion charge, the edge loop voltage, and reflects the high sensitivity of the calculation to the location of the CNTR-ECCD source taken from TORAY calculations. This sensitivity to the ECCD source location has motivated an experimental scan of the position of the CNTR-ECCD component which has shown that an outward displacement of only 10% of the minor radius caused a 40% reduction in the central plasma temperature, which is also borne out by the PRETOR simulations [13].

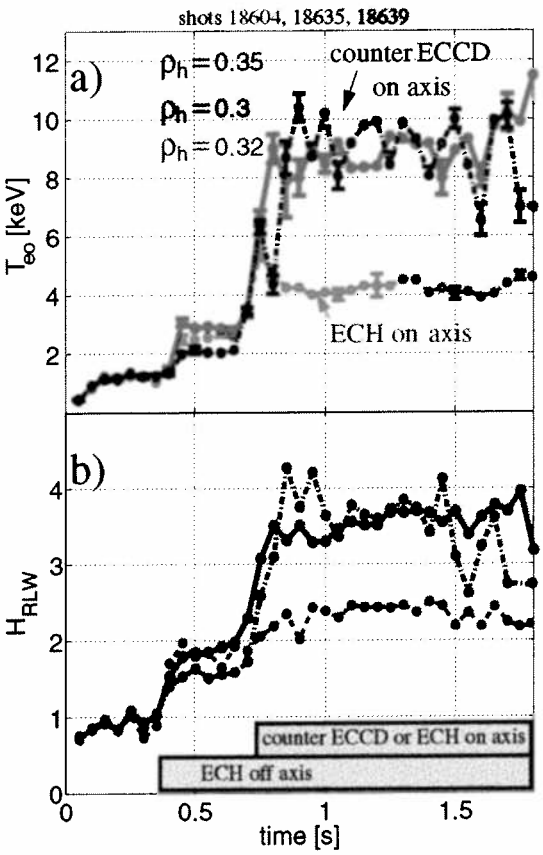

Fig. 3 a) Evolution of central electron temperature from Thomson scattering and b) enhancement factor over RLW energy confinement time for different ECH/CNTR-ECCD scenarios combining off-axis ECH (0.9MW) at different locations ρ_h with delayed central ECH or CNTR-ECCD. green: with 0.9MW central ECH blue and red: with 0.9 MW central CNTR-ECCD

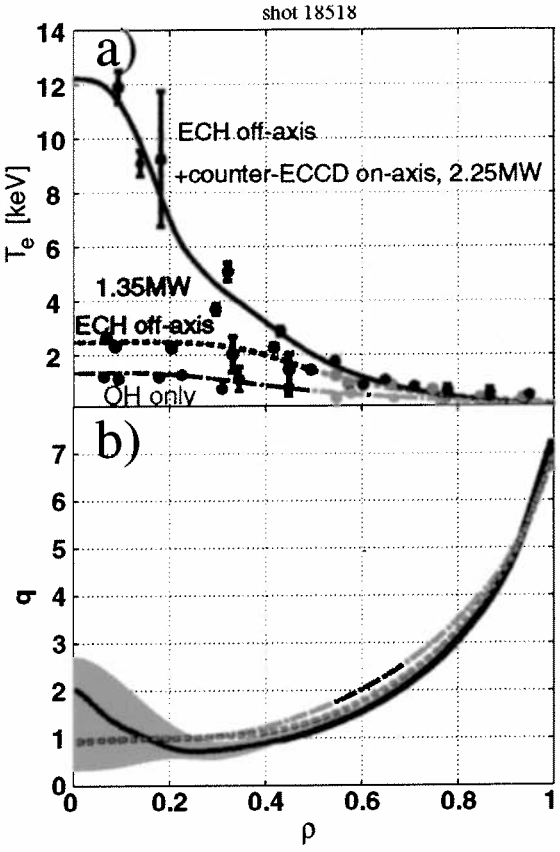

Fig. 4 a) Electron temperature profiles as simulated using RLW transport model for 3 phases of an ICC shot, together with measurements.
Fig. 5 green: OH phase, red: 1.35 MW off-axis ECH, blue: combination off-axis ECH and 0.9MW central CNTR-ECCD.
b) Corresponding calculated safety factor profiles with uncertainties (shaded) related to location of central CNTR-ECCD sources.

4. Full Absorption of ECH Power at the Third EC Harmonic in X-Mode

Plasmas in the TCV Tokamak have, for the first time, been heated using the first of three 0.5MW gyrotrons to be deployed at a frequency of 118 GHz [14], corresponding to the third EC harmonic. One of the motivations for X3 ECH in TCV is the possibility of heating at densities which are inaccessible with the X2 ECH system. The experiments reported here were aimed at establishing the importance of the plasma conditions, mainly electron temperature and suprathermal tail electron distributions, for the absorption of X3 ECH power [15]. For this purpose the plasmas were preheated with different power levels of X2 ECH and ECCD. The X3 wave was launched from the low field side via one of the upper lateral launching mirrors normally used for X2 heating [16].

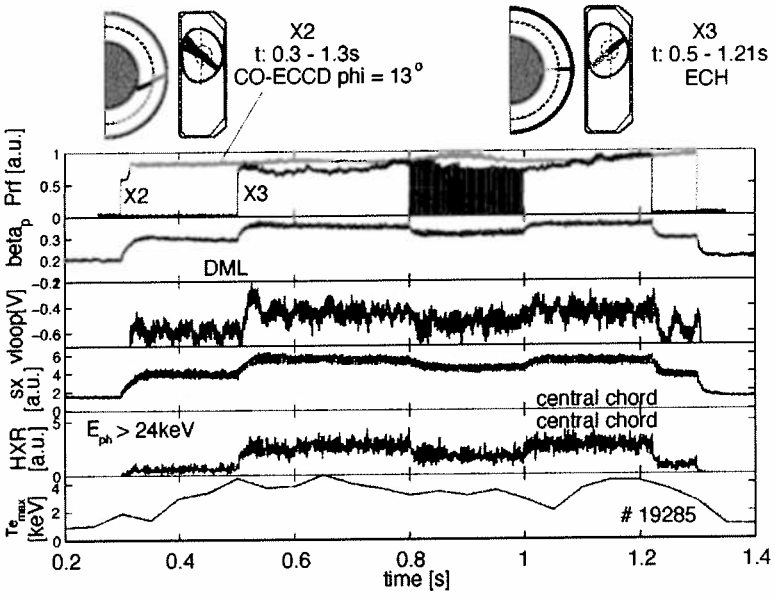

The target plasmas used in these experiments have the parameters R=0.88m, a=0.25m, κ=1.31, B_0 = 1.42T, $n_e(0)= 2.5\times10^{19}m^{-3}$. The launching geometry and time traces of relevant parameters are shown in Fig. 6 for a typical discharge. The top trace shows the timing X2 ECCD and X3 ECH. In all experiments the X2 power was kept constant from 0.3s to 1.3s whereas the X3 power was applied from 0.5s to 1.2s and included a phase with 100% modulation at 237Hz (0.8s to 1s).

Fig. 6 Launching geometry and typical time traces for the X2 and X3 ECH. Top to bottom: RF power, poloidal beta, loop voltage, soft X-ray signal, hard X-ray signal, peak electron temperature. $P_{X2}=P_{X3}=0.47M$, $I_p=200kA$.

The total stored energy variation was measured during the modulated part of the X3 RF pulse using a diamagnetic loop. The modulation frequency of f_m=237Hz was chosen such that $1/2\pi f<\tau_e\sim5$ms, where τ_e is the electron energy confinement time. While the X3 power (0.47MW) and launching geometry, aimed at the plasma centre, were kept constant, different X2 conditions were investigated, including variations of the toroidal launch angle ϕ, the power deposition radius, the total X2 power and the plasma current. A toroidal injection angle scan of the X2 launch, with $P_{X2}\approx P_{X3}$=0.47MW, has revealed a clear asymmetry. X3 absorption is highest on target plasmas with X2 injected with $\phi=+13^0$, corresponding to CO-ECCD. Fig. 7 shows the X3 absorbed power fraction, versus X2 preheat power for three X2 launching angles corresponding to CO-ECCD ($\phi=13^0$), ECH ($\phi=0^0$) and CNTR-ECCD ($\phi=-13^0$). For CO-ECCD target plasmas, nearly 100% absorption is obtained.

Calculations of the theoretical absorption with the TORAY ray tracing code [5], which makes the assumption of an isotropic, Maxwellian velocity distribution, are in fair agreement with the experimental results corresponding to ECH preheating. This observation is also in agreement with X3 absorption measurements by Pachtman et al. [17]. However, the measured X3 absorption exceeds that predicted by TORAY by a factor of up to 3 for the CNTR- and CO-ECCD cases. The only explanation of the discrepancy is that a large fraction of the X3 power is

absorbed by energetic tail electrons created by X2 ECCD. The presence of these is confirmed by the measurement of photon spectra using an energy resolving hard X-ray camera and a high field side ECE radiometer. The ECE radiometer detects suprathermal radiation levels exceeding the thermal level by an order of magnitude, while effective X-ray photon temperatures of tens of keV are measured in the presence of ECCD and X3 ECH. The insert in Fig. 7 shows that hard X-ray (>10keV) emission is highest with X2 CO-ECCD and lowest with X2 ECH in all phases of the experiment.

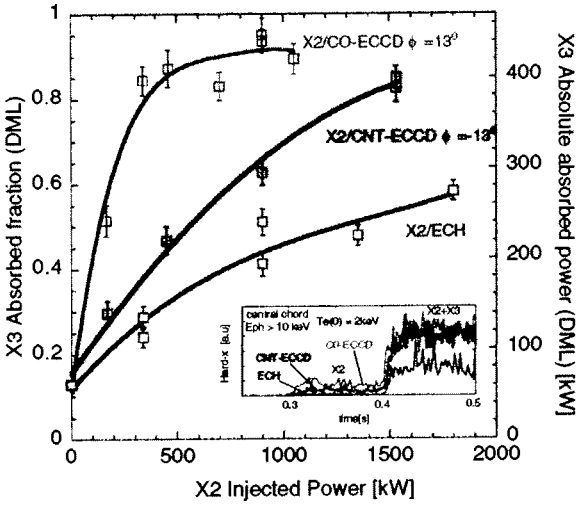

Fig. 7 Measured X3 absorption using the DML versus X2 preheat power for three different X2 launching configurations:
- CO-ECCD (green, $\phi=13^o$),
- CNTR-ECCD (red, $\phi=-13^o$),
- and ECH (blue, $\phi=0^o$).
3^{rd} harmonic ECH ($\phi=0^0$) is kept constant at 0.47MW with central deposition.
Insert shows hard X-ray (>10keV) signals for X2 Co- (green) and CNTR-ECCD (red) as well as X2 ECH (blue) cases. X3 ECH is applied from 0.4 s when the large rise in hard X-ray emission is observed.

The toroidal angle asymmetry suggests that the Ohmic electric field may also play an important role in shaping the energetic tail electron velocity distribution. This hypothesis is confirmed by ECE, hard X-ray and absorption measurements in a loop voltage scan in the range 0.23-0.55V, obtained by varying the plasma current from 130-230 kA, with $\phi=13^0$. Absorption decreases significantly as the loop voltage is reduced.

5. Particle Transport with High Power ECH and ECCD

A coupled heat and particle transport phenomenon, leading to particle depletion from the plasma core is observed in a variety of plasma conditions with centrally deposited ECH and ECCD in TCV. This phenomenon, known as "density pumpout" causes inverted density sawteeth in the core of sawtoothing discharges and leads to stationary hollow profiles in the absence of sawteeth. The density pumpout has been linked to the presence of (n,m)=(1,1) MHD modes and can be suppressed by stabilizing the mode by means of operation at high triangularity. The correlation of pumpout with loss of axisymmetry suggests that neoclassical transport processes involving locally trapped particles other than those arising from the toroidal field ripple and analogous to those in heliacs, may account for the phenomenon in tokamaks as well.

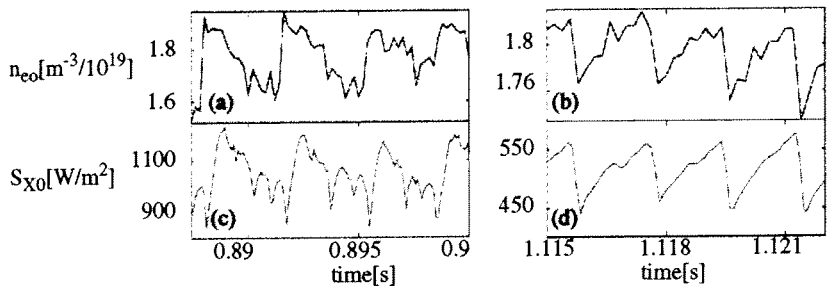

Fig. 8 Sawteeth on central Abel-inverted density (top) and raw X-ray signal (bottom) for Ohmic *heating (left) and* ECH *(right) with $\delta_a=0.22$ and $P_{ECH}=1.45MW$.*

Fig. 8 shows the difference in sawtooth behaviour at low and high heating power at low triangularity. For $P_{ECH}>0.5$ MW density sawteeth are inverted. The situation is different at high triangularity ($\delta_a>0.3$) when both X-ray traces and central densities have "normal", triangular sawteeth. The essential difference appears to be that at low triangularity a (1,1) magnetic island

is present during the sawtooth ramp phase, whereas the plasma is MHD-quiescent during the ramp phase at high triangularity.

The convective heat flux associated with the "pumped-out" particles is a small fraction, estimated to be less than 10%, of the loss power from the core. In sawtoothing plasmas strongly hollow density profiles cannot develop because the sawtooth crashes regularly flatten density and temperature profiles. However with ECCD many situations arise when sawteeth are stabilized for long enough (typically 10 ms or more) for the hollowness to become significant enough for the Thomson scattering system, as shown in Fig. 9.

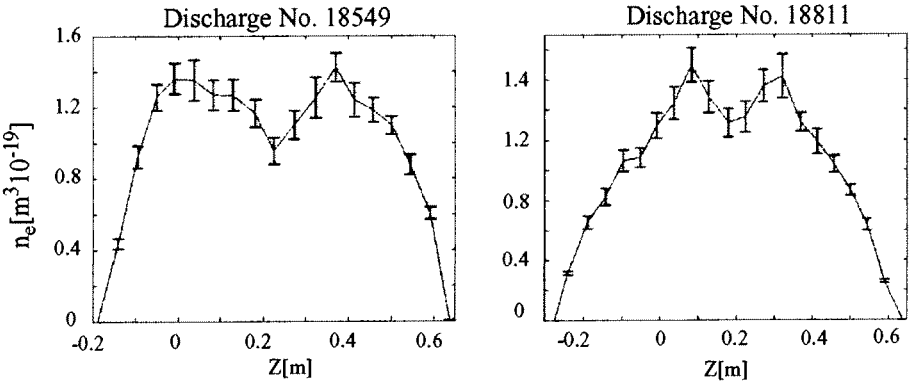

Fig. 9 Examples of electron density profiles in full CO-ECCD (left) and Counter-ECCD discharges (right).

One of the first explanations for "pumpout" in tokamaks by Hsu et al [18], based on the production of an excess of banana electrons and a poloidal charge asymmetry, is not consistent with our observations [19]. We propose that a loss of axisymmetry provides the crucial physics for this phenomenon by allowing the existence locally trapped particles, which are not confined in the core region. The presence of an (n,m)=(1,1) island causes the core to be helically displaced. The vicinity of the displaced core acquires stellarator-like features. As a result trapped particle orbits exist even at the magnetic axis, just as in a heliac configuration. This region may act as a sink from where locally trapped particles are lost to beyond the non-axisymmetrical region (typically outside q=1). The coexistence of locally and toroidally trapped particles within the q=1 surface can also be expected to give rise to competing transport phenomena, including pumpout, since the neoclassical off-diagonal terms associated with these two classes of particles have opposite signs. Near the displaced axis the effect of locally trapped particles dominates, giving rise to an outward flux (d_{12}~*1* in the long mean-free path regime), while further away toroidally trapped particles (d_{12}=-*1/2*), or an anomalous mechanism, are most important, giving rise to an inward pinch [20].

6. Dependence of Inversion Radii and Peaking Factors on Plasma Shape

When considering highly elongated tokamak designs, a frequently expressed concern is that as a result of the high current carrying capacity of elongated plasmas, sawtooth in inversion radii and consequently crash amplitudes may become excessive. In Ohmic plasmas we observe that the normalised sawtooth inversion radius ρ_{inv} and the profile inverse peaking factors (normalised widths) $\langle p_e \rangle / p_{e0}$, $\langle T_e \rangle / T_{e0}$ and $\langle n_e \rangle / n_{e0}$ for electron pressure, temperature and density, depend on the current profile peaking via the parameter $\langle j \rangle / (q_0 j_0)$, where $\langle j \rangle$ is the cross-sectionally averaged current density, irrespective of plasma shape and electron density [22]. This parameter can be evaluated without knowledge of the still somewhat controversial value of the axial safety factor since $q_0 j_0 = B_0 (\kappa_0 + 1/\kappa_0) / (\mu_0 R_0)$, where κ_0 is the axial elongation. The core elongation is generally in good agreement with the elongation of emissivity contours from X-ray tomography. In order to reduce the large scatter of the Thomson scattering measurements at random times in the sawtooth cycle we define "clipped" profile widths as

$<\bar{T}_e>/T_{e1}$ where T_{e1} is the electron temperature at the sawtooth inversion radius and $\bar{T}_e=T_{e1}$ for $\rho<\rho_{inv}$ and $\bar{T}_e=T_e$ for $\rho\geq\rho_{inv}$. These widths are sensitive to the profile in the confinement zone ($q>1$) and are shown in Fig. 10 for a wide variety of Ohmic and ECH L-mode plasmas [23]. The Ohmic data show a remarkably narrow distribution as a function of $<j>/(q_0 j_0)$ and are in good agreement with an Ohmic relaxation model based on the assumption that the magnetic entropy is stationary in time [24]. The parameter $<j>/(q_0 j_0)$ performs better than safety factor based scalings such as $1/q_{95}$, for which the dispersion is larger, and is related to the popular database variables q_{95}, κ_{95} and δ_{95} [23]. With ECH heating $<j>/(q_0 j_0)$ remains the primary scaling parameter, but now the profiles are modified by the ECH heat deposition profiles, the widths of which are not matched in the experiments to $<j>/(q_0 j_0)$.

TCV results show that frequently expressed fears of excessively large inversion radii and sawtooth amplitudes at high plasma elongation, susceptible to trigger NTM's, are ill founded. In TCV sawtooth amplitudes decrease with elongation both in Ohmic and in ECH heated discharges [21]. The normalized sawtooth inversion radius can be kept fixed while scaling up the plasma elongation κ_{95}, albeit at a modest penalty in plasma current (typically 10% for $\kappa_a=2$), as compared to scaling at fixed q_{95} [23].

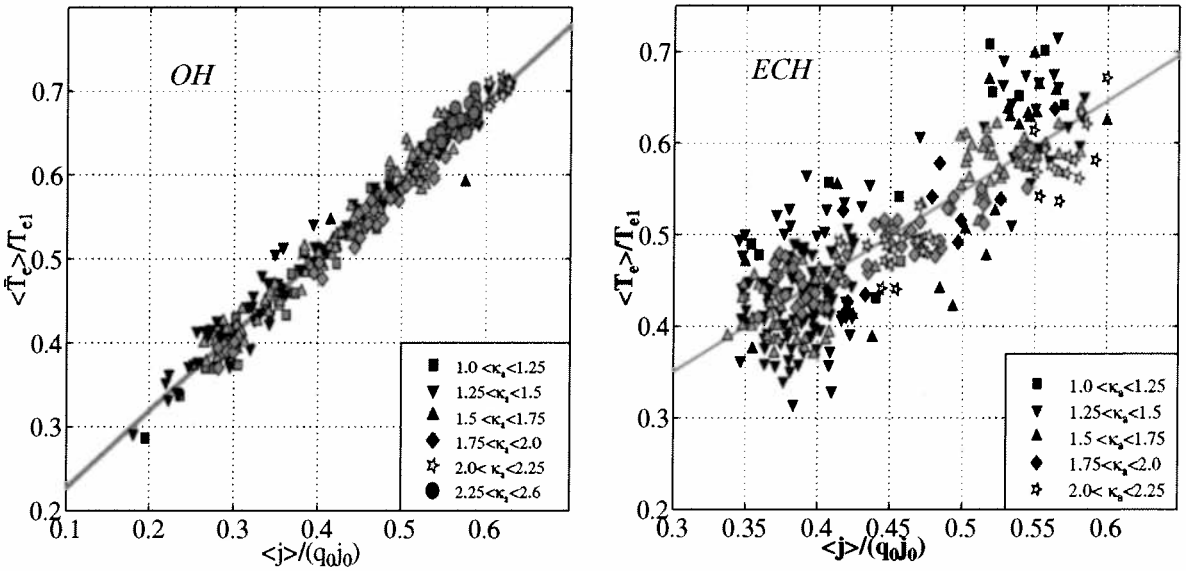

Fig. 10 Electron temperature inverse peaking factors in Ohmic (left) and ECH (right) plasmas.

7. Development of Highly Elongated Discharges

One of the main aims of the TCV tokamak is the creation and study of highly elongated plasmas. Part of the motivation for this comes from the fact that the maximum plasma current increases with elongation and according to Troyon scaling [25], the beta limit is proportional to the normalized current, $I_N=I/(aB_T)$. This favorable trend has been verified experimentally up to elongations of $\kappa=2.3$ [26], but it is not known whether it continues to be valid at higher elongation. The creation of elongated plasmas with $\kappa>2.5$ in a tokamak with conventional aspect ratio is an extremely difficult task [27]. In Ohmic plasmas, axisymmetrical stability imposes a lower limit to the normalized plasma current, which is necessary to produce a sufficiently broad current profile, and simultaneously, the non-axisymmetrical modes impose an upper limit to the current. The stable operating window between these two limits decreases as the elongation increases.

Axisymmetrical stability can be improved in several different ways. First, the passive stability can be improved by adapting the plasma shape as closely as possible to the shape of the vac-

uum vessel. Second, the vertical position control system can be optimized such that operation at very low stability margins becomes possible. Third, the current profile can be widened either by operating at the maximum possible plasma current, by using a fast ramp-up scenario or by applying off-axis ECH/ECCD. Non-axisymmetrical stability, on the other hand, can be improved by operating at low beta or at low current, since at high elongation, the current limit increases as beta decreases [28]. Clearly, the requirements for axisymmetrical and non-axisymmetrical stability are partially contradictory. As a result, beyond a certain elongation, the stable operating window shrinks to zero. Using the above methods in Ohmic plasmas, a maximum elongation κ=2.8 with I_p/aB_T=3.6MAm^{-1}T^{-1} has been achieved in TCV (Fig. 11).

With Ohmic heating alone such extreme elongations have only been obtained at high values of normalized average current density, $\langle j\rangle^*=\mu_0 R_0\langle j\rangle/B_T$ ~1.7. With 1-2MW of ECH power deposited near or outside mid-radius, it is possible to create highly elongated plasmas with much lower values of $\langle j\rangle^*$[29]. In the example of Fig. 12 plasma elongation was raised from $\kappa_a\approx$1.75 to κ_a=2.4 corresponding to $\langle j\rangle^*$=0.46 and $\langle j\rangle/q_0 j_0$=0.2, just by applying the ECH power at fixed quadrupole field. The resulting broadening of the current profile leads to vastly improved vertical stability. The example presented has a temperature profile width $\langle T_e\rangle/T_{e0}\approx$0.4, which is a factor ~1.5 times broader than obtained in Ohmic plasmas at the same value of $\langle j\rangle/q_0 j_0$. These experiments open up a wide operational domain for the investigation of confinement at high elongation.

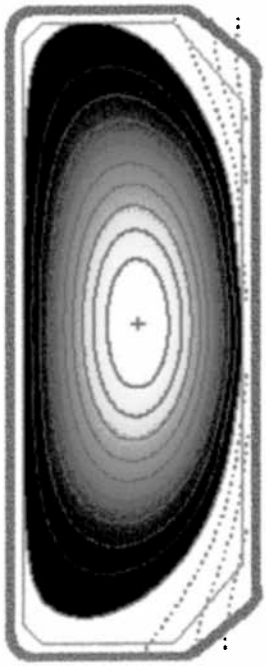

Fig. 11 (left)
Record elongation in TCV (#19373). I_p=755kA, B_T=0.8T, κ_a=2.8, k_0=2.15, δ_a=0.4, q_{95}=2.5, $\langle j\rangle^*$=1.74

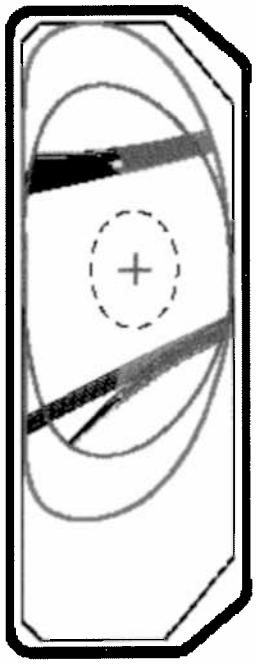

Fig. 12 (right)
ECH-assisted, highly elongated plasma (#19533).
Magenta: LCFS of initial configuration.
Red: LCFS of final elongated plasma with I_p=300kA, B_T=1.43T, κ_a=2.4, q_{95}=8.3, $\langle j\rangle^*$=0.46. ECH ray trajectories from TORAY are also shown, parts beyond X2 resonance are in black.

8. Ohmic ELMy H-mode accessibility

Ohmic H-modes are easily obtained in TCV, even with ∇B away from the X-point. In most conditions these are ELM-free and terminate in a high density disruption. Transitions from L-mode to stationary ELMY H-modes for SN configurations with reversed ion ∇B are only observed (at the nominal field B_T=1.43T) in a narrow range of discharge parameters: 0.35MA$\le I_p\le$0.43MA, 4.5×10^{19}m$^{-3}\le\langle n_e\rangle\le$6×10^{19}m^{-3}, 1.6$\le\kappa_a\le$1.7, 0.5$\le\delta_a\le$0.6. Moreover the gap width between the inner wall and the plasma last closed flux surface must be between 1 and 3 cm. Outside this domain either L-modes or ELM-free H-modes are obtained. This would be very restrictive, were it not for the high robustness of the ELMy H-mode, once it is established. After the transition both the plasma elongation (together with the plasma current)

and the plasma density can be varied over a wide range as shown in Fig. 13 [30]. An ELM-insensitive magnetic position observer has been developed, which prevents an undesirable vertical controller response during the ELM events [31].

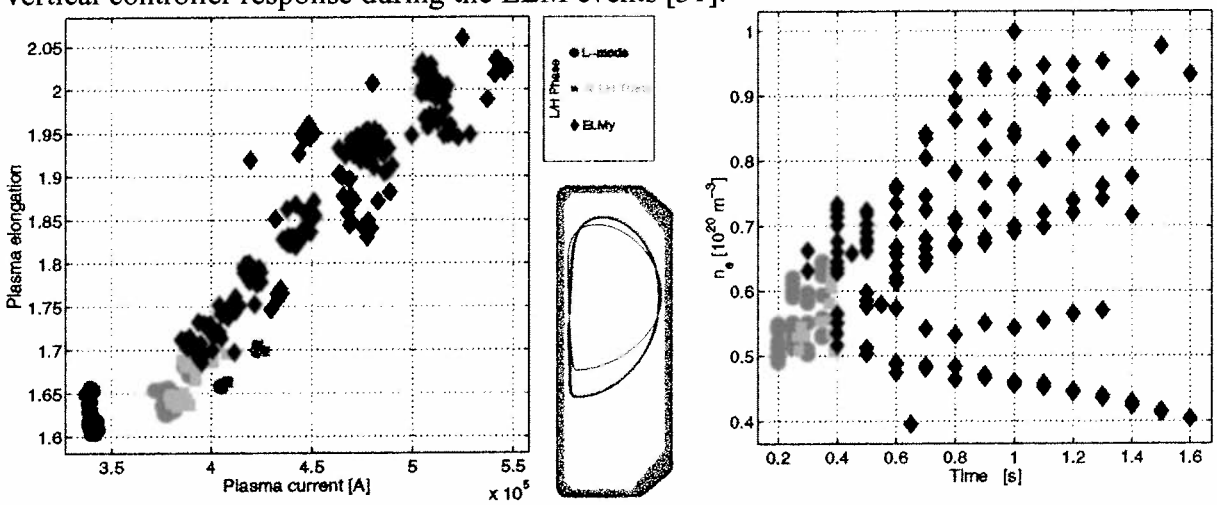

Fig. 13 Operational domain for ELMy SN H-modes. a) Accessible elongations and currents b) Accessible density (time evolutions). All discharges transited through a "gate" in the operational domain indicated by the green symbols. Central insert: LCFS at transition and at highest elongation.

9. Detachment in Variable Divertor Geometry

Although the requirement of shape flexibility precludes the use of fixed baffle or optimized divertor target structures, it does allow for the investigation of diverted equilibria not achievable in more conventional tokamaks. One such configuration, shown in Fig. 14, has been extensively used for studies of divertor detachment in Ohmic conditions and unfavorable ∇B drift direction with deuterium fueling only [32]. The equilibrium is simultaneously characterized by a very short inboard poloidal depth from X-point to strike point on a vertical target and an extremely long poloidal depth to a horizontal target on the outboard side. Density ramp discharges, invariably terminated by an X-point MARFE, leave the inboard target plasma attached even at the highest densities, whilst clear partial detachment is observed at the outboard target. Extensive modelling of this configuration using the B2-EIRENE coupled package shows in fact that the outboard divertor achieves high recycling at very low densities, with the rollover to detachment occurring near the outer strike point very soon after the density ramp begins. The differences in detachment threshold at the two targets can be ascribed to a large extent to divertor magnetic geometry.

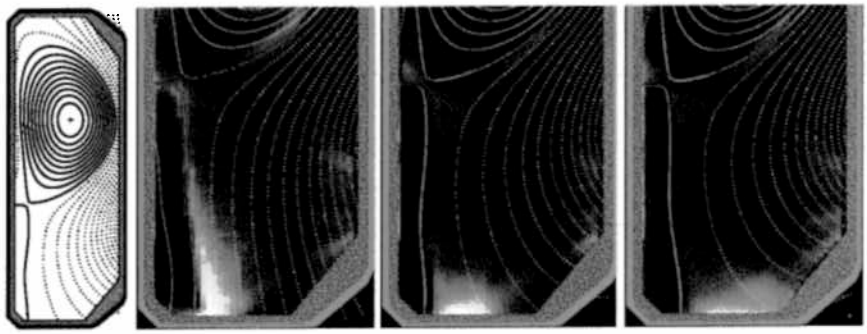

a) #17823 b) #17824, f_e = 2.8 c) #17823, f_e = 6.4 d) #17822, f_e = 9.3

Fig. 14 Distributions of D_α emissivity for varying outer target flux expansion at the same degree of detachment.

Whilst there is little latitude for changing the inboard geometry, a series of experiments has recently concentrated on studying the effect of outer target flux expansion, f_e, on the detachment behaviour. Fig. 14 (b,c,d) show inverted tangential CCD camera images of D_α emissivity from the divertor volume for the same absolute degree of detachment [33] as f_e

increases. The distributions clearly show the effect of plasma plugging by the expanded flux surfaces and can be qualitatively reproduced by code simulations. Interestingly, however, the latter find the maximum in the emissivity to be located at the strike point, in evident disagreement with experimental observation [34]. Moreover, the code cannot quantitatively reproduce the absolute level of detachment without artificially increasing fivefold the charged particle sink due to three-body and radiative recombination. This is a strong indication that other processes, perhaps involving molecularly assisted recombination pathways, dominate in the relatively low density plasma characterizing the TCV outer divertor. Such pathways are currently under further study.

Acknowledgement: This work was partly supported by the Swiss National Science Foundation.

References:

[1] Hofmann F. et al., Plasma Phys. Control. Fusion **36** (1994) B277
[2] Karyutdinov R.R and Lukash V.E., J. Comp. Physics **109** (1993) 193
[3] Sauter O. et al, Phys. Rev. Letters **84** (2000) 3322
[4] Coda S. et al, to be published in Plasma Phys. Control. Fusion (2000)
[5] Kritz A.H. et al, Proc. 3rd Varenna-Grenoble Int. Symposium on Heating in Toroidal Plasmas, Grenoble, 1982 (CEC, Brussels), vol. II, p. 707
[6] Cohen R. H., Phys. Fluids **30** (1987) 2442
[7] Fisch N.J. and Boozer A.H., Phys. Rev. Letters **45** (1980) 720
[8] Alikaev V.V. and Parail V.V., Plasma Phys. Control. Fusion **33** (1991) 1639
[9] Pietrzyk Z.A. et al., 27th EPS Conf. Contr. Fusion and Plasma Phys., Budapest, 2000, P4.099
[10] Pietrzyk Z.A. et al., *Phys. Plasmas* **7** (2000) 2909
[11] Angioni C. et al., to be publ. in *Theory of Fusion Plasmas,* Ed. Compositori, Bologna 2001
[12] Boucher D. and Rebut P.H., in *Proc. IAEA Tech. Conf. on Advances in Simulation and Modelling in Thermonuclear Plasmas*, Montréal, 1992
[13] Goodmann T.P. et al., this conference, paper EXP4/09
[14] Alberti S. et al, to be published in Fusion Engineering Design
[15] Alberti S. et al, this conference, PD/2
[16] Goodmann T.P. et al., In *Proc. 19th Symp. Fusion Technology* (Lisbon, 1996) Vol 1, Ed. C. Varandas and F. Serra (Amsterdam: Elesevier), p 565.
[17] Pachtman A., Wolfe S.M., Hutchinson I.H., *Nuclear Fusion*, Vol.27, No.8, (1987)
[18] Hsu J.Y. at al., *Phys. Rev. Lett.* **53** (1984) 564
[19] Weisen H., Furno I., Goodman T. and TCV Team, this conference, PDP/6
[20] Kovrizhnykh L.M., *Nucl. Fusion* **24** (1984) 851
[21] Reimerdes H. et al, *Plasma Phys. Contr. Fusion* **42** (2000) 629
[22] Weisen H. et al, *Plasma Phys. Contr. Fusion* **40** (1998) 1803
[23] Weisen H., Furno I. and TCV Team, submitted to *Nucl. Fusion,* CRPP report LRP 685/00
[24] Minardi E. and Weisen H., accepted for *Nuclear Fusion*, CRPP report LRP 669/00
[25] Troyon F. et al., Plasma Phys. Controlled Fusion **26**, 209 (1984)
[26] Lazarus E.A. et al., Phys. Fluids **B4**, 3644 (1992)
[27] Hofmann F. et al., Nucl. Fusion **28**, 399 (1998)
[28] Hofmann F. et al., Phys. Rev. Lett. **81**, 2918 (1998)
[29] Pochelon A. et al., this conference, paper EXP3/10
[30] Martin Y. et al, this conference, EXP5/30
[31] Hofmann F. et al, 27th EPS Conf. Contr. Fusion and Plasma Phys., Budapest, 2000, P1.029
[32] Pitts R.A. et al., to be published in Journ. of Nucl. Mater. (2000)
[33] Loarte A. et al., Nucl. Fusion **38** (1998) 331
[34] Pitts R.A. et al., this conference, paper EXP4/23

Full Absorption of 3rd Harmonic ECH in TCV Target Plasmas produced by 2nd Harmonic ECH and ECCD

S. Alberti, T.P. Goodmann, M.A. Henderson, A. Manini, J.-M. Moret, P. Gomez, P. Blanchard, S. Coda, O. Sauter, C. Angioni, K. Appert, R. Behn, P. Bosshard, R. Chavan, I. Condrea, A. Degeling, B.P. Duval, D. Fasel, J.-Y. Favez, I. Furno, F. Hofmann, P. Lavanchy, J. B. Lister, X. Llobet, Z. A. Pietrzyk, A. Gorgerat, P. Gorgerat, J.-P. Hogge, P.-F. Isoz, B. Joye, J.-C. Magnin, B. Marletaz, P. Marmillod, Y. Martin, A. Martynov, J.-M. Mayor, J. Mlynar, P. Nikkola, P.J. Paris, A. Perez, Y. Peysson[1], R.A. Pitts, A. Pochelon, H. Reimerdes, J. H. Rommers, E. Scavino, G. Tonetti, M. Q. Tran and H. Weisen

Centre de Recherches en Physique des Plasmas
Association EURATOM-Confédération Suisse
Ecole Polytechnique Fédérale de Lausanne
CH-1015 Lausanne, Switzerland

[1]Association Euratom-CEA sur la fusion, DRFC, CEA-Cadarache, France

email address of main author: Stefano.Alberti@epfl.ch

Abstract. An experimental study of the extraordinary mode (X-mode) absorption at the third cyclotron harmonic frequency (118GHz) has been performed on the TCV Tokamak in plasmas preheated by X-mode at the second harmonic (82.7GHz). Various preheating configurations have been experimentally investigated, ranging from counter-ECCD, ECH to CO-ECCD at various power levels. Full absorption of the 470kW of injected X3 power was measured with as little as 350kW of X2-CO-ECCD preheating. The measured absorption exceeds that predicted by the linear ray tracing code TORAY by more than a factor of 2 for the CO-ECCD case. Experimental evidence indicates that a large fraction of the X3 power is absorbed by electrons in an energetic tail created by the X2-ECCD preheating.

1. Introduction

For the first time in the TCV Tokamak, plasmas have been heated using the first of three 0.5MW gyrotrons to be deployed at a frequency of 118 GHz [1], corresponding to the third harmonic EC X-mode (X3). One of the motivations for X3 ECH in TCV is the possibility of heating at densities which are inaccessible with the existing X2 ECH system, which operates at 82.7 GHz with a total power of 3MW. In the final configuration with 1.5MW of X3 heating, the launching geometry will be vertical (top launch) such that the RF beam **k** vector will have a very shallow incidence angle on the 3rd harmonic resonant layer. Low power transmission measurements in this launching configuration have been performed by Segui et al. [2] on a target plasma with ohmic heating only. Comparison with linear ray tracing/absorption calculations, assuming a Maxwellian distribution function, have been shown to be consistent with the measurements.

In the experiment reported here, the X3 wave was launched from the low field side via one of the upper lateral launching antenna normally used for X2 heating [3]. In this launching scheme the RF beam **k** vector has a large incidence angle on the resonance layer and therefore is favourable for interaction with a wide electron energy spectrum. These experiments were aimed at establishing the importance of plasma conditions on the absorption of X3 ECH power. For this purpose the plasmas were preheated with different power levels of X2 ECH and ECCD.

2. Experimental configuration

The target plasmas used in these experiments have the parameters R=0.88m, a=0.25m, elongation κ=1.31, B_T = 1.42T, $n_e(0)$= $2.5 \times 10^{19} m^{-3}$. The cold resonances corresponding to the X2 and X3 frequencies are spatially separated by approximately 50mm, and, in the target plasma studied here, they are symmetric with respect to the plasma center; the X3 cold resonance being on the low field side.

The launching geometry, as well as a time trace of the relevant plasma parameters, are shown in Fig. 1. The top trace shows the time sequences for the 2nd and 3rd harmonic heating. For all launching configurations the X2 was kept at constant power from 0.3s to 1.3s whereas the X3 power was applied from 0.5s to 1.2s and included a phase with 100% modulation at 237Hz between 0.8s and 1s.

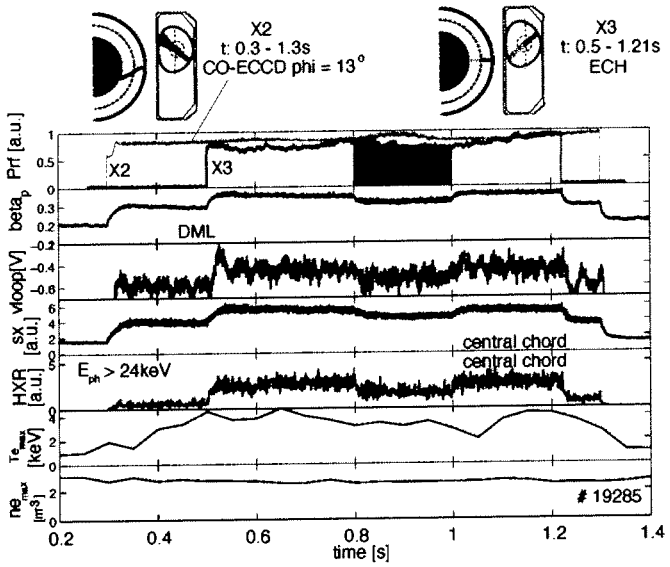

Fig. 1 Launching geometry and typical time traces for the X2 and X3 ECH. For X2, the toroidal injection angle is ϕ=13° (CO-ECCD). From top to bottom: RF power for X2 and X3, beta poloidal measured with DML, loop voltage, soft x-ray signal (central chord), hard x-ray signal (central chord), Thomson scattering peak electron temperature and density (every 50ms).
$P_{X2} \approx P_{X3}$=0.47MW, Ip=200kA.

The large fluctuations on the central electron temperature measured by Thomson scattering are related to the sawtoothing character of the plasma and the 50ms interval between Thomson measurements, the low temperature values being correlated with sawtooth crashes.

The total stored energy variation was measured during the modulated portion of the X3 RF pulse using a diamagnetic loop (DML). The modulation frequency f_m=237Hz was chosen such that $1/2\pi f_m < \tau_e$ ~5ms, where τ_e is the electron energy confinement time.

While the X3 power (0.47MW) and launching geometry, aimed at the plasma centre, were kept constant in this series of experiments, different X2 conditions were investigated including variations of the toroidal launch angle ϕ, the power deposition radius, the total X2 power and the plasma loop voltage by varying the plasma current.

3. X3 absorption measurements

All absorption measurements have been performed with the DML diagnostic in the modulated phase of the X3 power injection which provides an absolute measurement of the absorbed rf power.

Figure 2 shows the X3 absorbed power fraction, versus X2 preheat power for three X2 launching angles corresponding to central CO-ECCD (ϕ=13°), ECH (ϕ=0°) and CNT-ECCD (ϕ=-13°). For CO-ECCD target plasmas, within the experimental error bars, 100% absorption is obtained. A polarization scan of the X3 rf-beam as well as a poloidal scan of the launching

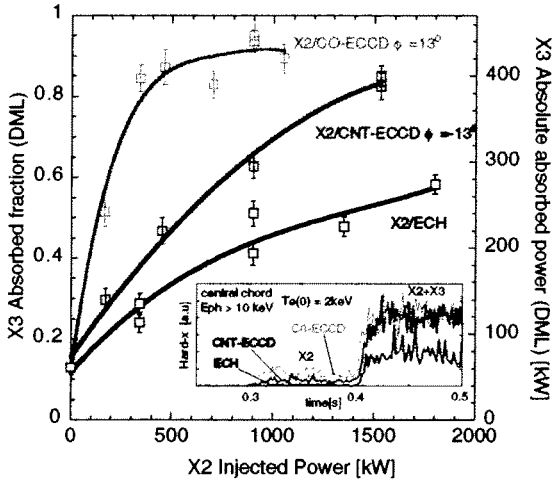

Fig. 2 Measured X3 absorption using the DML versus X2 preheat power for three different X2 launching configurations:

- *CO-ECCD (ϕ=13°),*
- *CNT-ECCD (ϕ=-13°)*
- *and ECH (ϕ=0°).*

The 3rd harmonic injected power was kept constant at 0.47MW with central deposition and zero toroidal injection angle (ECH).

The insert shows a comparison of the hard x-ray signal for the three launching configurations and for equal injected power of X2 and X3 (470kW)

angle (from central to off-axis) has demonstrated that single-pass absorption is measured with the DML diagnostic.

As shown in Fig. 3, a detailed toroidal injection angle scan of the X2 launch, with $P_{X2} \approx P_{X3}$=0.47MW, has revealed a clear asymmetry in the X3 absorbed fraction. The measured X3 absorption (blue curve) is highest in a target plasma with X2 injected at a toroidal angle of ϕ=13°, corresponding to CO-ECCD. The calculated absorption with the linear ray tracing code TORAY[4] (red curve) assumes an isotropic Maxwellian distribution function.

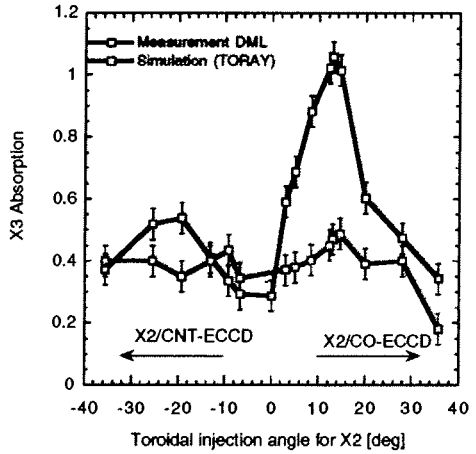

Fig. 3 Measured absorption with DML (blue curve) and calculated absorption with TORAY (red curve) versus X2 injection angle. The X2 and X3 injected power are equal at 470 kW. The TORAY code is runned using an isotropic Maxwellian distribution function.

For the largest toroidal angle in CO-ECCD (ϕ=36°), significant refraction of the X2 wave is occurring with a resulting X2 absorption of 38% only (TORAY). For all other toroidal angles, full absorption of X2 is predicted.

For this same toroidal angle scan, the variation of the plasma bulk parameters measured by Thomson scattering such as central electron temperature and density are shown in Fig. 4.

The red curves are measured during the X2 preheating phase (0.3-0.5s) while the blue curves are measured with the X3 power applied. As mentioned previously, the poor absorption of the X2 power at ϕ=36° is consistant with the significantly lower bulk temperature already during the X2 preheating phase. The slight central density reduction once the X3 power is applied (CO- and CNT-ECCD) is due to pump out effects observed on the density profiles. The strong asymmetry in the measured absorption observed in Fig. 3 can also be seen on the bulk plasma parameters during the X3 heating. Note that this is reflected in the TORAY results (Fig. 3) but still not sufficient to account for high absorption.

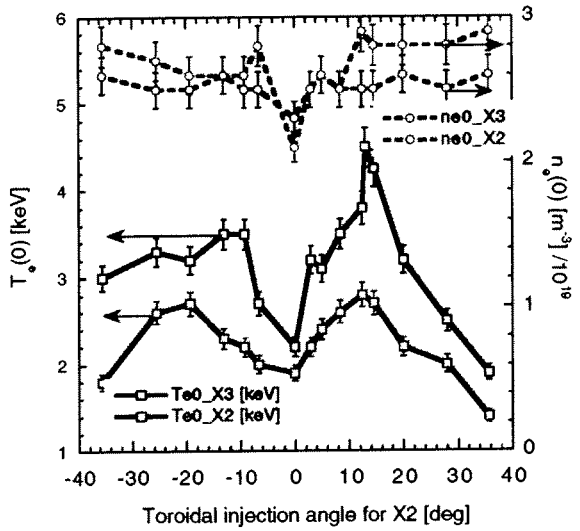

Fig. 4 Fitted central electron temperature and density mesured by Thomson scattering versus toroidal injection angle. The X2 and X3 power are as in Fig. 3. The red curves are measured during the X2 preheating phase(0.3-0.5s) while the blue curves are measured with the X3 power applied.

The Ohmic electric field effect on the X3 power absorption is shown in Fig. 5 where via a plasma current scan from 130kA to 230kA, the loop voltage was varied in the range 0.23-0.55V (green curve). With the X2 preheating in CO-ECCD at $\phi=13^o$, a substantial decrease in the absorption of the X3 wave is observed as the loop voltage is reduced (blue curve). Moreover, as the loop voltage is decreased, the difference between the measured absorption and the one predicted by TORAY is significantly reduced as well.

4. Discussion

Calculations of the theoretical absorption with the ray tracing code TORAY, using an isotropic, Maxwellian velocity distribution, are in fair agreement with the experimental results corresponding to ECH preheating. This observation is also in agreement with X3 absorption measurements by Pachtman et al. [5]. However, the measured X3 absorption exceeds that predicted by TORAY by a factor of up to 2 for the CNT- and CO-ECCD cases. A likely explanation of the discrepancy is that a large fraction of the X3 power is absorbed by energetic tail electrons created by X2 ECCD. The presence of these tails is confirmed by the measurement of photon spectra using an energy resolving hard x-ray camera (Figs.1 and 2 (insert)) and a high field side ECE radiometer (Fig. 6). The high-field side ECE radiometer detects suprathermal radiation levels several times larger than the thermal level, while effective x-ray photon temperatures of tens of keV are measured in the presence of ECCD. The radiometer time traces in Fig. 6 show that during the X2 preheating (0.3s<t<0.5s), no suprathermal electrons are generated for the quasi-ECH case (left figure), since the signals are

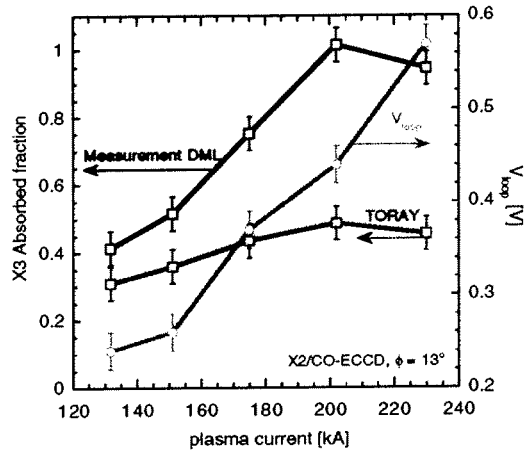

Fig. 5 Loop voltage dependence of the X3 absorption with X2 preheating in CO-ECCD at $\phi = 13^o$. The loop voltage scan has been performed by varying the plasma current (green curve). The blue curve is measured with the DML and the red curve gives the X3 absorption predicted by TORAY.

consistent with Thomson, on the contrary, for the CO-ECCD case, a significant deviation from Thomson is observed which indicates that a suprathermal electron tail is present. Comparing the two radiometer channels in the two cases (quasi-ECH and CO-ECCD) one can deduce that the suprathermal electrons are spatially located between the normalized minor radii r/a = 0 and r/a = 0.5 since, for the off-axis channel (red traces), the deviation from Thomson is very weak during the entire plasma discharge.
For an equal injected power of X2 and X3 (470kW), in the insert of Fig.2 a time trace of photon energies above 10keV is shown for the three different cases (CNT-ECCD, ECH, CO-ECCD). The photon counts and the ECE radiometer, are consistent in showing a weaker generation of suprathermal electrons during the ECH preheating phase.

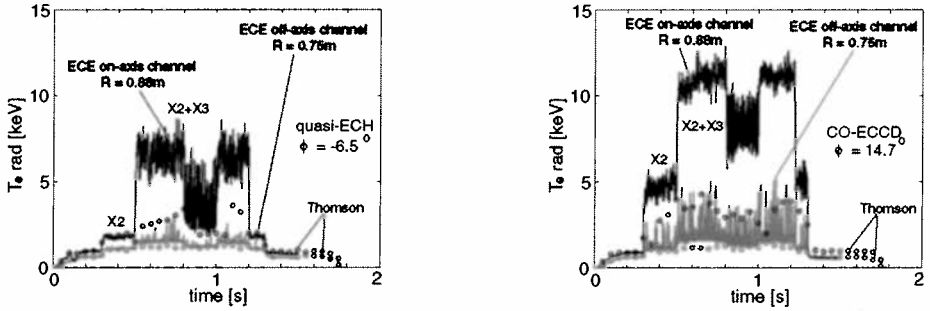

Fig. 6 Time traces of the high field-side ECE radiometer: left figure for quasi-ECH at ϕ = -6.5° and right figure for CO-ECCD at ϕ = 14.7°. In both figures, two radiometer channels are shown: a central view (R= 0.88m, blue curves) and an off axis view (R= 0.75m, red curves). All radiometer signals have been calibrated against the Thomson scattering diagnostic (circles) during the ohmic phase (t<0.3s). $P_{X2} \approx P_{X3} = 0.47MW$.

The bulk peak temperature (Te(0) = 2keV) measured by Thomson scattering during the X2 preheating (0.3-0.4s) is the same for the three cases. Also, in the ECH preheating case, the weaker suprathermal electron population is spatially located in an unfavourable region for enhanced X3 absorption due to the fact that the X2 cold resonance is placed far to the high field side of the X3 resonance whereas for ECCD is shifted outward by ≈ 25mm. Either or both of these mechanisms might explain the low absorption observed in Fig. 3 around $\phi = 0^0$.
The toroidal angle asymmetry suggests that the Ohmic electric field plays an important role in shaping the energetic tail electron velocity distribution. This hypothesis is confirmed by ECE, hard x-ray and absorption measurements in a loop voltage scan in the range 0.23-0.55V, obtained by varying the plasma current from 130-230 kA, with $\phi = 13^0$. Absorption decreases significantly as the loop voltage is reduced. Detailed analysis of the experimental data, as well as calculations of self-consistent distribution functions by means of a Fokker-Planck code, are in progress.

Acknowledgement: This work was partly supported by the Swiss National Science Foundation. The hard x-ray camera is on loan from the Tore Supra group (CEA,Cadarache).

References:

[1] S. Alberti et al., to be published in Fusion Engineering Design.
[2] J.-L. Segui et al., Nuclear Fusion, Vol. 36, No. 2 (1996).
[3] T. P. Goodman et al., Proc. of 19th Symp. On Fusion Technology (Lisbon, 1996) vol.1 Ed. C. Varandas and F. Serra (Amsterdam: Elesevier), p 565.
[4] A. H. Kritz et al. Proc. 3rd Varenna-Grenoble Int. Symposium on Heating in Toroidal Plasmas (Grenoble 1982) (Brussels: CEC) Vol.II, p.707.
[5] A. Pachtman, S.M. Wolfe, I.H. Hutchinson, Nuclear Fusion, Vol.27, No.8, (1987).

Evidence for the Need of Accurate Power Localization for Efficient Heating and Current Drive in TCV

T.P. Goodman for the TCV Team

Centre de Recherches en Physique des Plasmas
Association EURATOM-Confédération Suisse
Ecole Polytechnique Fédérale de Lausanne
CH-1015 Lausanne, Switzerland

email address of main author: timothy.goodman@epfl.ch

Abstract. The 6 beam 2nd harmonic X-mode (X2), 3MW, ECH/ECCD system of the TCV tokamak allows a fine tailoring of the deposition profiles in the plasma. The sensitivity of the sawtooth period to the deposition location is used to increase the equilibria reconstruction and ray-tracing accuracy. Off-axis ECH, followed by on-axis counter-ECCD produces improved central confinement regimes in which τ_{Ee} exceeds RLW scaling by a factor of 3.5. The PRETOR transport code (incorporating an RLW local transport model but constrained by the experimental density profiles) predicts an extreme sensitivity of τ_{Ee} to the deposition location of the counter-ECCD. This is confirmed by experiments. Sawtooth simulations using PRETOR, including the effects of current drive with inputs from the TORAY ray-tracing code, are in good agreement with experimental results. These results are an initial benchmark for the package of analysis codes, LIUQE / TORAY / PRETOR used during ECH/ECCD experiments on TCV.

1. Introduction

The Tokamak à Configuration Variable, TCV, ($R_0 = 0.88$m, $a < 0.25$m, $B_T < 1.45$T, $I_p < 1.2$MA, $\kappa_{vessel} = 3$) is a medium-size device designed to study the influence of plasma shape on plasma stability and confinement. The only auxiliary heating capable of accessing all possible plasma shapes (e.g. $1.0 < \kappa_{achieved} < 2.8$ and $-0.7 < \delta_{achieved} < +0.7$) in the device is Electron Cyclotron Heating (ECH).

The auxiliary heating system of TCV is not limited to heating alone; but, is designed to provide an extremely flexible delivery system of antennas - or, "launchers" - capable of Electron Cyclotron Current Drive (ECCD), as well. The launchers have two degrees of freedom allowing the beams to be swept in a plane during a plasma shot: the plane of the sweep can be rotated between shots. In the usual setup, the plane of the sweep coincides with the poloidal plane of the tokamak and the rotation angle of the plane is used to introduce a toroidal injection angle for ECCD.

Although many present day plasma devices (both tokamaks and stellarators) are equipped with multi-source ECH systems, most often the power from several gyrotrons is combined in the launchers leaving a small number of independent beams in the plasma. In TCV the system consists of six 82.7GHz, 2.0s gyrotrons coupled to 6 independent launchers delivering a total of 2.7MW of power at the 2nd harmonic in X-mode (X2). In addition, three 118GHz, 210s gyrotrons are to be combined in one launcher at the top of the machine, providing 1.5MW of heating at the 3rd harmonic in X-mode (X3) in 2001. This frequency and launching configuration allows central heating at higher density than for X2 and has a high optical depth at the resonance. At present, a 118GHz gyrotron has been used with an X2 launcher for initial absorption tests [1].

With independent launchers, good alignment of the beams is crucial. Conversely, once precise aiming is confirmed, detailed comparisons between theory and experiment become possible. This paper is concerned with just such comparisons. In section 2, we discuss the alignment of the launchers and implications for the LIUQE [2] reconstruction code. A comparison of high temperature, improved central confinement (ICC) regimes [3,4] with the PRETOR [5] transport code is then given in section 3 and results of the successful simulation of experimental sawteeth by the sawtooth crash model [6] incorporated in the code, in section 4. Section 5 describes stable, sustained, fully non-inductive, ECCD plasma experiments, possible only with well aimed independent beams. Concluding remarks are made in section 6.

2. Reproducibility of the plasma/launcher geometry

To properly analyze the effects of ECH and ECCD on the TCV plasmas a good knowledge of the power deposition and current drive profiles is needed. This in turn requires an accurate overall reconstruction of the magnetic equilibrium and ray-tracing. These calculations are carried out using the LIUQE and TORAY [7] codes, respectively. Considerable work has been carried out to simplify the interface between the codes so that a typical 2s TCV shot can be analyzed and displayed graphically within 5-10 minutes.

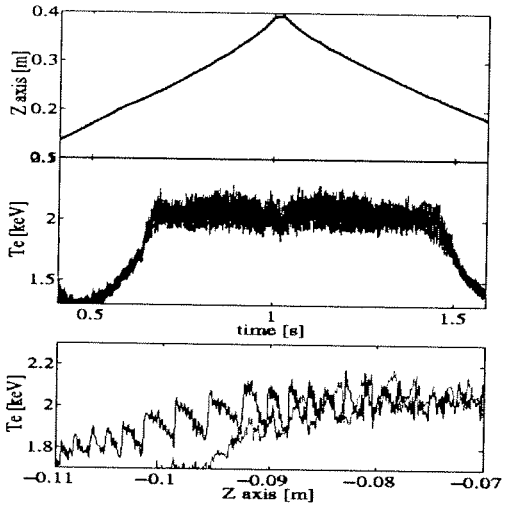

Fig. 1 The Plasma is swept through a stationary beam. The region of large sawteeth is displaced ~1.3cm when sweeping in opposite directions. The displacement is in the direction of the beam motion relative to the plasma center.

The accuracy of the overall reconstruction has been improved using measurements taken during sweeps of the plasma through the beam. In particular, the sawtooth period is highly sensitive to the power density close to the q=1, resulting in an effective spatial resolution smaller than the beam spot size and all of our present plasma diagnostics (mm vs. cm). This sawtooth response is very reproducible and the location of maximum sawtooth period is used as a target, to make a relative alignment between launchers to within ± 3mm [8,9]. This technique can thus provide an additional check on the magnetic reconstruction which helps improve the overall accuracy of ray-tracing results by showing the need for, and justifying the use of, tighter geometrical and numerical constraints in the code. Whereas ± 20mm accuracy in the Z_{axis} was previously acceptable in Ohmic discharges, this leads to excessively large errors in the deposition location calculated by ray-tracing.

Care must be taken to avoid confusion when moving the beams relative to the plasma (or vice verse) due to possible hysteresis effects. The hysteresis is often of the order of the error bars on the improved reconstruction and it is tempting to attribute the small differences in position of the large sawteeth to a residual error in the beam or plasma location. Figure 1 shows a situation in which the sweep direction appears to affect the location of the q=1 surface, near which the large sawteeth occur: A 1.3cm shift in the large sawtooth region is evident. This difference is small compared to the 3-4 cm resolution of diagnostics but would require only a 6mm error in the beam/plasma location to remove it altogether. Nevertheless, similar hysteresis has been confirmed with swept beams, plotting the sawtooth signal as a function of the launcher angle, i.e. independent of any reconstruction or ray-tracing. The hysteresis is also

reproduced by PRETOR. These high resolution, reproducible results give us confidence that small, systematic changes in the launching angles can indeed be responsible for some of the significant changes in confinement observed during on-axis counter-ECCD - although the resolution of the ray-tracing is still limited. An example in which the limited resolution of the analysis codes prompted such systematic experiments, is that of the ICC regime.

3. The Improved Central Confinement Regime

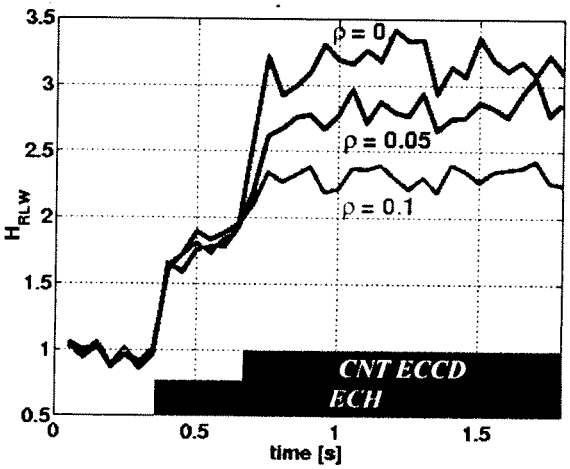

Fig. 2 Small changes in the deposition location, ρ, of central counter-ECCD in the ICC regime lead to large changes in global confinment,

The predictive, 1D, time dependent, transport code PRETOR, coupled with a 2D equilibrium solver and incorporating a Rebut-Lallia-Watkins (RLW) local transport model, has been validated on a wide variety of TCV L-mode plasmas [10]. When coupled to the TORAY code (for the power and driven current source terms), it successfully reproduces the evolution of the temperature profiles in many cases with auxiliary heating. Global RLW confinement scaling is appropriate for our low-n_e, high T_e/T_i plasmas [10], but is often exceeded for high-power central deposition[3,4]: A good figure-of-merit for these plasmas is the ratio $H_{RLW} = \tau_{exp.}/\tau_{RLW}$. The ICC regime is produced by a two step process: *1)* off-axis ECH is used to broaden the profiles and lower the central heat conductivity while maintaining the plasma stability when *2)* strong counter-ECCD is added, after ~300ms, on-axis[4]. PRETOR does not always successfully reproduce the experimental temperature evolution when taking the TORAY inputs as source terms. However, the code can be run in a "diagnostic mode", in which *both* the n_e and T_e profiles are imposed and steady-state conditions (constant V_{loop}) are assumed. In this case, the deposition location is varied within the range permitted by the errors in the profile measurements, and a wide variety of current profiles and, therefore, safety factor profiles are obtained. These results highlight the extreme sensitivity of plasma performance to variations in the ECCD location, smaller than the accuracy or TORAY, and specifically suggests that exact on-axis counter-ECCD is crucial in producing the high temperatures and high confinements characteristic of this regime [11]. Figure 2 shows that this prediction is confirmed by experiments, in which changes of a few centimeters (as little as $\Delta\rho$~0.05) cause ~15% changes in global confinement H_{RLW} factors.

4. Sawtooth simulations

PRETOR also includes a sawtooth crash model which has been used to successfully reproduce [11] the results of experiments in which the sawtooth period was found to depend on the local driven current as well as the power density near the q=1 surface [12]; an observation which, in turn, was used to put in evidence the asymmetric nature of off-axis current drive due to the poloidal field [8,9]. The sawtooth crash criterion included in the model can be written as $s_1 > s_{1\,crit}$, where s_1 is the shear in the profile of the safety factor at q=1 and $s_{1\,crit}$ is a critical value of shear above which the sawtooth instability is triggered. The density and temperature profiles are flattened out to the mixing radius after the crash. The q profile is relaxed according to the Kadomtsev model for full magnetic reconnection. The

value of s_{1crit} contains a free parameter which is adjusted for a given experiment so that PRETOR reproduces the sawtooth period measured during the Ohmic phase: all free parameters are then fixed.

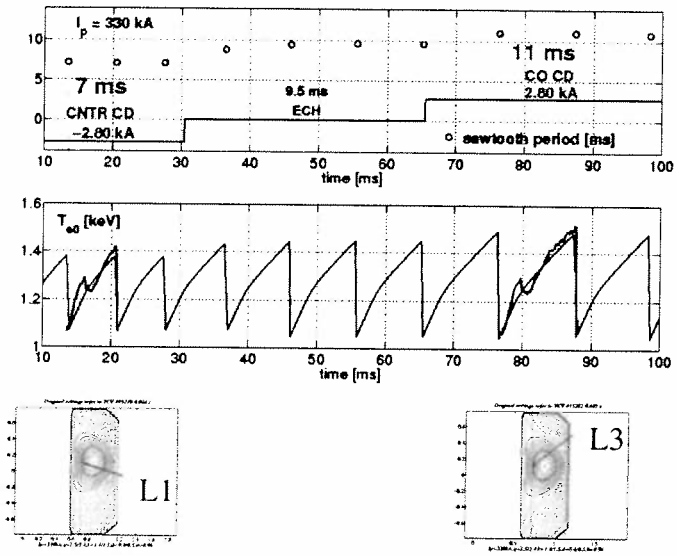

Fig. 3 Small changes in the local current drive (<1% of total current) cause measurable changes in the sawtooth period; an effect well reproduced by the sawtooth model used in PRETOR.

It is found that special care must be taken to reproduce the experimental situation when modeling sawteeth since all aspects found in experiments are important to the results: power density, sweep direction, current drive direction and magnitude. The model is however 1D and cannot reproduce features related to non-axisymemetric processes; e.g. magnetic islands. An example of a simplified case is shown in figure 3. In this situation, the beam location was fixed; however, different launchers were used in the two shots shown. The projection o the beam **k**-vector onto the poloidal field is different in the two cases, producing opposite driven currents; counter-ECCD in the case on the left and co-ECCD in the case on the right. A measured x-ray signal is superimposed on the simulated central temperature (scaled in the vertical, but not the horizontal, direction): the periods are in good agreement.

5. Fully non-inductive ECCD driven operation

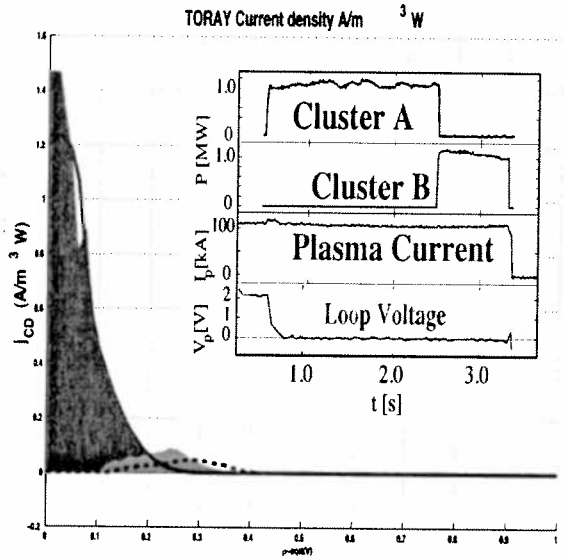

Fig. 4 Stable replacement one set of 2 beams, with another. This allows the pulse to be extended and demonstrates that exact beam overlap is not required. (blue - Launchers 1 & 3; red - Launchers 5 & 6).

The 6 independent beams allow a fine tailoring of the deposition profiles in the plasma and have allowed stationary fully ECCD driven plasmas to be produced in which the Ohmic transformer coil current I_{OH} is kept constant by the feedback system, rather than I_p, and the plasma has settled to the shape determined by the combination of the feed forward shaping-coil currents and the ECCD profiles - a process of current redistribution lasting several 100ms. In this mode of operation, the pulse length is determined by the gyrotron pulse length of 2s provided that the distribution of current sources is broad enough to prevent overpeaking of the profiles which otherwise lead to a disruption on an ideal-instability time scale. Up to 210kA have been driven in this way using all 6 gyrotrons [13].

As the total plasma current can be maintained non-inductively with as few as 2 beams, the sensitivity of the overall driven current to the profiles can be shown by switching from one current distribution to a slightly different one. This is done by replacing one pair of beams by two others with a 5ms overlap. The resulting 2.8s full ECCD plasma is shown in figure 4. This proof-of-principle experiment shows that it is possible to switch drivers during a pulse; something necessary in a reactor where one source may need to be taken off-line and be replaced by another. Since the plasma disrupts only after a few 10's of milliseconds if the gyrotrons are turned off, it should be possible to replace a source which has tripped off due to a malfunction, with another within this time. The fact that the sources are not exactly equivalent in location shows that small errors in alignment do not preclude a stable switch over. However, other, similar shots do disrupt. With the continual improvements being made in our analysis package, the differences between these shots should be able to be resolved.

6. Conclusions

Swept beam experiments have allowed (a) refinement in magnetic reconstruction analysis which in turn (b) reduces the errors in ray-tracing calculations and so (c) increases confidence that small differences in beam aiming can lead to large changes in plasma confinement as predicted by PRETOR. Careful experiments in the ICC regime confirm this with 15% decreases in confinement occuring for 5% displacements of deposition. Thus, the interplay of experiment and theory has resulted in methods of experimental design and analysis, using a package of codes and diagnostics, which increase our ability to properly study and predict the behaviour of ECH and ECCD dominated experiments, such as fully sustained ECCD plasmas.

Acknowledgment: This work was partly supported by the Swiss National Science Foundation.

References:

[1] ALBERTI, S., et al., post-deadline, this conference
[2] HOFMANN, F. and TONETTI, G., Nucl. Fusion **28** (1988) 1871.
[3] PIETRZYK, Z.A., et al., Phys. of Plasmas **7** (2000) 2909.
[4] PIETRZYK, Z.A., et al., subm. to Phys. Rev. Lett. and Lausanne Report LRP 678/00 (2000)
[5] BOUCHER, D. and REBUT, P.H., in *Proc. IAEA Tech. Conf. on Advances in Simulation and Modelling in Thermonuclear Plasmas*, 1992, Montréal (1993) 142.
[6] PORCELLI, F., et al., Plasma Phys. Contr. Fusion **38** (1996) 2163.
[7] SMITH, G.R., et al., in *Proceedings of the 9th Joint Workshop on ECE and ECRH, Borrego Springs, CA, 1995* (World Scientific, Singapore, 1995), p. 651.
[8] GOODMAN, T.P., et al., in *Proceedings of the 26th EPS Conf. on Contr. Fusion and Plasma Physics, Maastricht, 1999*, ECA (European Physical Society, Mulhouse, 1999), Vol. 23J, 1101.
[9] HENDERSON, M.A., et al., to be published in Fusion Engineering Design.
[10] POCHELON A. et al, Nucl. Fusion **39**, No 11Y (1999) 1807
[11] ANGIONI C. et al., to be published in *Theory of Fusion Plasmas, Varenna 2000* (Bologna: Editrice Compositori) and Lausanne Report LRP 682/00 (2000)
[12] GOODMAN T.P. et al., in *International Congress on Plasma Physics & 24th EPS(Proc. Cong. Prague, 1998),* (European Physical Society, Geneva, 1998), Vol. 22c, 1324.
[13] CODA, S., et al., to be published in Plasma Phys. Contr. Fusion

ELMing H-mode Accessibility in Shaped TCV Plasmas

Y.R. Martin and TCV Team

Centre de Recherches en Physique des Plasmas, Association EURATOM - Confédération Suisse, Ecole Polytechnique Fédérale de Lausanne, CH-1015 Lausanne, Switzerland

e-mail address of main author: Yves.Martin@epfl.ch

Abstract. The H-mode regime is easily reached with ohmic heating only in a wide range of TCV plasma parameters. However, the plasma usually enters an ELM free H-mode phase after the LH transition, leading to a high density disruption. Therefore, the access to a stable ELMy regime requires an LH transition directly leading to an ELMy phase. A "gateway" to the ELMy regime was found in TCV ohmic discharges. Although small in terms of plasma control parameter ranges, this "gateway" is well defined and robust against changes in wall conditioning for instance. Once in the ELMing regime, the plasma was successfully driven in a much wider range of plasma parameters, whilst remaining in this better confinement mode.

1. Introduction

Future fusion reactors like ITER are planned to operate in the ELMy H-mode regime. The H-mode is desired because of its high confinement properties and ELMs are necessary to control the plasma density and plasma impurities. ELMs, however, represent a threat to the divertor plates because of the deposited heat flux if the delay between ELMs becomes too large. Therefore, the identification of the plasma parameters which can control the ELM frequency is necessary. The strong shaping capabilities of TCV can be used to investigate the effect of plasma shape and position with plasma parameters on the ELM activity. On TCV, additional heating can not, as in other machines [1, 2 and references therein], be used to access a desired ELMing regime. Thus, other machine or plasma parameters must be found.

H-mode have already been obtained in ohmic TCV discharges with a large variety of plasma shapes, currents and densities. A large number of these discharges had an ELM free H-mode phase while some, seemingly similar discharges, exhibited ELMs. The goal of this study was to determine the conditions necessary for the production of a stable ELMy H-mode. These discharges could subsequently be used to study the plasma behaviour and ELM dynamics in an ELMing regime.

In this investigation, the plasma current, density, elongation, triangularity, plasma to wall gaps, divertor geometry and toroidal magnetic field were scanned. A single null divertor with the ion grad B drift directed away from the X point was chosen for these experiments. This configuration has been extensively used in previous experiments and led to most of the ELMy discharges previously observed on TCV. An ELM free H-mode period on TCV results in the plasma density increasing until the discharge terminates by a high density disruption. Since many such discharges had already been obtained, plasma parameters leading to this regime could be avoided. In the same way, discharges in this configuration which remained in L-mode were also avoided. From database studies of TCV discharges, ELMs were expected for plasma parameters between these limits.

It was found that an ELMy regime could be obtained by passing through a small but well defined region of the operational domain. Surprisingly, large changes in the machine condition-

ing, (including a boronisation) did not significantly affect the position of this "gateway" which was used to reliably access an ELMy TCV regime, as described in next section. Once in the ELMy regime, the plasma was found to be relatively robust to changes in the current, shape and density. It was thus possible to access a wider range of plasma parameters whilst remaining in an ELMy regime. A subsequent section describes the operational boundaries of the established ELMy regime and the limiting operational parameters.

2. The "Gateway" to the Ohmic ELMing Regime

This section first presents how the boundaries of the ELMy "gateway" were determined. The plasma discharges in this study were tagged with one of the labels: ELMY for stationary ELMy discharges, LMODE for discharges remaining in L-mode, ELMFREE for discharges which transited to an ELM free phase, ELMYL and ELMYELMFREE were attributed to discharges alternating between the two modes and ELMYFAIL was attributed to discharges disrupting shortly after the transition, for which the mode was unknown. Example discharges for these labels are shown in Fig. 1. The non stationary ELMing discharges were classified in two categories: discharges which ceased to be ELMy soon after the L-H transition and discharges whose ELM frequency became irregular as a result of programmed changes in some of the plasma parameters.

To pass the "gateway" to the ELMy regime, three parameters must simultaneously exceed a threshold value to obtain an H-mode: a) the plasma current has to be greater than 350kA or equivalently q_{95} must be lower than 3.0 with κ=1.6-1.7 and δ=0.5-0.6 as shown in Fig. 2a; b) the plasma line average density must exceed $4.5 10^{19} m^{-3}$,as shown in Fig. 2b; c) the distance between the plasma and the tiles must be greater than 1cm. The inter-dependencies between these limits were small. With the same plasma shape parameters, the plasma current must not

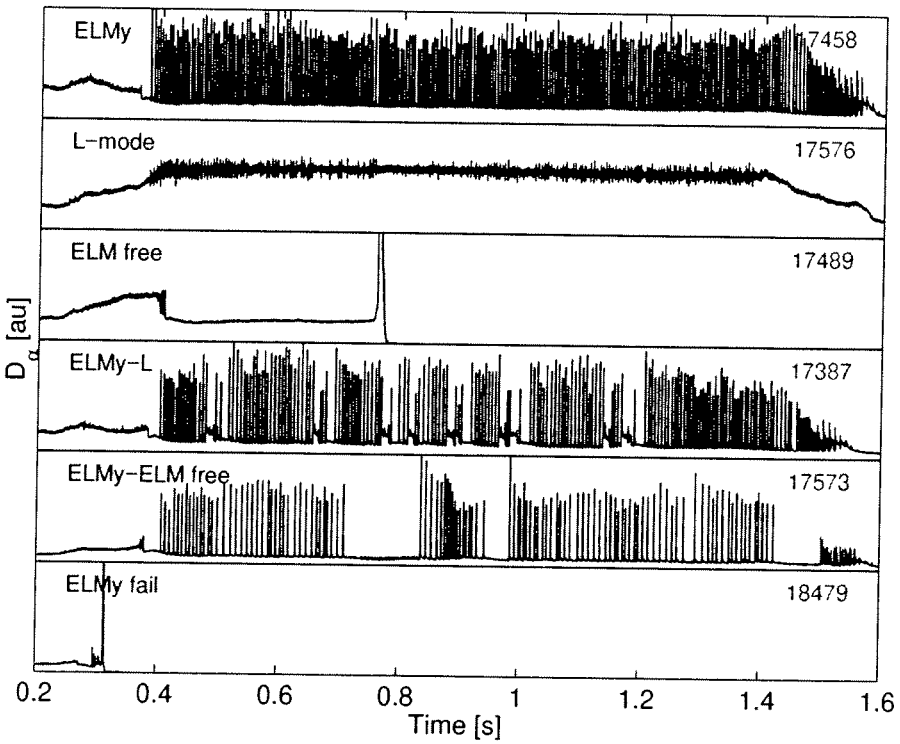

FIG. 1. Time evolution of the D_α emission from different type of discharges as indicated on the left.

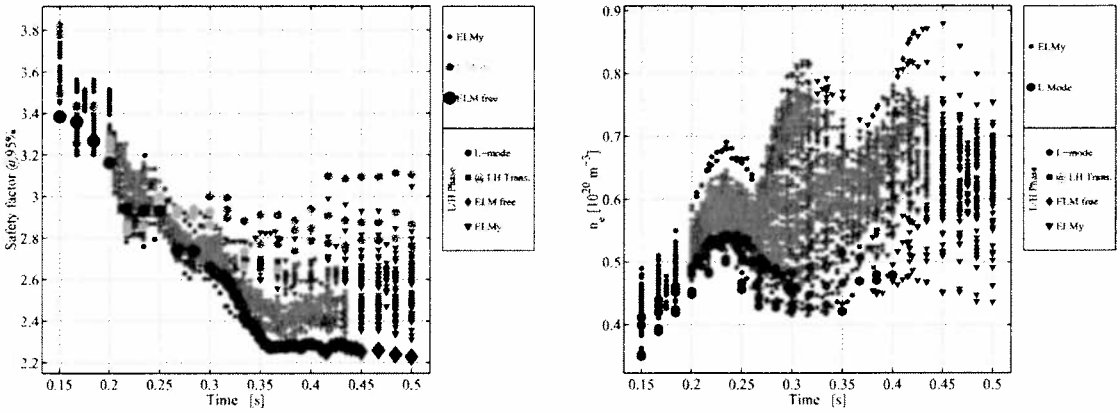

FIG. 2. a) Time evolution of the safety factor for L-mode, ELMy and ELM free shots indicating the available range in q_{95} to access the ELMy regime. b) Time evolution of the plasma density for L-mode and ELMy shots indicating the lower boundary to access the ELMy regime.

exceed 430kA (or q_{95}<2.3) otherwise the transition leads to an ELM free phase. A high density (> $6.10^{19}m^{-3}$) at the transition also led to an ELM free phase.

LH transitions were also provoked at higher plasma elongation (in the range 1.7 to 2.1) by retarding the formation of the SND configuration. In otherwise similarly shaped plasmas with similar densities, the L-H transition was obtained at higher q_{95}, with roughly equal values of plasma current. However, these transitions led to ELM free H-modes. A reduction in the plasma density at the L-H transition time resulted in L-mode discharges. Minor changes in the plasma shape at higher q_{95} sometimes resulted in ELMs but with low frequency and high amplitude. The resulting perturbation in the control system was sufficient to lose vertical plasma position control and a disruption (VDE) ended the discharge. Changes in the control observers are being developed to improve this situation [3] which, for this paper, limited the maximum plasma elongation.

In summary, the "gateway" to the ohmic ELMy is bounded by the following limits in the operational parameters:

	I_p [MA]	$n_e[10^{19}m^{-3}]$	κ	δ	gap_{pl-w}[m]
Min	0.35	5.0	1.6	0.5	0.01
Max	0.43	6.5	1.7	0.6	0.03

3. The Operational Domain of the Ohmic ELMy Regime

Once in the ELMy regime, it was then possible to modify certain plasma parameters while preserving the ELMs. The plasma elongation was increased to κ=2.1, with q_{95} approximately constant, as shown in Fig. 3a. Changes in q_{95} during the elongation ramp resulted in vertical stability problems. Decreases in q_{95} lowered the ELM frequency, as mentioned above, where-

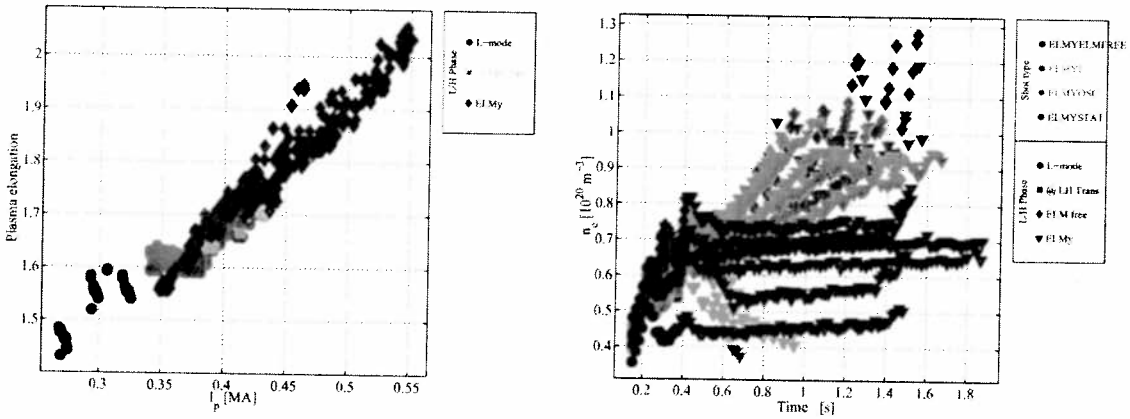

FIG. 3. a) Time evolution of the ELMy discharges in the I_p/κ plan. The first stages of the discharges are in L-mode in the lower left corner and at the LH transitions in the centre of FIG. Then it was possible either to increase or decrease the plasma elongation at constant q_{95}. whilst remaining in the ELMy regime. b) Time evolution of the plasma density for ELMy shots. Stable ELMy shots are accessible in a limited range of plasma densities. A strong increasing density leads to oscillations in the ELM frequency or even to appearance of ELM free phases. Reduction of plasma density below a threshold at $4.10^{19}m^{-3}$ leads to a return in L-mode regime.

as increases in q_{95} made the plasma less vertically stable. Moreover, the plasma current must be ramped sufficiently slowly, or the discharge showed spontaneous H-L-H transitions regime or even returned to L-mode for higher values of dI_p/dt. The ELMing regime was also kept while the plasma elongation was reduced down to k=1.55. It is worth noting that no L-H_{ELMy} transition was observed at this elongation exhibiting the hysteresis behaviour of the H-mode accessibility.

Once in ELMy H-mode, the plasma density can be decreased or increased in the range between $4\text{-}10.10^{19}m^{-3}$, as shown in Fig. 3b. A strong gas puff led to either oscillation in the ELM frequency or to alternating ELM free and ELMy phases. Trials to reduce the density below $4.10^{19}m^{-3}$ finally led to returns in L-mode.

Modifications in the plasma triangularity were also performed on ELMing plasmas whilst keeping other parameters fixed, see Fig. 4a. Discharges remained in stationary ELMing regime in a short range of plasma triangularity. At a triangularity higher than 0.65, the discharge shows oscillations in the ELM frequency or even the appearance of short ELM free phases. Contrarily, at low triangularity, $\delta<0.45$, the plasma suffers a back transition and returns in L-mode. LH transitions to ELMy or ELM free H-mode occur much more easily when the plasma wall distance is larger than 1 cm. However, this plasma wall distance can be reduced to values below 1cm, again without losing the ELMing regime, as shown in Fig. 4b.

Finally, the toroidal field was reduced during the ELMy phase. In one scenario, the safety factor was kept constant during the B_t ramps. In the other, the plasma current was maintained. Small reduction of B_t did not affect the ELMing regime for both scenarios. Stronger toroidal field decrease led to plasma disruptions for unclear reasons in case of constant q95 and to an oscillation between ELMy, ELM free and L-mode phases in the constant plasma current case.

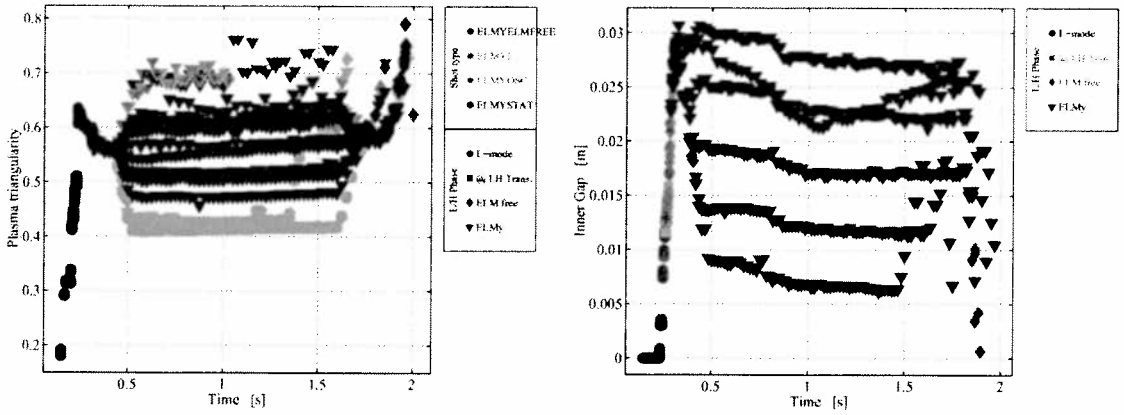

FIG. 4. a) Time evolution of the plasma triangularity for ELMy discharges. An increase of the triangularity leads to an oscillating ELM frequency or even to the appearance of ELM free phases. A reduction of the triangularity leads to a back transition to the L-mode. b) Time evolution of the plasma wall distance for ELMy shots. The gap was reduced to values below the threshold value without any deterioration of the ELMy regime.

4 Conclusion

A reliable ELMy H-mode regime was successfully obtained in TCV. Access to ELMy discharges was only possible for a small region of the operational domain. Once this "gateway" is traversed, the ELMing state is stable to changes in the operational parameters. Plasma elongations from 1.55->2.1, triangularities from 0.45->0.65, plasma wall distances from .5->3cm and densities from 4->10.10^{19}m^{-3} were successfully attained by passing the L-H transition with the "gateway" parameters and then programming plasma control changes. Although the ELM frequency was modified for these discharges, the ELMy regime characteristics were conserved.

Since the parameters under investigation in this paper were changed one at a time, it may be possible to extend even more theses ranges by compensating the effects of one parameter with changes in the other plasma parameters. The reliable access to the ELMy regime on TCV, together with the systematic changes in ELMing phases characteristics within parameter scans, open the way for the study of ELM dynamics and plasma confinement in this regime, both with and without ECH as a function of the plasma shape.

Acknowledgement: This work was partly supported by the Fonds National Suisse de la Recherche Scientifique. This work would not have been possible without the support of the entire TCV team.

References:

[1] H. Zohm, Plasma Phys. and Contr. Fusion 38 (1996), 105.
[2] W. Suttrop, Plasma Phys. and Contr. Fusion 42 (2000), A1.
[3] F. Hofmann et al. Proc 27th EPS conf. on Contr. Fus. and Plasma Phys, Budapest, 2000, p47.

Detachment in Variable Divertor Geometry on TCV

R.A. Pitts 1), A. Loarte 2), B.P. Duval 1), J.-M. Moret 1), J. A. Boedo 3), D. Coster 4), J. Horacek 5), A. S. Kukushkin 6) and the TCV team.

1) Centre de Recherches en Physique des Plasmas, Association EURATOM-Confédération Suisse, Ecole Polytechnique Fédérale de Lausanne, CH-1015 Lausanne, Switzerland
2) EFDA-CSU, Max Planck Institut für Plasmaphysik, D-85748 Garching, Germany
3) Fusion Energy Program, University of California, San Diego, CA 92093-0417, USA
4) Max-Plank-Insitut für Plasmaphysik, Boltzmannstr. 2, D-85748, Garching, Germany.
5) IPP, Academy of Sciences of the Czech Republic, Za Slovankou 3, POB 17, 182 21 Praha
6) ITER Joint Central Team, Garching Joint Working Site, Boltzmannstr. 2, D-85748, Garching, Germany.

email address of main author: richard.pitts@epfl.ch

Abstract. Although the requirement of shape flexibility in TCV precludes the use of fixed baffle or optimised divertor target structures, it does allow for the investigation of diverted equilibria not possible in more conventional tokamaks. One such single null configuration is simultaneously characterised by a very short inboard poloidal depth from X-point to strike point on a vertical target and an extremely long poloidal depth to a horizontal target on the outboard side. Density ramp discharges leave the inboard target plasma attached even at the highest densities, whilst clear partial detachment is observed at the outboard target. Modeling of this configuration using the B2-Eirene code package shows that the outboard divertor achieves high recycling at very low densities, with the rollover to detachment occurring near the outer strike point very soon after the density ramp begins. An important result of the modeling effort is that, due to the low apparent densities in the TCV outboard divertor, the code cannot quantitatively reproduce the absolute level of observed detachment without artificially increasing fivefold the charged particle sink due to three-body and radiative recombination.

1. Introduction

An interesting aspect of certain diverted equilibria possible on the TCV tokamak is the geometrical contrast between inner and outer strike zones. This permits the influence of horizontal and vertical targets and short and long divertor poloidal depths to be investigated simultaneously with regard to their effects on the divertor plasma and in particular on detachment [1]. In addition, the relatively unconventional (with regard to most operating tokamaks) nature of these configurations makes them an interesting subject for code modeling. This has been performed for TCV data using the coupled B2-Eirene package [2] and some results are presented here along with experimental data.

2. Experiment

A typical density ramp discharge is summarised in Fig.1, along with three of the equilibria studied. All have κ_{95} = 1.6, δ_{95} = 0.35 and fixed height (57 cm) from outer target to X-point. In each case, I_p = 345 kA (q_{95} =

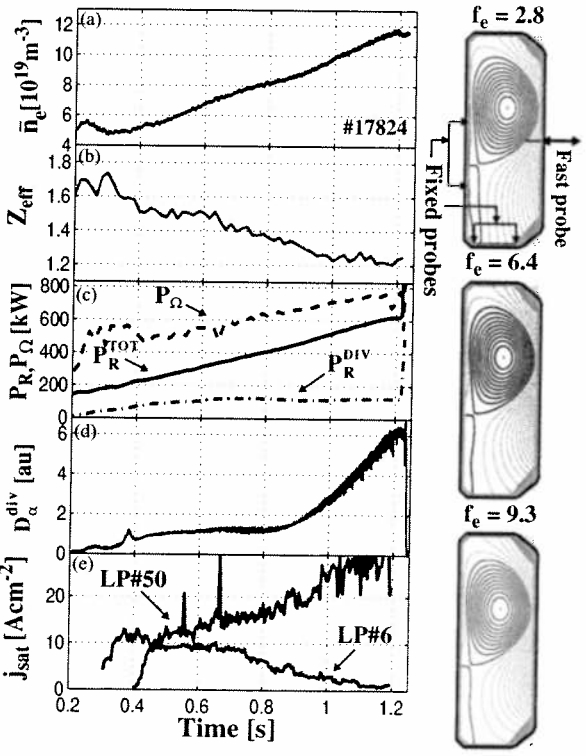

Fig. 1 Illustrating the time dependence of some relevant plasma sigals for a typical density ramp discharge for detachment studies.

2.9), with fixed flux expansion (≈ 4) at the inner target but variable at the outer strike zone in the range $f_e = 2.5 \rightarrow 10$. In what follows, f_e is taken to refer to this outer target flux expansion the variation of which can be clearly seen in the equilibria of Fig.1. All cases discussed here have unfavourable ∇B drift direction and are deuterium fueled density ramp discharges, leading invariably to an X-point MARFE but not necessarily to disruption ($\bar{n}_e \approx 65\%$ of the Greenwald limit at maximum). One may note the very low Z_{eff} (Fig. 1b) and the low level of divertor radiation (Fig. 1c), taken here to mean all radiation found below the X-point. Most of the former originates at the X-point since, even at the lowest densities in the ramp, the outer divertor is too cold for carbon (the dominant impurity in TCV) to radiate efficiently.

3. Results and Comparison with B2-Eirene Code Modeling

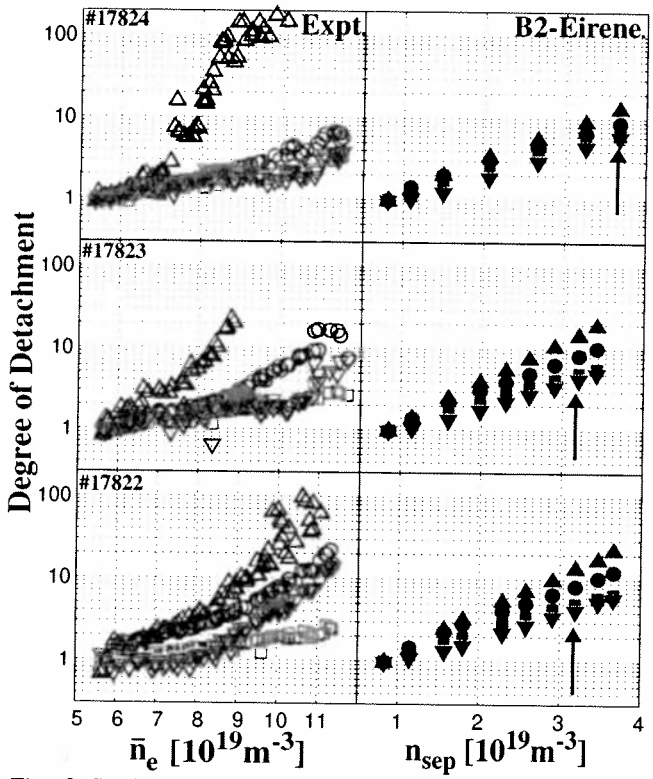

Fig. 2 Strike point and integral ion flux DOD's from experiment and B2-Eirene simulations as a function of density (main or separatrix) and outer target f_e. ○: Outer divertor, integral current, □: Inner divertor, integral current, Δ: Outer divertor, separatrix current density, ∇: Inner divertor, separatrix current density. The vertical arrows indicate the B2-Eirene run numbers corresponding to the D_α distributions of Fig. 5.

In what follows, code results are presented along with experimental data to facilitate comparison. In the former, the power crossing the separatrix, P_{SOL}, the chemical sputtering yield, Y_{chem} and the transport coefficients, $D_\perp$, $\chi_\perp$ have been fixed at 0.36 MW, 3.5% and 0.2 m^2s^{-1}, 0.9 m^2s^{-1} respectively for all densities and equilibria. These parameters are chosen so as to approximately match upstream profiles and target ion fluxes at the lowest densities in the ramp.

In Fig.1e the parallel ion flux densities measured by target Langmuir probes at the inner (probe 50) and outer (probe 6) strike points show that the inner target remains attached throughout the density ramp, whilst at the outer target a plateau value is already attained at divertor formation followed by a rollover to detachment at around $\bar{n}_e \approx 8x10^{19}m^{-3}$. This suggests that the outer divertor plasma rapidly accesses the high recycling regime and is close to detachment at the beginning of the density ramp. With increasing f_e, although a plateau region is always attained, detachment at the strike point occurs at progressively lower densities. This can be seen clearly in Fig.2 which compiles experimental and theoretical values of the Degree of Detachment [3], defined as $DOD = C\bar{n}_e^2/I_{sat}^{div}$ with I_{sat}^{div} the probe ion saturation current to the divertor target, expressed either as a peak value at the separatrix or an integral value across the target. The DOD's describe the extent to which the 2-point model [4] scaling $\Gamma \propto \bar{n}_e^2$ is obeyed, with DOD » 1 indicating detachment. As f_e increases, the outer target integral DOD progressively increases for given $\bar{n}_e$ indicating detachment right across the target. Except at the highest f_e and highest $\bar{n}_e$, the inner target remains largely attached everywhere. With the exception of the outer target separatrix DOD's, there is excellent agreement between the B2-Eirene predictions and experiment both in absolute magnitude and relative ordering amongst

the individual DOD's. However, and this is one important outcome of the code modeling effort, with the chosen run parameters, B2-Eirene is unable to match experiment in this way *without artificially increasing the rate coefficients for three body and radiative recombination by a factor of 5*. These pathways to recombination: $e+D^+ \rightarrow D_o+h\nu$ (radiative) and $e+e+D^+ \rightarrow D_o+e$ (3-body) are assumed to be the most important electron-ion recombination channels in operation for temperatures and densities common to most tokamak divertor plasmas [5]. Without increasing these reaction rates, insufficient recombination occurs for the observed degree of detachment to be reproduced. Even with this artificial modification, the code fails to reproduce the strong strike point detachment seen experimentally.

Experiment and theory are again compared in Fig.3, on this occasion in terms of scrape-off layer (SOL) and divertor profiles of T_e, n_e and electron pressure, p_e, measured with target probes and a fast reciprocating probe entering the edge plasma at the tokamak midplane (Fig.1). All profiles are mapped to the outer midplane at the magnetic axis of the equilibrium. In the very low density case, to the left of Fig.3, the experimental data indicate the divertor plasma to be in the low recycling regime with roughly equal upstream and downstream T_e and p_e. Agreement with code results is reasonable given that run parameters where not optimised

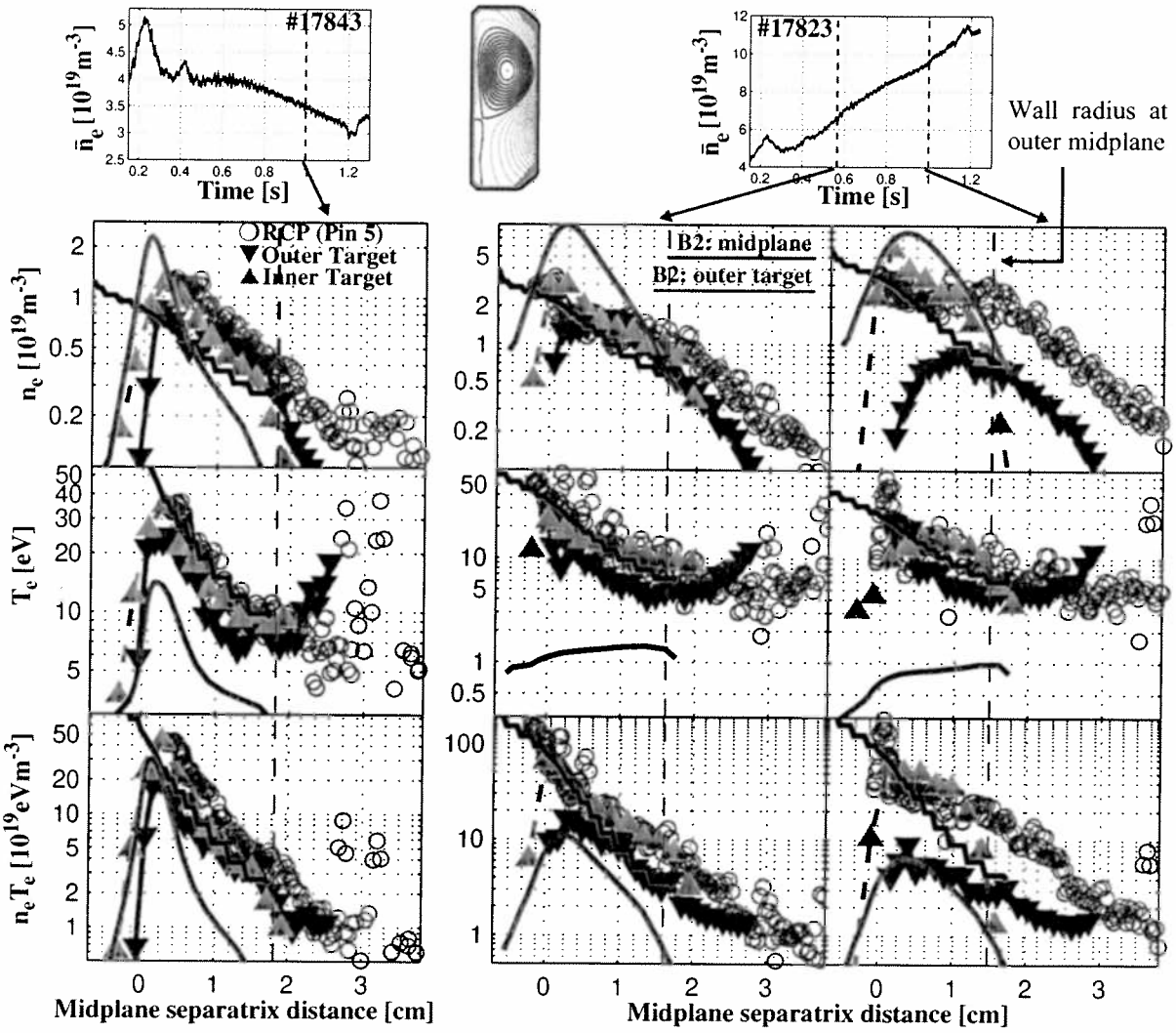

Fig. 3 Compilation of fast reciprocating and divertor target probe profiles mapped to the magnetic midplane for a very low density case (TCV #17843, left) and during a high density ramp discharge (TCV #17823, right). In both cases f_e = 6.4. B2-Eirene profiles for the outer target only are also included from runs approximately matching the observed midplane profiles.

for this case. At the beginning of the density ramp, when upstream profiles are approximately matched, one notes the large discrepancy in the values of simulated and measured outer target T_e. This is preserved at higher densities and in turn leads to large differences in density at the target when comparing theory and experiment. By coincidence, agreement is rather good with regard to p_e in the divertor. That the Langmuir probe measured T_e can be an overestimate of the true value is nothing new [6] and there are strong arguments for the case of the TCV divertor in support of significant deviations of the measured T_e from the real value local to the outer target under high recycling and detached conditions [7].

For the case of lowest flux expansion, Fig.4 illustrates the comparison between measured and simulated outer target perpendicular ion flux profiles (at low f_e, field line impact angles are sufficiently high as to avoid problems associated with probe shadowing by adjacent tiles leading to erroneous measured fluxes [1]). Whilst profile shapes are evidently less well matched, absolute values of maximum ion flux are in good agreement. With increasing separatrix density, the simulated ion flux increases and then begins to decrease, corresponding to a certain degree of separatrix detachment. But, as mentioned above, a charged particle sink sufficiently high for any significant detachment to occur (a maximum of 30% of the ion flux for the highest density B2 case in Fig.4) can only be obtained if recombination rate coefficients are artificially increased. Even this level of recombination is far from sufficient to reproduce the level of separatrix detachment seen in Figs.4 and 2 at the highest densities.

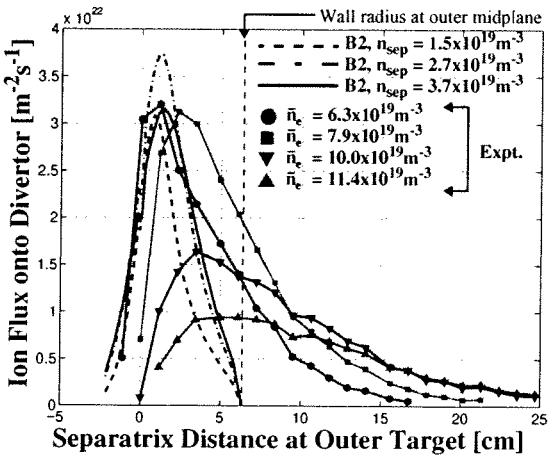

Fig. 4 Experimental divertor ion flux profiles at the outer target for low f_e (#17824) and four values of plasma density compared with B2-Eirene predictions at three values of model separatrix density.

As a further example of the comparison between experiment and simulation, Fig.5 compiles model predictions, at each value of f_e, of the 2-D distribution of D_α emission in the divertor and inverted emissivities from tangential CCD camera measurements of the same emission. The latter originates both from excitation and recombination processes. In the case of the experimental data, distributions are compared at discharge times (or, equivalently, values of $\bar{n}_e$) having approximately the same outer target integral DOD (Fig.2), whilst the model cases correspond to runs for which the level of total recombination is similar. Agreement is satisfactory with regard to the differences when passing from low to high flux expansion in the vertical extent of the emission. The indications are this is likely due to more uniform distribution of momentum losses further up the outer leg owing to the greater neutral transparency of a laterally "thinner" divertor. Code and experiment differ, however, with respect to the localisation of D_α emission at the target. Whilst the simulation places the highest intensity at the strike point and even into the private region, experiment shows the emission to be localized further out in the divertor fan, especially at high f_e. This behaviour is not currently understood but is most likely strongly linked to the inability of the code to reproduce the high degree of strike point detachment. One may also note in Fig.5 how the two extreme flux expansions are very similar from the point of view of code results. This is also reflected in other aspects of code output, particularly in the levels of recombination achieved at a given density.

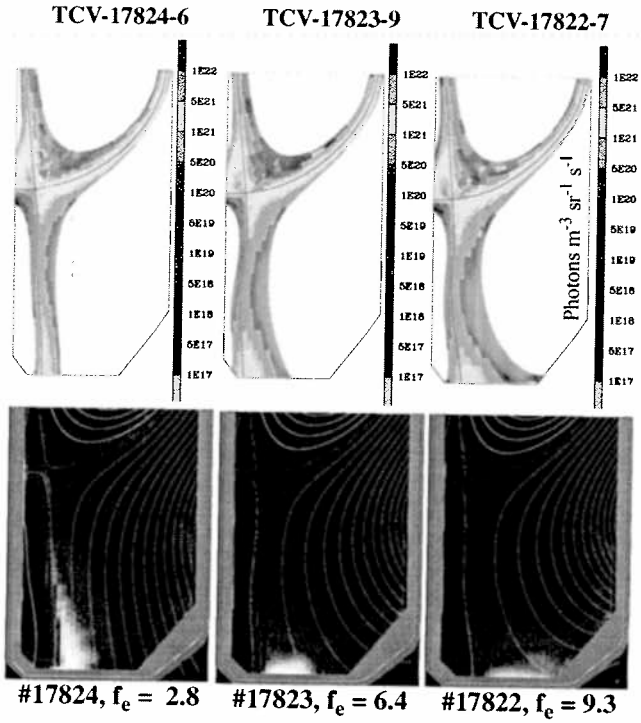

Fig. 5 Comparing visible CCD camera inversions of D_α emissivity (bottom) with B2-Eirene simulations (top) for the three values of outer target f_e. All experimental data are plotted on the same, arbitrary, intensity scale. For the model distributions, the cases correspond to the vertical arrows in Fig. 2

Concerning the essential differences between the results of experiment and simulation, the problem lies with the low apparent densities in the TCV divertor. Although outer target detachment is readily observed experimentally, it can only be obtained theoretically without adjustment of recombination rates if the upstream density is fixed at values significantly higher than measured experimentally. This in turn yields target ion fluxes incompatible with observed values. The modelling strategy has therefore been to reduce P_{SOL} such that upstream densities stay low enough when detachment occurs and to increase the carbon chemical sputtering yield such that radiation balance is achieved at the relatively low divertor (and hence neutral) densities implied by the low ion fluxes seen experimentally. Whilst this approach leads naturally to the low divertor T_e (Fig. 3) required for recombination to occur, the effective (3-body and radiative) rate coefficient at these temperatures is strongly density dependent and is too low for recombination to play a role, at least if the rate coefficients are not artificially increased. An alternative mechanism for charged particle removal, the action of a cold plasma buffer just in front of the target [5], is unimportant in TCV as a consequence of the low densities and hence low neutral-neutral collision rate. Of course, by fixing input parameters in the way described here, one does not realistically simulate all experimental aspects (in particular P_{SOL} varies rather strongly with increasing density). However, given the CPU intensive nature of these simulations, this kind of systematic approach serves at least to highlight those areas where discrepancies are largest. In the case of TCV, it would appear that an alternative recombination pathway must be sought to explain the level of observed detachment. Such processes might involve molecular recombination pathways involving both deuterium [5] and/or hydrocarbons [8].

Acknowledgment: This work was partly supported by the Swiss National Science Foundation.

References:

[1] PITTS, R.A., et al., to be published in J. Nucl. Mater.
[2] REITER, D., et al., Plasma Phys. Contr. Fusion **33** (1991) 1579.
[3] LOARTE, A., et al., Nucl. Fusion **38** (1998) 331.
[4] KEILHACKER, M., et al., Phys. Scr. **T2/2** (1982) 443.
[5] KRASHENINNIKOV, S.I., et al., Phys. Plasmas **4** (1997) 1638.
[6] STANGEBY, P.C., Plasma Phys. Contr. Fusion, **37** (1995) 1459.
[7] HORACEK, J., PITTS, R.A., and LOARTE, A., in preparation.
[8] JANEV, R.K., KATO, T., WANG, J.G., submitted for publication in Phys. Plasmas.

Plasma Shape Effects on Sawtooth / Internal Kink Stability and Plasma Shaping Using EC Wave Current Profile Tailoring in TCV

A. Pochelon, F. Hofmann, H. Reimerdes, C. Angioni, R. Behn, R. Duquerroy, I. Furno, T.P. Goodman, P. Gomez, M.A. Henderson, An. Martynov, P. Nikkola, O. Sauter, A. Sushkov*

Centre de Recherches en Physique des Plasmas, Ecole Polytechnique Fédérale de Lausanne, Association EURATOM-Confédération Suisse, CH-1015 Lausanne EPFL, Switzerland
*RRC, Kurchatov, Russia
e-mail contact of main author: Antoine.Pochelon@epfl.ch

Abstract. This paper addresses the effect of plasma shaping (triangularity and elongation) on the sawtooth stability as well as the technique of current profile broadening using off-axis electron cyclotron heating (ECH) to enlarge the stable operational range towards higher elongations. The plasma shape strongly influences the sawtooth period and amplitude. This effect is emphasised by ECH, with the sawtooth period becoming shorter at low triangularity or at high elongation; for these plasma shapes, the pressure profile inside q=1 remains essentially flat. A comparison of the sawtooth response with marginal Mercier stability shows that the critical pressure gradient at q=1 is particularly low for plasma shapes where the increased sawtooth repetition frequency prevents the peaking of the pressure profiles. For theses shapes, the ideal internal kink is also found unstable from stability calculations. The stability of highly elongated plasmas depends largely on current profiles. The operational range at low current has been extended towards higher elongation using ECH heated discharges. Far off-axis second harmonic X-mode ECH power deposition proves to be an efficient tool for current profile tailoring allowing a significant elongation increase at constant quadrupole field.

1. Introduction

The TCV tokamak (R=0.88 m, a=0.25 m, $I_p \leq 1$ MA, B<1.54 T, $\kappa<2.8$, $-0.7<\delta<0.9$) is particularly suited for the study of shape related issues. It is presently equipped with a total of 3 MW ECRH/ECCD power at the second harmonic, 82.7 GHz, injected by 6 independent launchers, steerable during the discharge, which allows for highly localised power deposition schemes [1].

2. Dependence of sawtooth / Internal kink stability on plasma shape

2.1 Triangularity and elongation effects with central ECH

In the TCV tokamak the sawtooth period and the sawtooth amplitude are observed to depend strongly on the shape of the poloidal plasma cross-section. Systematic scans of plasma elongation and triangularity ($0<\delta<0.5$, $1.2<\kappa<2.1$) show small sawteeth with short periods at high elongation or at low and negative triangularity, and large sawteeth with long periods at low elongation or high triangularity. Additional central electron cyclotron heating power further amplifies the shape dependence of the sawtooth properties. The sawtooth period can either increase or decrease with additional heating power depending on the plasma shape. As an example, FIG. 1 shows the increase of the sawtooth period with power deposited inside the q=1 surface at high triangularity and the decrease at low triangularity. Similarly, the sawtooth period decreases for high elongations [2].

An analytic expansion of the Mercier criterion [3] suggests that low triangularity and high elongation lead to a lower ideal MHD central pressure limit, as shown in FIG. 2 for the shape parameters of the q=1 surface. These analytic results are confirmed by ideal MHD calculations using the KINX code [4], which show that the internal kink mode is unstable for the lowest triangularity and highest elongation cases of FIG. 2, and stable for the highest triangularity and lowest elongation cases. Therefore, for plasma shapes where additional heating and, consequently, increased central pressure gradients shorten the sawtooth period, the low central pressure gradient limit achieved is consistent with ideal MHD predictions of internal kink stability. This is expressed by a limitation of the poloidal beta on the q=1 surface (see e.g. [2]): $\beta_{p,1}=(\langle p\rangle_1 - p(\rho_1))/(B_p^2(\rho_1)/2\mu_0)$, where the numerator represents the volume averaged

incremental pressure above the pressure at q=1. In addition, the experimentally observed sawtooth behaviour is consistent with a sawtooth trigger model, which assumes the ideal or resistive internal kink to be responsible for the sawtooth crash [5]. The results of FIG. 1 exhibit two triangularity ranges: for $\delta \leq 0.2$, where the sawtooth period decreases with power in accordance with the destabilising effect of central pressure on internal kink stability; and for $\delta \geq 0.3$, for which the increased pressure gradients are stabilising through increased ω_e^* [5].

Ideal KINX code results also show the internal kink stability to be dependent on shape parameters [6]. The ideal internal kink is shown to be unstable at triangularities in the range $-0.14<\delta_1<0.11$ for elongations typically $\kappa_1>1.3$, this elongation limit decreasing slightly with $\beta_{p,1}$. At higher or lower δ_1, the mode becomes stable. The domain over which τ_{ST} was investigated in TCV is within this triangularity range. In the experiment, discharges with elongation $\kappa_1>1.3$ show indeed a shortening of τ_{ST} with P_{EC} (see FIG. 2).

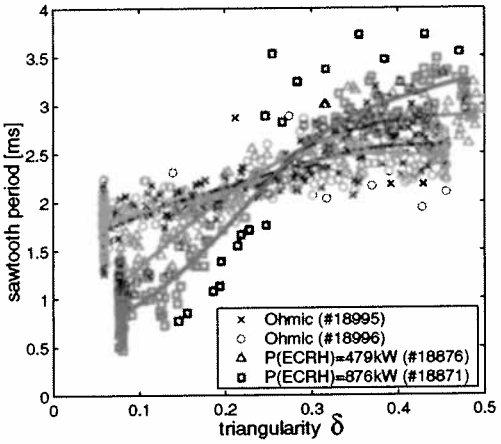

FIG. 1 Sawtooth period as a function of triangularity δ for an ohmic discharge with κ~1.5 and different ECRH powers injected inside q=1. The sawtooth period decreases for low triangularity, δ<0.2-0.3 and increases above. Electron density and sawtooth inversion radius were kept constant (ρ_{inv}~0.5, $q_{eng}=5abB/RI_p$~2).

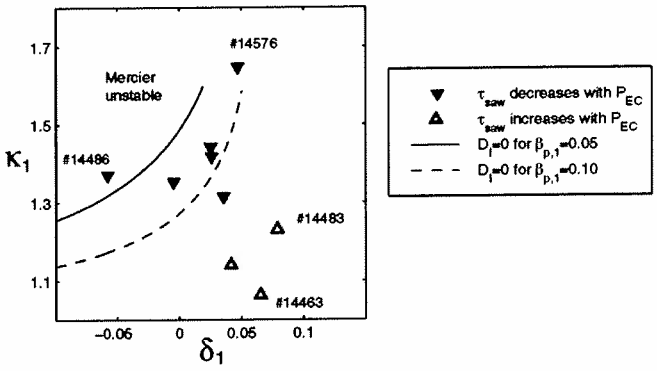

FIG. 2 The discharges of different shapes are shown as a function of triangularity and elongation of the q=1 surface. The plasma shapes are compared to the shapes corresponding to marginal stability according to the Mercier criterion [3] for two different values of $\beta_{p,1}$ and assuming constant shear $s_1=\rho_1(dq/d\rho_1)=0.1$ and inversion radius $\rho_{inv}=0.5$.

Direct measurements of the n=1 exponential growth rate γ from magnetic and/or soft X-ray signals have also been attempted, e.g. in JET [7] and TCV. In TCV, this γ increases with triangularity ($0<\delta<0.5$), and appears to be in contradiction with the Mercier stability and the sawtooth period data [2]. The measured γ scales with the amplitude of the crash pressure drop, which increases with the longer sawteeth at high triangularity. However, the experimental γ can only be measured in the late non-linear phase of the crash, and is not necessarily related to the linear γ, which probably remains below noise level.

2.2 Extreme elongation ohmic behaviour ($2.3<\kappa<2.8$)

Extremely elongated ($2.3<\kappa<2.8$) ohmic plasmas have been created in TCV at low q. In these discharges, the sawtooth period, τ_{ST}, decreases with elongation, FIG. 3, extending earlier results [2, 8] to even higher elongation. The sawtooth period is normalised to the density, which folds ramp-up and ramp-down values together. Therefore, the τ_{ST} values are not the result of transients. This normalisation is justified by the proportionality $\tau_{ST} \sim n_e$ found in several tokamaks [9, 10] and confirmed in TCV for different elongations (κ=1.6, 2.2), at similar measured inversion radii (ρ_{inv}~0.40-0.45) for densities ranging from 2 to 5 $10^{19} m^{-3}$.

When the elongation is increased, see FIG. 3, a first discontinuity is seen at κ~1.9, after which the sawtooth period and relative fluctuation amplitude continue to decrease up to an elongation κ~2.3-2.6, where the sawteeth abruptly disappear below resolution. This abrupt transition occurs at a very precise value of the internal inductance, l_i~0.69 (at low q, large ρ_1), see FIG. 4. The sawtooth inversion radius, ρ_{inv}, remains approximately constant. It does not vary significantly prior to the transition (typically ~ 0.49±0.03), and may vary somewhat more after the transition, where some small randomly re-occurring sawteeth allow its determination, even below l_i~0.69. The electron temperature profile remains practically unchanged through the transition. Therefore, with or without sawteeth, it is very flat in the centre and shows a sharp rollover in the ρ_{inv} region, suggesting that ρ_1 does not change during this transition.

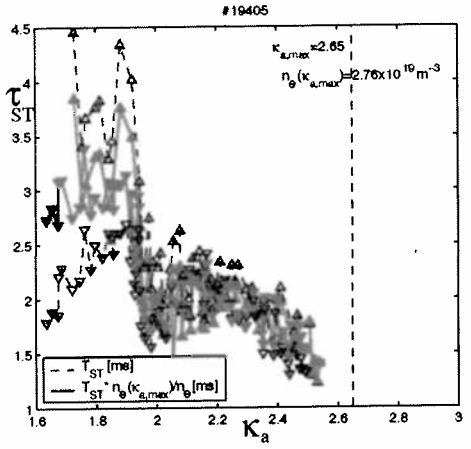

FIG. 3 Decrease of the sawtooth period τ_{ST} with elongation and sawtooth disappearance at κ~2.5. The normalisation to n_e (full triangles) cancels the ramp-up/-down hysteresis.

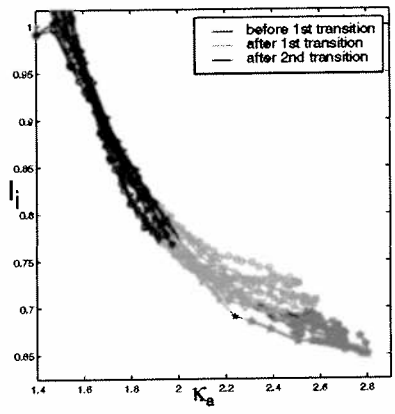

FIG. 4 Abrupt disappearance of sawteeth below an internal inductance of l_i=0.69 for different n_e and dI_p/dt.

Higher toroidal modes, n=2, 3, 4, measured with magnetic probes, are observed at high elongation. Thus, there are several indications supporting the existence of unstable modes at extreme elongation which flatten the core temperature profile even though the macroscopic sawteeth have disappeared.

2.3 Conclusion

In these experiments, the observed sawtooth period has been successfully used to link the experiment with the Mercier ideal stability criterion and with internal kink stability. The flexibility in plasma shape of TCV has therefore allowed: 1) the experimental determination of the effect of plasma shape and central pressure on sawtooth stability, 2) the demonstration of the contribution of the ideal internal kink mode in triggering the sawtooth crash at high elongation and at low triangularity [2].

3. Current profile modifications to increase plasma elongation

The stability of highly elongated plasmas depends largely on current profiles [11]. At high elongation, low current high q discharges are unstable with respect to axisymmetric modes. We present initial experiments using EC wave current profile broadening to create and stabilise high elongation, low current discharges, which would be ohmically unstable, thus reducing the strong correlation between κ and l_i in ohmic plasmas at fixed current (FIG. 4).

Among the different EC-schemes, the current profile can be broadened by off-axis ECH, on axis counter-ECCD or off-axis co-ECCD. PRETOR transport code simulations [12, 13] using the local RLW heat transfer coefficients [14] favour off-axis ECH. Let us consider the requirements for maximising the current density in the outer half of the profile. In general, simulations show that the current density j(ρ) is increased above ohmic at the deposition radius, ρ_{dep}, and in a layer of finite thickness outside of it. Hence, the optimal ρ_{dep} to increase j(ρ~0.7)

is typically ρ_{dep}~0.7. Moving ρ_{dep} too far in, typically ρ_{dep}<0.5, is seen to decrease j(ρ~0.7). The experimental task is then the determination of an optimum deposition location in the outer half of the profile, which maximises both elongation and plasma stability. Central counter-ECCD increases the current in a ring inside ρ~0.65 and decreases it further out, making it less attractive than off-axis ECH, which was also confirmed experimentally.

The standard EC set-up uses 2-4 gyrotrons, a maximum of 2MW shared between upper lateral and equatorial launchers, in off-axis ECH. The discharges are pre-programmed for a constant quadrupole field throughout the ohmic and EC heated phases. Using a high pre-programmed triangularity, similar to that used in ohmic discharges, led to 8% indentation in the mid-plane on the HFS in the EC phase, a wider gap on the LFS and very high central elongation $k_0 \sim k_{edge}$. By decreasing the triangularity, the indentation was removed and the elongation on axis reduced, which improves stability and spreads the power more uniformly onto the tiles. This allowed operation at high elongation and low current (κ=2.4, q=13, I_p=300kA, $\langle j \rangle / (q_\omega j_0) \sim 0.22$), which would not have been possible with peaked ohmic profiles. As a comparison, ohmic discharges at elongation κ=2.4 were typically obtained at current densities which were higher by a factor 2.5.

With an injection of 1.9MW using 4 static EC beams at ρ=0.65 initially, the initial ohmic elongation of 1.75 increases to 2.40 in 0.37s, while the deposition gradually moves to smaller radii, ρ=0.5. Meanwhile, the internal inductance l_i decreases from 1.25 to 0.83, which can be attributed to both the increased elongation and the flattened current profile. Growth rates of the vertical instability, as obtained from a rigid displacement model [15] are γ_R=996s^{-1} in the ohmic phase and γ_R=2688s^{-1} just before the disruption. The latter value corresponds to a very low stability margin and, consequently, we are close to the maximum elongation at I_p=300kA.

The discharge stability was improved by reducing the injected power to 1MW and moving the ECH deposition out during the elongation process. This allowed completely stable non-disruptive discharges at κ=2.4, FIG. 5, with γ_R=2238s^{-1} at the highest elongation, t=1.4s. The lower beam is moved out (FIG. 5b) during the discharge to keep the deposition location

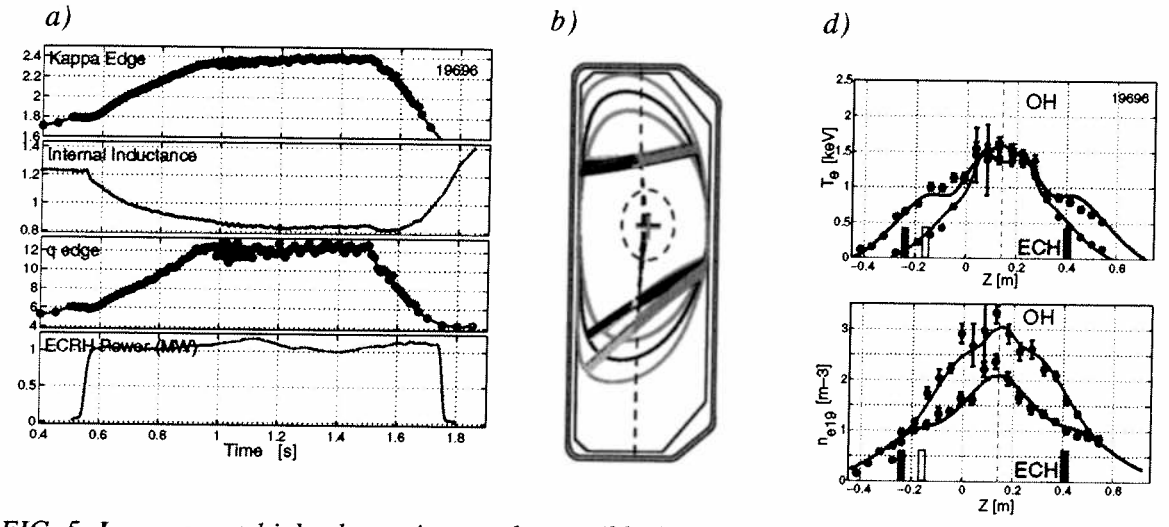

FIG. 5. Low current high elongation made possible by off-axis ECRH current profile broadening. a) Elongation grows from 1.8 to 2.4 with 1MW ECRH. b) Poloidal view with plasma shape and beams at three times (t=0.55, 0.75, 1.4s), cold resonance and q=1 surface at initial ohmic time. c) Deposition in the outer half of the profile, with lower launcher moving out during the shot. c) Thomson T_e and n_e profile in ohmic phase (blue) and at highest κ during ECRH (red, t=1.4s).

approximately constant at ρ_{dep}~0.7 (FIG. 5c), which allows a more economical use of the deposited power while elongating. The ECH power was shut off only after the pre-programmed elongation ramp-down, permitting a soft termination of the discharge. The electron temperature profile is broadened, with a distinct shoulder at the power deposition location, see FIG. 5d top. The density profile is strongly modified with a pump-out effect removing density from the deposition location, pushing it to the centre and to the edge. This explains strong density peaking on axis and a high gas injection rate to compensate for the outward flux. A power balance analysis shows that the heat flux and the electron conductivity χ_e is strongly reduced to values below the ohmic level inside the deposition radius and increased outside.

Soon after the heating starts, the central q_0 moves above unity and sawteeth disappear. Due to the ρ_{dep} sweep during the discharge and the induced q-profile change, the power deposition location crosses integer-q surfaces. However no deleterious MHD was noticed in these high q discharges. The final elongation depends only weakly on power. It also depends weakly on the location of the power deposition as long as the deposition occurs in the outer half of the profile.

However, there is an outer limit for the initial deposition radius beyond which the first-pass absorption is too low to embark on an elongation process. A successful elongation run was still obtained with 2MW and starting the deposition as far out as ρ~0.8, with a first-pass absorption below 50% (n_{e19}~0.7, T_e~0.3keV at the absorption layer). Lowering the power to 1MW required a more central initial deposition location.

3.1. Conclusion

Far off-axis second harmonic X-mode ECH power deposition proves to be an efficient tool for current profile tailoring allowing a significant elongation increase at fixed quadrupole field. The operation at low current and high elongation has been substantially extended with off-axis ECH current profile broadening, making low current operation possible at current densities 2.5 times lower than in similar ohmic plasmas. From the present experience, stable high elongation discharges at κ>2.4 will require higher currents, since the axisymmetric growth rate is close to the limit. Furthermore, the exploitation of the high β potential of elongated discharges would require a normalised current around I_N=I/aB~2.0MA/mT, a factor of 2 above the 0.84MA/mT achieved here. This opens a new area for confinement and stability limit studies at high elongation, e.g. combining X2 current profile broadening and X3 central heating [16].

Acknowledgement: This work was partly supported by the Swiss National Science Foundation.

References:

[1] GOODMAN T.P. et al., 19th Symp. on Fusion Technology, Lisbon, Portugal, 1996.
[2] REIMERDES H., POCHELON A., SAUTER O., GOODMAN T.P., HENDERSON M.A., MARTYNOV An.A., Plasma Phys. Contr. Fusion **42** (2000) 629.
[3] LÜTJENS H., BONDESON A. and VLAD G., Nucl. Fusion **32** (1992) 1625.
[4] DEGTYAREV L., MARTYNOV A., MEDVEDEV S., TROYON F., VILLARD L., GRUBER R., Comput. Phys. Commun. 103 (1997) 10.
[5] PORCELLI F., BOUCHER D. and ROSENBLUTH M.N., Plasma Phys. Contr. Fus. **38** (1996) 2163.
[6] MARTYNOV An. and SAUTER O., Proc. of Theory of Fusion Plasmas, Varenna 2000, (Editrice Compositori, Bologna, 2000), (to be published).
[7] DUPERREX P.A., POCHELON A. et al., Nucl. Fusion **32** (1992) 1161.
[8] POCHELON A., GOODMAN T.P., HENDERSON M.A. et al., Nucl. Fus. **39**, No.11Y (1999) 1807.
[9] TFR-Group, Proc. 6th Int. Conf. on Plasma Phys. and Contr. Nucl. Fus. Research, Berchtesgaden Vol. I (1976) 279.
[10] SIMM W., Thesis, Lausanne Laboratory Report LRP 334/87 (1987).
[11] HOFMANN F. et al., Phys. Rev. Lett. **81**, 2918 (1998).
[12] ANGIONI C. et al., ibid., (to be published).
[13] BOUCHER D. and REBUT P.H., in Proc. IAEA Tech. Com. on Advances in Simulation and Model. of Thermonuclear Plasmas, 1992, Montreal (1993) 142.
[14] REBUT P.H., LALLIA P.P. and WATKINS M.L., Proc. 12th Int. Conf. Plasma Physics and Controlled Nuclear Fusion Research, Nice 1988, IAEA Vienna 1989, Vol. 2, 191.
[15] HOFMANN F. et al. Nuclear Fusion **38** (1998) 1767.
[16] ALBERTI. S. et al., Proc. 18th IAEA Fusion Energy Conf. paper PD/2.

Advances in Global Linear Gyrokinetic Simulations

L. Villard 1), K. Appert 1), W.A. Cooper 1), G.L. Falchetto 1), G. Jost 1), M. Maccio 1), T.M. Tran 2), J. Vaclavik 3)

1) CRPP, Association Euratom - Confédération Suisse, Lausanne, Switzerland
2) Service Informatique Central, EPFL, Lausanne, Switzerland
3) La Conversion, Switzerland

e-mail contact of main author: laurent.villard@epfl.ch

Abstract. Substantial advances have been made in the global calculation of microinstabilities. First, we present results of the world's first global linear gyrokinetic code in fully 3D configurations. We show that the unstable Ion Temperature Gradient (ITG) modes in quasi-axisymmetric and quasi-helical configurations exhibit 3D features, while the global stability properties seem rather insensitive to the three-dimensionality of the configuration. Second, the inclusion of equilibrium radial electric fields in both finite element particle-in-cell (PIC) and spectral global codes yield the remarkable result that the value of the $E \times B$ flow can be as effective as its shear in stabilizing toroidal ITG modes. Third, electron dynamics and finite beta effects are addressed by including electromagnetic perturbations with a two-potential formulation.

1. Introduction

The present understanding of anomalous transport in magnetically confined plamas is based on various underlying microinstabilities driven by equilibrium gradients. While nonlinear simulations are necessary for the determination of the heat flux generated by the microturbulence, linear simulations are useful in identifying the physical and geometrical parameters influencing the stability. In this paper a global approach is adopted, in which the relevant gyrokinetic equations are solved in the full plasma domain in the appropriate geometry. Throughout this paper the usual gyrokinetic ordering is used: $O(k_\perp \rho) \approx 1$, $\omega/\Omega \approx k_\parallel/k_\perp \approx e\phi/T_e \approx \rho/L_n \approx \rho/L_T \approx O(\epsilon)$ and $\rho/L_B \approx O(\epsilon_B)$, where ρ is the ion Larmor radius, Ω is the ion cyclotron frequency, ϕ is the perturbed electrostatic potential, L_n, L_T and L_B are the equilibrium scale lengths of density, temperature and magnetic field, respectively. The gyrokinetic equations are valid to the order $O(\epsilon^2)$, $O(\epsilon\epsilon_B)$ and $O(\epsilon_B)$. Two different methods are used: one is a time-evolution, Particle In Cell (PIC) - finite element method [1], the other is a spectral approach [2].

2. ITG modes in stellarator configurations

The next generation of stellarators will be characterized by much smaller neo-classical transport than previously and by particle confinement close to that of tokamaks. The question naturally arises as to whether anomalous transport in these devices will show up. As a first step in this direction we have developed a global gyrokinetic code, EUTERPE, aimed at the investigation of ITG modes in general 3D geometry. The essential ingredients used in the model and its numerical implementation are summarized here. More details can be found in [3]. We consider general 3D MHD equilibrium configurations with nested flux surfaces provided by the VMEC code [4]. The VMEC coordinates are mapped into straight-field-line magnetic coordinates. We use PIC with 3D quadratic

splines finite elements on the linearized δf method [5] in which only the perturbed part of the distribution function is discretized. We take advantage of the interchange nature of the ITG mode ($k_{||} \approx 0$) by extracting the fast phase variation across field lines using the method presented in [1], thus making simulations with large mode numbers possible with virtually no increase in the required computing power. To reduce numerical noise a Fourier filter is applied that keeps m and n components with small $k_{||}$ and those resulting from the coupling induced by the 3D magnetic field configuration. The resulting EUTERPE code has been successfully validated against the 2D GYGLES code [1] in its toroidal axisymmetric and helically symmetric versions [6].

We have investigated the global linear stability of ITG modes in the QAS3 configuration which is under consideration at PPPL [7]. QAS3 is characterized by three field periods, a dominant tokamak-like $B_{m=1,n=0}$ component, but also a strong "mirror-field" $B_{m=0,n=1}$ component. Its shear is negative. Fig.1 shows the ITG mode $m_0 = -24$, $n_0 = 8$ as computed by EUTERPE. (In a 3D configuration the eigenmodes of the system have several m and n, so m_0, n_0 refer here to the dominant mode numbers.) The ITG mode is ballooning all along the torus on the low field side, with only a slight variation in amplitude along the toroidal direction. Thus this mode is almost characterized by a single toroidal mode number as in a tokamak. The similarity of QAS3 with a tokamak is further exemplified by comparing the frequencies and growth rates of QAS3 and an "equivalent tokamak" having only the axisymmetric components of the plasma surface $R_{m,n=0}, Z_{m,n=0}$ but otherwise the same parameters (Fig.2). We have checked that this similarity of ITG behaviour is not a coincidence by considering a sequence of equilibria that vary continuously from the pure axisymmetric case to the QAS3 case. In contrast to the balloning model which predicts a strong influence of the local magnetic shear on drift wave stability [8] we have found virtually no influence, even though the local shear in QAS3 is strongly modulated: the ITG mode amplitude is only slightly modulated and the growth rate is not affected. We conclude that the stability properties of the global toroidal ITG mode in QAS3 are indeed virtually identical to those obtained in a tokamak.

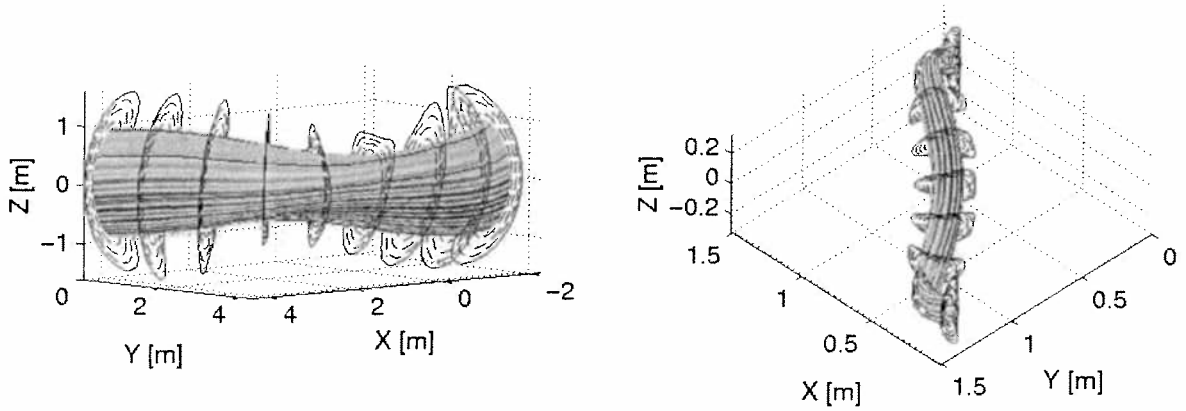

Figure 1: *ITG mode in QAS3 (left) and in HSX (right) as computed with the EUTERPE global gyrokinetic code.*

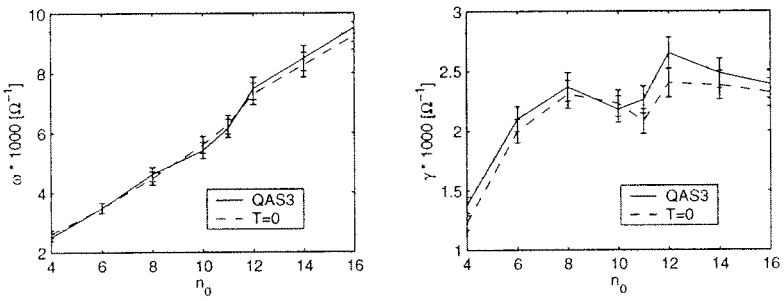

Figure 2: *Frequencies (left) and growth rates (right) of ITG modes vs dominant toroidal mode number in QAS3 (continuous line) and an equivalent tokamak (broken line).*

The HSX device is a helical axis stellarator with 4 field periods, a dominant helical-like $B_{m=1,n=1}$ component and a rather flat safety factor profile, $q_{edge}/q_{axis} \approx 0.95$. It has recently started operation at the University of Wisconsin. We show in Fig.1 the mode $m_0 = -9, n_0 = 8$ as computed with the EUTERPE code. The ITG mode amplitude shows, in addition to a tendency to alignment with the quasi-helical symmetry, a toroidal modulation of about 50%. This amplitude modulation has been found to correlate with the variation of the Jacobian: $|\tilde{\phi}|$ reaches its maximum where the Jacobian is minimum. Because of its helical magnetic axis, the structure of the Jacobian results from the variation of the major radius along the toroidal direction. In HSX it varies from $R = 1.45$m at the beginning of a field period to $R = 1.05$m in the middle of a field period. The curvature drifts are then stronger in the middle of a field period and this pushes the ITG mode amplitude higher there. In order to quantify the influence of plasma shape, we consider a sequence of equilibria varying from the quasi-helical HSX configuration to a helically symmetric configuration, increasing the number of field periods in proportion to the aspect ratio. The modulation of the ITG amplitude decreases until perfect alignment with the helical symmetry is reached. However, we have found that the growth rate varies by less than 10%. This indicates that global ITG mode stability properties in HSX are essentially similar to those of a helically symmetric configuration.

3. Effects of $E \times B$ flows

In tokamaks, $E \times B$ sheared flows have been observed to be related to the appearance of improved confinement regimes, hence reduced anomalous transport. Theories of flow shear fluctuation supression [9, 10] show that if the $E \times B$ flow is sheared, then it should decorrelate the turbulence and therefore stabilize it when the shearing rate $\omega_{E\times B}$ approximately equals the growth rate γ. In [9] $\omega_{E\times B}$ is proportional to $\partial/\partial\rho(u/\rho)$, where $u = E \times B/B^2$ and ρ is the minor radius, whereas in [10] it is proportional to $d^2/d\psi^2\Phi_0(\psi)$, which reduces in the circular, large aspect ratio limit to $\partial/\partial\rho(qu/\rho)$. Here, an equilibrium radial electric field is assumed and its effect on ITG modes global linear stability is studied. Both PIC-finite element and spectral methods have been applied. We consider a tokamak with circular cross-section, and a T_i profile peaking at mid-radius with R/L_{Ti}=7.4. The $E \times B$ profile is specified in three different ways: (1) a constant profile of u/ρ; (2) a linear profile of u/ρ; and (3) a constant profile of $d\Phi_0/d\psi$, where $\mathbf{E} = -\nabla\Phi_0(\psi)$ and ψ is the poloidal flux. Our results in Fig.3 show that indeed a sheared $E \times B$ flow is

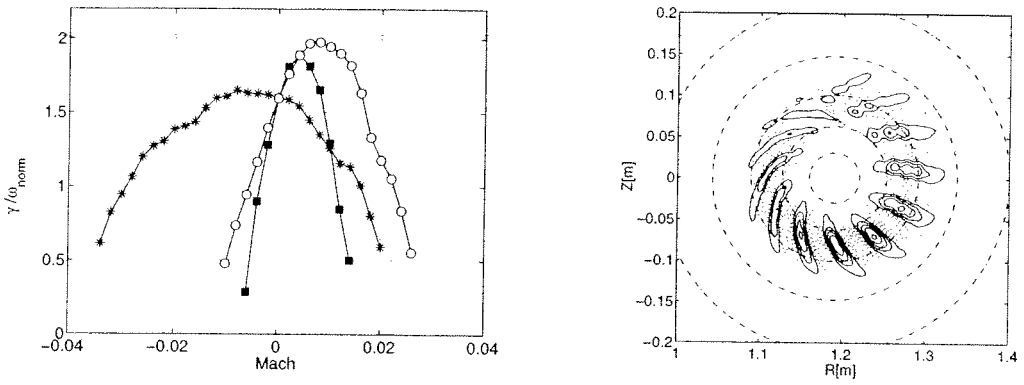

Figure 3: *Left: growth rates of the most unstable toroidal ITG mode vs Mach number for a sheared profile of* $u = E \times B/B^2$ *(open symbols), for a shearless profile of* u/ρ *(filled symbols) and for a shearless profile of* $d\Phi_0/d\psi$ *(stars). Right: perturbed* ϕ *for a shearless profile of* $d\Phi_0/d\psi$ *with Mach=-0.034.*

stabilizing the toroidal ITG mode (open symbols). But the shearless cases are interesting: the shearless u/ρ (filled symbols) provides even stronger stabilisation than the sheared case, while the shearless $d\Phi_0/d\psi$ is more weakly stabilized. We conclude that, in addition to the commonly admitted shearing rate criteria, there is another stabilizing mechanism: the value of flow is as important as its shear. From an analysis of the eigenmode structure we interpret it as follows: the toroidal ITG mode balloons in the unfavourable grad B drift region; as the value of $E \times B$ flow is increased it pushes the maximum mode amplitude poloidally away from the unfavourable grad B drift region, thereby decreasing the instability drive. A heuristic criterion can be derived: there is stabilization when the poloidal $E \times B$ rotation frequency becomes comparable to the linear growth rate without rotation. Note that the profile of constant u/ρ is sheared in the sense of Ref.[10], so the two effects of shearing and rotation value add up for this particular profile.

Taking parabolic profiles of u/ρ with zero first derivative at the maximum gradient position, we have shown that the effect of the so-called "flow curvature" is negligible [11]. Also, we have analyzed an ASDEX-Upgrade case with improved confinement. Our results show that ITG modes are stabilized for values of $E \times B$ flow in reasonable agreement with the experiment [11]. We have also shown that large T_i/T_e is stabilizing, whereas the inclusion of trapped electron dynamics is destabilizing.

4. Electromagnetic effects on microinstabilities

Electromagnetic perturbations and electron dynamics can strongly affect the behaviour of microinstabilities: finite plasma β can stabilize ITG modes. The model used describes the perturbation with a two-potential approximation $(A_{\|}, \phi)$. The same spectral approach as in [2] is adopted. We show in Fig.4 the growth rates as a function of β. Neglecting trapped electron effects, the ITG mode is quickly stabilized at $\beta \approx 4\%$. Including trapped electrons, we show different cases for different values of magnetic shear. Trapped electrons are overall destabilizing, but the most remarkable feature is the effect of shear coupled to β. For small β values, reversing the shear is stabilizing, whereas for $\beta > 3\%$, zero or negative

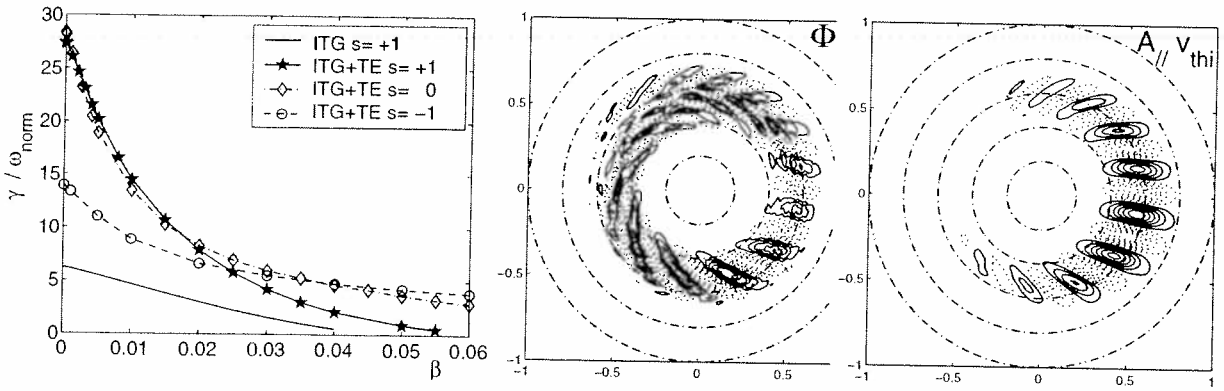

Figure 4: *Left: growth rates of most unstable ITG modes vs β, for different values of magnetic shear (plain line: without trapped electrons, other curves with). Perturbed ϕ (middle) and $A_{||}$ (right), for the case β=4%, shear=+1.*

shear cases are more unstable and complete stabilization is prevented at least until β=6%. For zero or positive shear, the electromagnetic component of the perturbation, measured as $v_{thi} < |A_{||}| > / < |\phi| >$, where <> denotes the spatial average, is increasing from about zero at β=0 to about 0.4 at β=4%. Fig. 4 shows a ballooning-like mode structure for $A_{||}$ which varies very little with β, whereas ϕ is more affected. For negative shear, ITG modes are more slab-like and the electromagnetic component does not exceed 3×10^{-3}.

Trapped electron modes, on the other hand, are insensitive to finite β effects, and reversing the shear is always stabilizing. The insensitivity to β is confirmed by the fact that these modes are almost purely electrostatic: $v_{thi} < |A_{||}| > / < |\phi| > < 10^{-3}$ for all β values.

Acknowledgements. This work was partly supported by the Swiss National Science Foundation. Some computations were performed using the Cray T3E of the Max Planck Gesellschaft in Garching. We thank A. Peeters and S. Günter for fruitful discussions.

References

[1] FIVAZ, M., *et al.*, Comput. Phys. Commun. **111** (1998) 27.
[2] BRUNNER, S., *et al.*, Phys. Plasmas **5** (1998) 3929.
[3] JOST, G., Simulation of Drift Waves in 3D Magnetic Configurations Using Particles, PhD Thesis no. 2174, EPFL, Switzerland.
[4] HIRSHMAN, S.P., LEE D.K., Comp. Phys. Commun. **39** (1986) 161.
[5] DIMITS, A.M., LEE, W.W., J. Comput. Phys. **107** (1993) 309.
[6] VILLARD L., *et al.*, in "Theory of Fusion Plasmas", Int. Workshop, Varenna, 1998, p.511.
[7] MONTICELLO, D.A., *et al.*, Proc. 25th EPS Conf. on Controlled Fusion and Plasma Physics, Prague, 1998, p.185.
[8] WALTZ R.E., BOOZER, A.H., Phys. Fluids B **5** (1993) 2201.
[9] BIGLARI, *et al.*, Phys. Fluids B **2** (1990) 1.
[10] HAHM, T.S., BURELL, K.H., Phys. Plasmas **2** (1995) 1648.
[11] MACCIO M., *et al.*, submitted to Phys. Plasmas.

Drift- / Kinetic Alfvén Eigenmodes in High Performance Tokamak Plasmas

A. Jaun[1], A. Fasoli[2], D. Testa[2], J. Vaclavik[3], L. Villard[3]

1) Alfvén Laboratory, Euratom-NFR Association, KTH, 100 44 Stockholm, Sweden
2) Plasma Science Fusion Centre, MIT, Cambridge MA 02139, USA
3) CRPP-EPFL, 1015 Lausanne, Switzerland

E-mail: jaun@fusion.kth.se

Abstract. The stability of fast-particle driven Alfvén eigenmodes is modeled in high performance tokamaks, successively for a conventional shear, an optimized shear and a tight aspect ratio plasma. A large bulk pressure yields global kinetic Alfvén eigenmodes that are stabilized by mode conversion in the presence of a divertor. This suggests how conventional reactor scenarii could withstand significant pressure gradients from the fusion products. A large safety factor in the core $q_0 > 2.5$ of deeply shear reversed configurations and a relatively large bulk ion Larmor radius in a low magnetic field can trigger global drift-kinetic Alfvén eigenmodes that are unstable in high performance JET, NSTX and ITER plasmas.

1. Introduction

Because of the large birth velocity of the fusion produced $\alpha-$particles exceeding the Alfvén speed, Alfvén eigenmodes (AEs) can potentially be driven unstable by the pressure gradient and affect the global confinement in a reactor. The regimes where this may occur can not be explored with dimensionless experimental scalings using the tokamaks currently in operation; numerical models are therefore needed to make stability predictions. To be credible, these models have to be validated against existing experimental measurements [1, 2].

The global nature and the frequency of AEs can be understood from fluid MHD models describing shear-Alfvén wavefields "trapped in a toroidal resonator"; global modes result because of the interplay between the plasma current, the plasma shape and pressure. To determine the stability of AEs, it is necessary to account for the coupling to the kinetic Alfvén wave. This stimulated the development of models such as *continuum damping*, *complex resistivity* and *radiative damping* where this coupling is calculated in an ad-hoc manner directly from fluid MHD modes. The difficulties in finding agreement between the models, more theoretical arguments [3] and the comparisons with experimental measurements [4, 5] motivate the use of a self-consistent gyro-kinetic description for the bulk plasma. Such a model is required to calculate the power transfer between global fluid and kinetic wavefields [6] and correctly predict global damping rates. Consequently, the stability of AEs depends on a variety of *mode conversion* mechanisms that appear where the phase velocities of the shear- and the kinetic-Alfvén wave coincide.

From the ratio between the ions drift- and the TAE frequency $\omega_*/\omega_{TAE} \simeq 2nq^2(\rho/a)^2(R\omega_{pi}/c)$ it appears clearly that a large safety factor $q_0 > 2.5$, a low magnetic field and large normalized Larmor radius ρ/a characteristic of high performance regimes, significantly complicate the stability calculations by introducing new mechanisms for mode conversion to the electro-magnetic drift waves. Global drift-kinetic AEs (DKAEs) [7] are formed that provide plausible explanations for the large fast particle losses observed in low magnetic field DIII-D plasmas [2, 8] and will here be further examined using the PENN code with an approximative $k_{||} = 1/(2qR)$ to model the resonant wave-particle interaction.

2. Comparisons with measurements from JET

Having tested in a predictive manner how the damping of low toroidal mode number $n = 1$ AEs rises with the edge magnetic shear ($|\gamma/\omega| \simeq 0.02-0.08$) [4] and decreases with the isotope mass ($|\gamma/\omega| \simeq 0.02 - 0.01$) [5], the understanding of the mode-conversion in JET made it possible to identify conventional plasma configurations where all the low and high n fast particle driven AEs of global nature are stable.

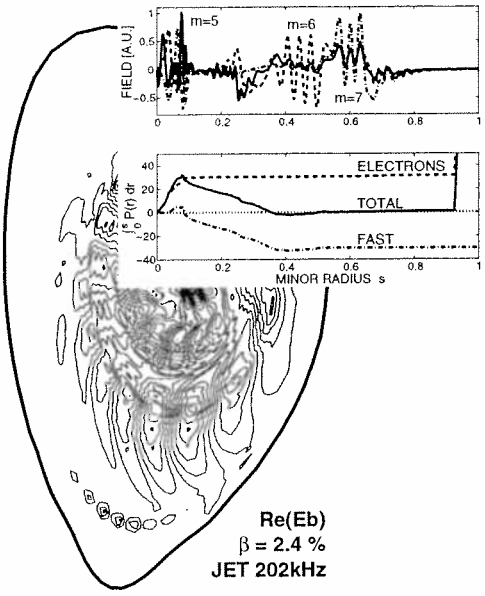

Figure. 1: A global n=6 KAE is stabilized by mode conversion near the X-point for a bulk $\beta > 2.5\%$ in the JET shot 40308.

Recent studies involving ICRH-driven instabilities with intermediate mode numbers (n=5-12), show that also radially localized modes become kinetic and global when the bulk plasma β rises, and, in a manner similar to low n modes, are stabilized by the strong shear in the divertor region and the weak shear in the plasma core [10]. Figure 1 illustrates this mechanism with a hot-ion H-mode discharge where an n=6 kinetic AE (KAE) instability in the plasma core ($s \simeq$ 0.2-0.4) extends radially as the bulk pressure rises above $\beta \simeq 1\%$ and mode-conversion is induced in a succession of toroidicity gaps (n_{e0}=3.5×10^{19} m^{-3}, T_{e0}=11.3 keV, T_{D0}=24.9 keV, q_0=0.84, q_{95}=3.5, l_i=0.94, β=2.4%, β_p=0.78, P_{NBI}(140 keV)=10 MW, P_{NBI}(80 keV)=8 MW, P_{ICRH}=4.5 MW). The mode is stabilized when the global wavefield reaches the divertor region and the kinetic Alfvén wave (visible at the bottom of Fig.1) gets heavily Landau damped by the electrons, in good agreement with the stability threshold observed experimentally.

A new class of instabilities is observed in optimized shear discharges, where a non-monotonic safety factor profile $q(s)$ is created by applying lower hybrid power in the pre-heating phase. This results in two internal transport barriers that sustain relatively large pressure gradients: the outer barrier is located in the neighborhood of the q=2 surface and the inner one is associated with a negative magnetic shear [9]. A typical example is given in Fig.2 for the JET discharge 51594, where MSE measurements show that a shear reversal is achieved at the beginning of the main heating phase (t=44.25s, q_0=3.1, q_{min}=2.1 at s=0.4 and q_{95}=5.7) and then slowly evolves due to the current diffusion (t=47.16s, q_0=2, q_{min}=1.5 at s=0.25 and q_{95}=5.4). The inner barrier is produced at t=45.2s around s=0.2 and the outer at t=45.9s around s=0.6. The spectrum of the magnetic fluctuations in Fig.2 shows that global instabilities with low to intermediate n=1-7 appear in the frequency range 70-170kHz. These modes are excited at relatively low ICRF power ($P_{ICRF} > 1$MW) and satisfy the local scaling $0.01 < \omega_{*D}/(n\omega_{TAE}) < 0.1$ characterisitc of DKAE modes. The frequency does not reproduce the usual AEs scaling and increases in time until the mode saturates in the TAE frequency range. The energetic character [11, 12] of the modes may also play a role. A comparison with a global gyrokinetic model accounting for both the drifts- and the energetic character is necessary to properly identify these modes.

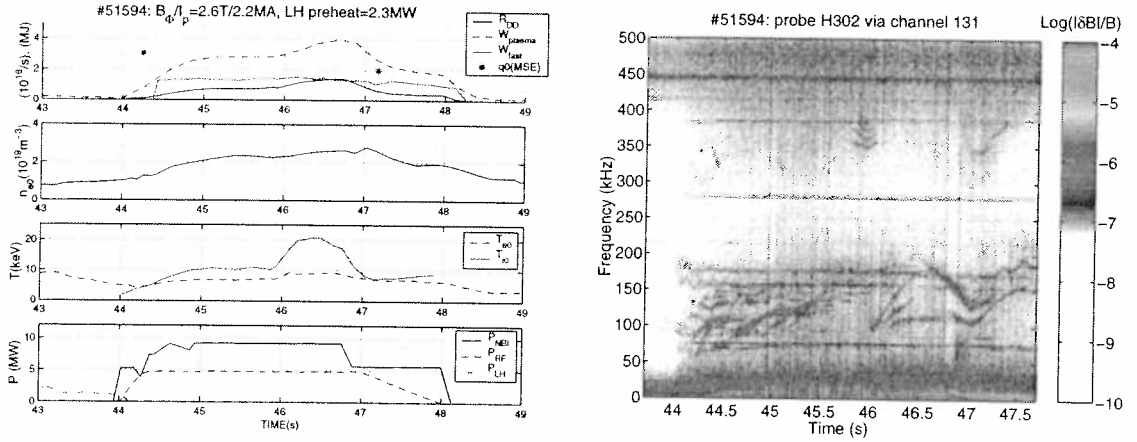

Figure 2: Instabilities are observed in the shear-optimized JET discharge 51594 using passive measurements of magnetic fluctuations.

3. Drift-kinetic Alfvén instabilities predicted in NSTX

Low aspect ratio plasmas differ in several manners from conventional ones and it is useful to address what could be the limits of applicability of the PENN model to such configurations. The most obvious limit is the strongly shaped toroidal geometry (in this NSTX model equilibrium, a tight aspect ratio R/a=1.3, elongation b/a=1.9, q_0=0.85, q_{95}=4), which yields strongly toroidal modes that are particularly well represented with a 2D finite elements discretization in configuration space. The large magnetic compressibility $\vec{B}_{||} = \nabla \times \vec{A}_{\perp}$ associated with the bulk pressure (β=23%, β_p=0.37) is taken into account using four potentials $(\vec{A}, \Phi)$ instead of the two components $(A_{||}, \Phi)$ that are often sufficient to model AEs in conventional tokamaks. The large bulk ion Larmor radius ($\rho_D/a \simeq 0.02$) and the large drift frequency $\omega_{*D}/\omega_{TAE} > 1$ resulting from rather energetic thermal particles in a low magnetic field (T_e=2.7 keV, T_i= 1 keV, B_0=0.3 T) are likely to cause strong effects from the finite Larmor radius and the equilibrium inhomogeneities; both are taken into account in the PENN code, which assumes here an approximative functional dependence $k_{||} = 1/(2qR)$ for the resonant wave-particle interaction. This provides a good qualitative description of the mode conversion between the fluid, kinetic Alfvén and drift wavefields, but may not always be sufficient for a quantitative evaluation of the drift-wave damping. The stability predictions below will need to be verified with a more complete model for macro-instabilities [3]. Because of the tight aspect ratio, a significant proportion of the particles are trapped and do not provide resonant interactions; it was suggested that collisional damping of trapped electrons become important instead. The power transfer to passing drift-kinetic electrons P_{DKe} [13] has therefore been supplemented with the collisional damping of trapped electrons

$$P_e = (1-\alpha_t)P_{DKe} + \alpha_t P_{col} \quad \text{with} \quad \alpha_t = \sqrt{\frac{B}{B_{max}}} \tag{1}$$

$$P_{col} = -\frac{(q\omega)^2}{2}\int dV \left(\frac{\nu}{\omega^2+\nu^2}\right)\frac{n_e}{T_e}|\Phi|^2 \tag{2}$$

where $\nu = (\nu_{ee}+\nu_{ei})R/\rho$ is an effective collision frequency and Φ is the electrostatic potential.

The power transfer with fast- and bulk ions is evaluated with the non-local expressions from Ref.[14] that are valid to all orders in the Larmor radius.

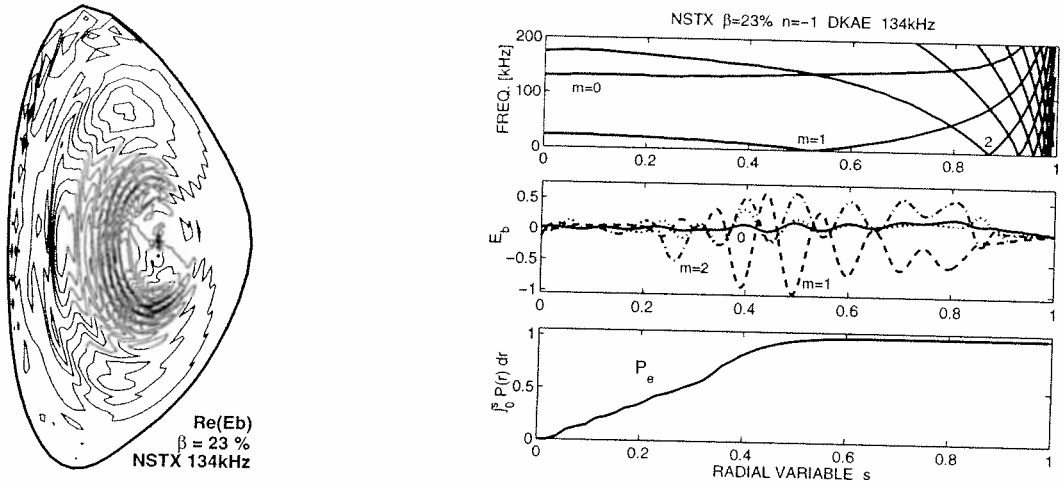

Figure 3: In NSTX, a global $n = 1$ DKAE at 134 kHz with a very weak damping $|\gamma/\omega| = 0.003$ is expected to becomes unstable already for moderate beam pressure gradients.

Weakly damped DKAEs susceptible to become unstable with a moderate drive from fast or even thermal ions are found both in the TAE and EAE frequency range. Figure 3 illustrates how a global n=-1 mode is formed at 134 kHz by elliptical coupling of the m=0,2 shear-Alfvén wavefield components. Mode conversion occurs to a kinetic-Alfvén wave, which propagates across the magnetic field and is responsible for the short radial oscillations that are visible on $E_b(s)$. Because of the large ratio ω_{*D}/ω_{TAE}, the largest component is an m=1 drift-wave induced by mode conversion in the neighborhood of the q=1 rational surface where $k_{\|} = R^{-1}(n + m/q) \approx 0$. The large compressibility $B_{\|} \simeq B_{\perp}$ results from the high plasma β. Power transfers from the particle to the wavefield integrated from the center $\int_0^s (P_e + P_D)dr$ show that resonant interactions with passing electrons provide for most of the small global damping $|\gamma/\omega| = 0.003$ from the plasma core $s < 0.5$. Towards the edge, most particles are trapped and neither the Landau damping nor the collisional damping significantly contribute to damp the short wavelengths oscillations that are mode converted in the high magnetic shear divertor region (clearly visible on the high field side of the torus).

Non-local calculations of the energetic particles drive have been performed assuming a relatively peaked density in the core and indicate that DKAEs become unstable already for moderate beam pressures $\beta_b > 2\%$. Large magnetic fluctuations created by the helicity injection could also excite weakly damped (but stable) DKAEs that could play a role in the global drift-Alfvén turbulence.

4. Implications for ITER and outstanding issues

Studies using (EDA, FEAT) model equilibria predict that conventional scenarii with monotonic or nearly flat safety factor profiles exist where all the AEs with low to intermediate mode numbers are stable [14]. Shear reversal in a reactor with a large safety factor on axis $q_0 > 2.5$, however, again brings the TAE frequency down into the drift frequency range and the PENN predictions indicates that global DKAE instabilities could appear above an intolerably small $\alpha-$particle pressure gradient [10]. More work with an improved modeling and comparisons with experimental data are necessary to establish an understanding of the linear mode conversion involving electro-magnetic drift waves and hopefully again identify high performance regimes where global DKAEs are stable. At present, the knowledge of the non-linear evolution and the associated transport stems almost exclusively from experiments and is not sufficient to draw firm conclusions for a reactor.

Acknowledgments

The Authors would like to acknowledge the support of the JET Team and thank D. Darrow, O. Sauter, Y. Gribov and D. Campbell for providing the equilibria. This work was supported in part by the Swedish and the Swiss National Science Foundations, the DoE Contract DE-FG02-99ER5-456 and the super-computer center in Linköping.

References

[1] A. Fasoli *et al.*, Phys. Plasmas 5 (2000) 1816

[2] W.W. Heidbrink *et al.*, Phys. Rev. Lett. 71 (1993) 885

[3] A. Jaun, J. Vaclavik, *Theory of Fusion Plasmas* (Proc. Int. Workshop, Varenna, 2000) Editrice Compositori, Bologna (2000)

[4] A. Jaun, A. Fasoli, W. W. Heidbrink, Phys. Plasmas 5 (1998) 2952

[5] A. Fasoli, A. Jaun, D. Testa, Phys. Lett. A 265 (2000) 288

[6] A. Jaun *et al.*, Phys. Plasmas 5 (1998) 3801

[7] A. Jaun, J. Vaclavik, L. Villard, Phys. Plasmas 4 (1997) 1110

[8] H.H. Duong *et al.*, Nucl. Fusion 33 (1993) 749

[9] C. Challis *et al.*, "Effect of q-profile Modifications by LHCD on Internal Transport Barriers in JET", Plasma Phys. Contr. Fusion (2000) submitted

[10] A. Jaun, A. Fasoli, J. Vaclavik, L. Villard, Nucl. Fusion 40 (2000) 1343

[11] L. Chen, *Theory of Fusion Plasmas* (Proc. Int. Workshop, Varenna, 1988) Editrice Compositori, Bologna (1988) 327

[12] F. Zonca, L. Chen, R.A. Santoro, J.Q. Dong, Plasma Phys. Control. Fusion 40 (1998) 2009

[13] L. Villard, S. Brunner, J. Vaclavik, Nucl. Fusion 35 (1995) 1173

[14] A. Jaun, A. Fasoli, J. Vaclavik, L. Villard, Nucl. Fusion 11Y (1999) 2095

Particle Transport with High Power Central ECH and ECCD in TCV

H. Weisen, I. Furno, T. Goodman and the TCV Team

Centre de Recherches en Physique des Plasmas
Association EURATOM-Confédération Suisse
École Polytechnique Fédérale de Lausanne
CH-1015 Lausanne, Switzerland

E-mail address of main author: Henri.Weisen@epfl.ch

Abstract. A coupled heat and particle transport phenomenon, leading to particle depletion from the plasma core is observed in a variety of plasma conditions with centrally deposited ECH and ECCD in TCV. This phenomenon, which causes inverted sawteeth of the central density in sawtoothing discharges and leads to stationary hollow profiles in the absence of sawteeth, has been linked to the presence of $m/n = 1/1$ MHD modes. In particular this phenomenon, known as "density pumpout" can be suppressed by stabilizing the mode by means of operation at high triangularity. The correlation of pumpout with the loss of axisymmetry suggests that neoclassical transport processes involving locally trapped particles near the helically displaced magnetic axis, previously believed to be important only in stellarators, may account for the phenomenon in tokamaks as well.

1. Introduction

ECH and ECCD are attractive candidate heating and current drive methods for future tokamak experiments, in particular ITER. However these methods appear to be at the origin of unexpected transport phenomena, which are potentially important for the confinement of fusion plasmas. In several past and present experiments, ECH is often seen to lead to a reduction of plasma particle density and confinement [1,2]. Such a phenomenon is also observed in stellarators, where it is at least qualitatively explained by neoclassical transport processes (thermodiffusion) arising from the presence of locally trapped particles due to the existence of magnetic field modulations throughout the plasma cross section [3]. Since the toroidal magnetic field ripple is very small on axis in most tokamaks, there are in principle no locally trapped particles in the core of axisymmetrical tokamaks. As a result the pumpout effect in tokamaks has remained unexplained.

The latest evidence from the TCV tokamak [4] (R_0=0.88m, a<0.25m, B_T<1.54T, I_p<1.2MA), which is currently equipped with 3 MW of ECH at the second harmonic (82.7GHz), suggests that pumpout in stellarators and in the core region of tokamaks is most probably of the same physical origin. Whereas in stellarators the field modulation is a built-in feature of the magnetic configuration, in tokamaks it can result from MHD perturbations caused by instabilities affecting the plasma core, especially inside the $q = 1$ surface. The presence of an $m/n = 1/1$ island causes the core to be helically displaced. As a result trapped particles exist even on the axis, just as in a heliac configuration. The coexistence of locally and toroidally trapped particles within the $q = 1$ surface can be expected to give rise to competing transport phenomena, including pumpout, since the off-diagonal terms associated with these two classes of particles have opposite signs.

2. Experimental evidence

Fig. 1 shows sawtooth oscillations using soft X-ray and interferometer signals in an ECH discharge with deposition outside (a) and inside (b) the sawtooth inversion radius r_{inv}. While deposition outside r_{inv} leads to sawteeth with positive ramps on both signals, deposition inside r_{inv} leads to negative density ramps (inverted sawteeth) in this low triangularity discharge (δ_{95}=0.22). The phenomenon is observed for $P_{ECH} > 0.5$ MW, as shown in Fig. 2 for Ohmic

and ECH phases of the same discharge. Fig. 3 shows the crash amplitudes $\Delta\bar{n}_{e0}/\bar{n}_{e0}$ from an ECH power scan for low and high triangularity obtained from a central line integrated electron density signal.

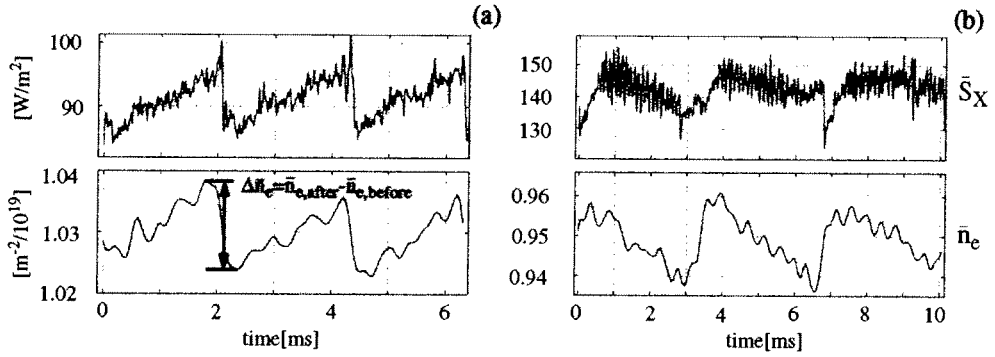

*Fig. 1 Discharge No. 16061. Sawtooth oscillations from a central line integrated soft X-ray channel (top) and from a central interferometer channel (bottom), corresponding to ECH power deposition outside **(a)** and inside **(b)** the sawtooth inversion surface.*

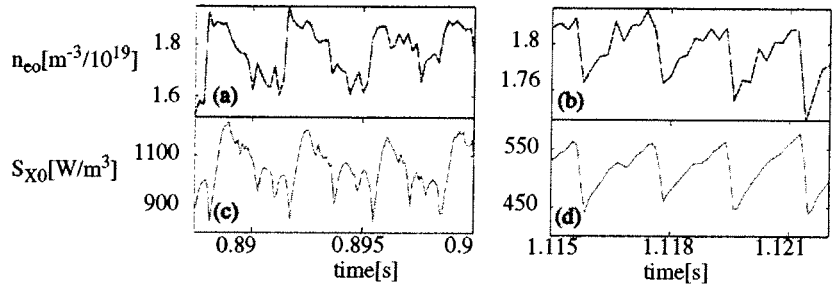

*Fig. 2 Discharge No. 14475. Sawteeth at different injected ECH power from Abel-inverted central electron density **(a, b)** and on local soft X-ray emissivity **(c, d)**.*

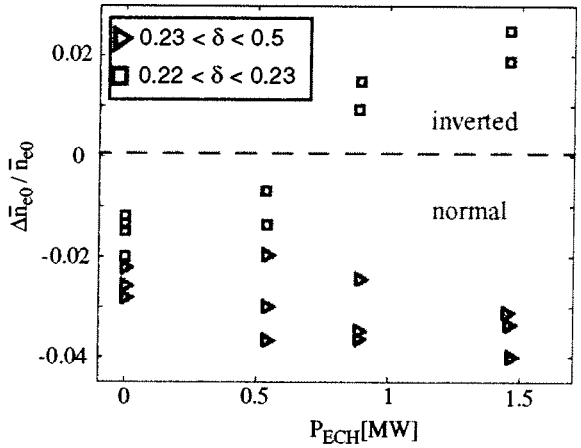

Fig. 3 Relative variation of $\bar{n}_{e0}$ at the sawtooth crash for different plasma triangularity and injected ECH power. Positive and negative $\Delta\bar{n}_{e0}/\langle\bar{n}_{e0}\rangle$ values indicate respectively inverted and normal sawteeth

At high triangularity no pumpout is observed. It is a generally observed feature in TCV, both in Ohmic [5] and ECH plasmas [6], that $m/n = 1/1$ pre-and postcursor oscillations are absent at high triangularity and are increasingly present as triangularity is reduced, suggesting a link between mode activity and the observed particle transport. Approximate heat and particle balance estimates for the plasma inside the sawtooth inversion radius show that the convectively expelled thermal energy during the inverted ramp phase is a small fraction, less than 10%, of the total loss power from that volume. In sawtoothing plasmas significantly hollow density profiles cannot develop because the crashes regularly flatten density and

temperature profiles. However with ECH and ECCD many situations arise when sawteeth are stabilized for long enough (typically 10 ms or more) for profiles to approach steady-state and the hollowness to become significant enough for measurements using the TCV Thomson scattering system. The absence of sawteeth is often accompanied by saturated (1, 1) modes (as well as higher harmonics), indicating that the plasma still has a $q = 1$ surface. Fig. 4 shows typical examples of electron density in a fully sustained Co-ECCD and a Counter-ECCD discharge showing that the pumpout phenomenon is very general and does not depend on the parallel velocity of the electrons interacting with the heating beams.

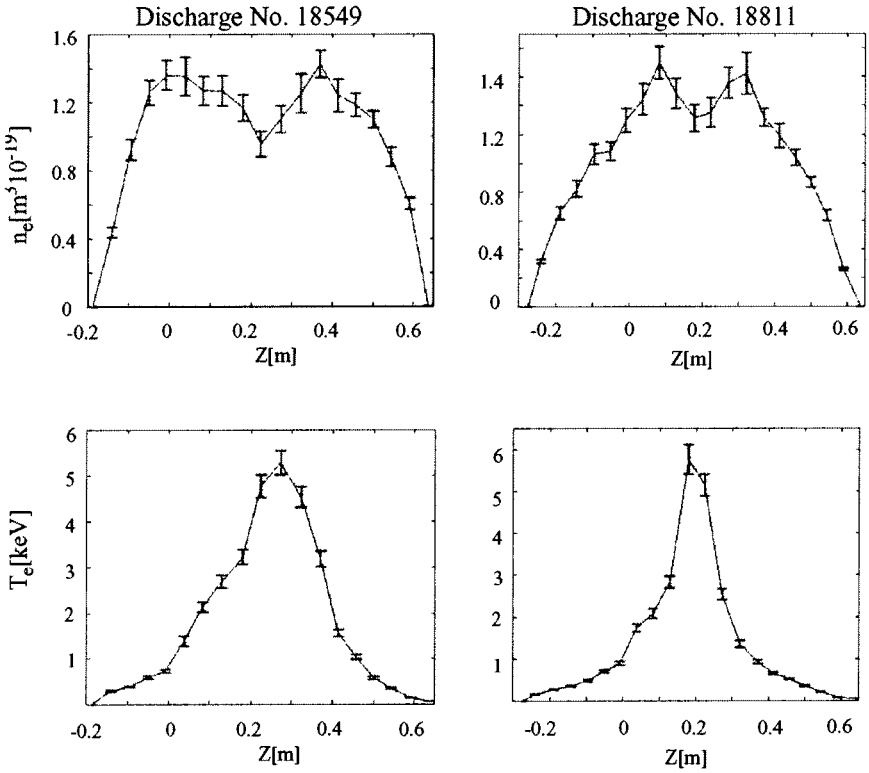

Fig. 4 Examples of electron density (top) and temperature (bottom) profiles in a Co-ECCD (left) and a Counter-ECCD discharge (right).

3. Discussion

Several explanations for "pumpout" have been suggested. Pondermotive effects are the least likely, both because the potentials are easily shown to be far smaller than electron temperatures and because the beams are very localized poloidally and toroidally, whilst the phenomenon is observed outside the beam region. In principle the thermal force [7] could transfer parallel momentum to ions in the presence of a parallel electron temperature gradient. Such an explanation might fit into the (controversial) picture of electron diffusion in stochastic magnetic fields, but would not make the economy of considering ion orbits. The first explanation based on particle orbits was proposed by Hsu et al [8]. According to this theory, the ECH, by increasing the perpendicular energy of electrons of low parallel velocity, causes many of these to become toroidally trapped, leading to the buildup of an excess of banana-electrons and thereby a poloidal charge asymmetry which produces a net electric field oriented in the direction of the major radius ("banana pile-up"). The resulting increased ion vertical drift velocity, by widening ion orbits, would then increase the neoclassical diffusivity and lead to increased particle losses.

The banana pile-up explanation however does not explain why pumpout is observed with heating on the high field side of the magnetic axis, which is the case in most TCV experiments, nor with large toroidal injection angles as are used for ECCD experiments, when the power is deposited to electrons with large $v_{//}$. A model which only predicts increased diffusivities cannot

explain the observed gradient reversal. Finally banana pile-up cannot account for the observed importance of MHD modes.

We propose that loss of axisymmetry provides the crucial physics for this phenomenon by allowing the existence of locally trapped particles, which are not confined in the core region. Fig. 5 shows a schematic of the magnetic configuration inside the $q = 1$ surface when a magnetic island causes a helical displacement of the magnetic axis by a distance ξ. This displacement is typically of order 10% of the minor radius, as determined from X-ray tomography. The magnetic field modulation produced by the displacement inside the $q = 1$ surface is $\Delta B/B \cong \xi/R_0$. Particles with $|v_{//}/v| < (2\xi/R_0)^{1/2}$ on the low field side are not confined and can be expected to drift outside of the $q = 1$ volume where they find themselves in an (approximately) axisymmetrical field configuration and may remain confined as banana particles. Some of the particles escaping from the core region may also become trapped in the toroidal field ripple (which increases with distance from the core) and drift out of the plasma altogether.

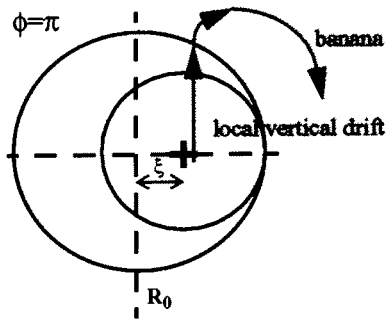

Fig. 5 Helically displaced plasma core and locally trapped particle orbit (schematic).

The nature of a configuration can be characterized by the parameter $\alpha = \varepsilon B/(\Delta B q n)$, where ε is the aspect ratio, q the safety factor and n the number of toroidal modulations [9]. For the configuration considered in Fig.5 $\alpha \cong \rho/\xi$. It is stellarator-like for $\rho < \xi$ and becomes increasingly like an ideal tokamak when $\rho > \xi$. In principle both collisions and direct perpendicular energy transfer by ECH can cause electrons to become trapped. Since pumpout occurs even with ECH on the high field side, where trapped electrons cannot be created directly, we must assume that collisional trapping is the most important of these mechanisms.

The vicinity of the displaced magnetic axis may act as a sink from where locally trapped particles are lost to beyond the non-axisymmetrical region (typically outside $q=1$). The coexistence of two classes of trapped particles may also give rise to competing transport phenomena. In neoclassical theory [9] trapped particles give rise to coupled heat and particle transport, of the generic form

$$\Gamma_{e,i} = D_{11}^{e,i} n_{e,i} \left[\left(\frac{n'_{e,i}}{n_{e,i}} + \frac{q Z_{e,i} \Phi'}{T_{e,i}} \right) + d_{12}^{e,i} \frac{T'_{e,i}}{T_{e,i}} \right] \qquad (1)$$

d_{12} giving rise to thermodiffusion (primes designate spatial derivatives). A steady state solution is obtained in the usual way by setting the ion flux to zero and inserting the ambipolar potential into the electron equation, with the result

$$\frac{n_e'}{n_e} = -d_{12}^e \left(1 + \frac{d_{12}^i T_i'}{d_{12}^e Z T_e'} \right) \Big/ \left(1 + \frac{T_i}{Z T_e} \right) \cdot \frac{T_e'}{T_e} \approx -d_{12}^e \frac{T_e'}{T_e} \qquad (2)$$

where the last approximation pertains to typical conditions on TCV, where $T_e >> T_i$. For fluxes caused by toroidally trapped particles we have $d_{12}^t = -0.5$, corresponding to an inward pinch, while for locally trapped particles $d_{12}^l \sim 1$ in the long mean free path regime and $d_{12}^l \sim 3.5$ in the 1/ν regime [9], corresponding, for peaked temperature profiles, to an outward flux. In a realistic situation both processes as well as anomalous transport must be expected to compete. Formally we may write the total flux as a sum $\Gamma = \Gamma^t + \Gamma^l + \Gamma^a$, with $D_{11} = D_{11}^t + D_{11}^l + D_{11}^a$ and the superscript ^{a} refers to anomalous. The resulting off-diagonal term is then

$$d_{12} = (d_{12}^t \cdot D_{11}^t + d_{12}^l \cdot D_{11}^l + d_{12}^a \cdot D_{11}^a)/D_{11} \quad (3)$$

(Note that D_{11}^x may depend on electric fields). In the absence of an anomalous pinch, a hollow profile is expected where $D_{11}^l/D_{11}^t > -d_{12}^t/d_{12}^l \sim 0.5$, e.g. sufficiently close to the displaced axis. Fig. 6 shows the relations between the temperature and density gradients obtained in a variety of discharges including, Co- and Counter-ECCD. Although the results are qualitatively consistent with the existence of neoclassical outward fluxes due to locally trapped particles, the observed density gradients $\langle \nabla n_e \rangle / n_{e0} \sim -0.5 \cdot \langle \nabla T_e \rangle / T_{e0}$ in hollow profiles are smaller than expected from locally trapped particles alone. From Eq. (3) we see that the effect of anomalous diffusion, which generally can be expected to dominate, is to erode the strong steady-state gradients predicted by Eq. (2), which would be produced by neoclassical effects alone. We attribute the absence of strongly hollow profiles to the smallness of the stellarator-like region where local trapping dominates and to the competing effects of toroidal trapping and anomalous diffusion outside this region.

The above considerations should be regarded as tentative since it is not clear wether standard neoclassical theory can be applied. Locally trapped particle orbits for instance, even in the presence of electric fields, may well be larger than the stellarator-like region near the magnetic axis, as indicated in Fig.5. Clearly future work to test and refine the emerging physical picture of the pumpout phenomenon in tokamaks will require numerical orbit calculations and an improved understanding of neoclassical transport in the particular magnetic configurations which result when MHD instabilities break the symmetries of the ideal tokamak.

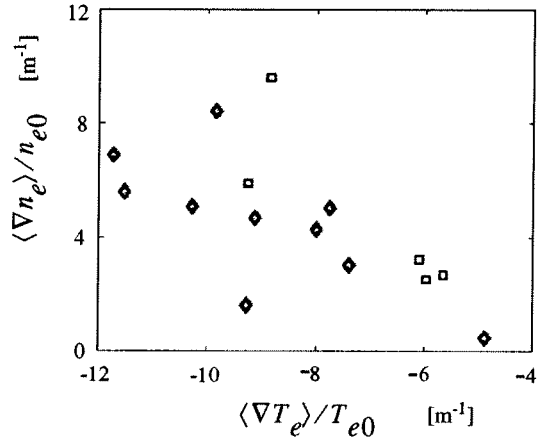

Fig. 6 Average electron density versus average T_e gradients over region with hollow n_e profiles. squares: Co-ECCD diamonds: Counter-ECCD

Acknowledgement: This work was partly supported by the Swiss National Science Foundation. The authors thank K. Lackner, H. Maassberg and W.A. Cooper for stimulating discussions.

References

[1] TFR-GROUP, *Nucl. Fusion* **25** (1985) 1011.
[2] V. Erckmann and U. Gasparino, *Plasma Phys. Control. Fusion* **36** (1994) 1862.
[3] H. Renner, W7-AS Team, NBI Group, ICF Group and ECRH Group, *Plasma Phys. Control. Fusion* **31** (1989) 1579.
[4] F. Hofmann, et al., *Plasma Phys. Control. Fusion* **36** (1994) B277.
[5] H. Weisen, et al., Nucl. Fusion **37** (1997) 1741.
[6] H. Reimerdes, et al., *Plasma Phys. Control. Fusion* **42** (2000) 629.
[7] Braginskii in Review of Plasma Physics **1**, Ed. M. A Leontovich (1965) 205
[8] J. Y. Hsu, at al., *Phys. Rev. Lett.* **53** (1984) 564.
[9] L. M. Kovrizhnykh, Nucl. Fusion **24** (1984) 851.

Structural Materials for Fusion Reactors

M. Victoria, N. Baluc and P. Spätig
EPFL-CRPP Fusion Technology Materials, CH-5232 Villigen PSI, Switzerland

e-mail: Philippe.Spatig@psi.ch

Abstract: In order to preserve the condition of an environmentally safe machine, present selection of materials for structural components of a fusion reactor is made not only on the basis of adequate mechanical properties, behavior under irradiation and compatibility with other materials and cooling media, but also on their radiological properties, i.e. activity, decay heat, radiotoxicity. These conditions strongly limit the number of materials available to a few families of alloys, generically known as low activation materials. We discuss the criteria for deciding on such materials, the alloys resulting from the application of the concept and the main issues and problems of their use in a fusion environment.

1. Introduction

The development of adequate structural materials is a major step towards fusion reactors becoming an efficient source of energy, particularly if the promise of an environmentally safe machine is to be maintained. The first wall, divertor, limiters and breeding blanket components are subjected not only to the high energy neutron environment resulting from the fusion reactions, but also to strong mechanical, heat and electromagnetic loadings. These conditions create a very severe operation frame for the materials used in these elements and have led to a long developmental path for the candidate materials.
The main idea in the materials development program to comply with the safety conditions is the development of ***low activation materials***. The **criteria** for deciding on such materials, the resulting **material families** resulting from the application of the concept and the **main issues and problems** of their use in a fusion environment are discussed below.

2. Effects on materials due to the fusion reactor environment.

Eighty percent of the energy released by the D-T fusion reaction are transferred by 14 MeV neutrons to the first wall and breeding blanket. The remaining 20% are carried by α-particles issued from the same reaction, that together with other low energy neutral and charged particles will induce sputtering, erosion and blistering in the plasma facing materials.
About 10% of the energy of the 14 MeV neutrons will be deposited in the first wall, the remaining energy being transferred mostly to the blanket [1]. Two types of **radiation effects** are produced in the materials:

(i) Inelastic (n,x) interactions with nuclei which yield **transmutation products** and lead to the production of He, H and other impurities in the bulk of the material.
(ii) The neutrons themselves plus the recoils resulting from the above nuclear reactions transfer energy to lattice atoms through elastic collisions and displace them from their normal sites. Through an iterative process, a **displacement cascade** is formed. About 10% of the vacancies and interstitial defects originally formed survive the evolution of the cascade and lead to the formation of a defect microstructure that hardens the material, to the formation of voids, to the redistribution of elements in the alloy inducing segregation and possibly to phase transformations.

The neutrons slow down as they penetrate the reactor structure, so the neutron spectrum changes with penetration depth. This will modify the recoil energy spectra as well as the transmutation rate, the magnitude of the radiation effects will be typically different in the first wall and blanket.
Radiation damage depends strongly on irradiation temperature T_{irr} and three regions can be recognized in relation to the melting temperature of the material T_M:

(i) At low temperatures ($T_{ir} < 0.3T_M$) the vacancies do not yet evaporate from their clusters. The microstructure is dominated by defect clusters and results in radiation hardening and a degradation of the fracture toughness (embrittlement) of the material, increasing its ductile to brittle transition temperature.
(ii) In the region of $0.3T_{irr} < T_{irr} < 0.5\ T_M$, defects are strongly mobile and this results in phenomena such as radiation creep and swelling.

(iii) At still higher temperatures, the presence of He leads to embrittlement through the formation of bubbles at grain boundaries.

All the above described effects limit the life of the components.

3. Low activation materials

While the burning of fission fuel produces long lived actinides, the fusion reaction does not intrinsically yield other radioactive elements. But fusion neutrons will activate the materials surrounding the plasma and this fact conditions the waste management and disposal scenarios. Under accident conditions, the decay heat is an important parameter, since heat enhances oxidation and possible volatilization and such release to the environment is the main contamination hazard in a loss of coolant condition [2].

In order to evaluate these parameters, extended cross section data libraries together with decay and activation data have been developed. In Europe, the present version of the FISPACT97/EAF97 [3,4] inventory code together with the decay and activation libraries EASY [5], which includes five reference fusion reactor neutron spectra (first wall, blanket, shield and two magnetic coils), have been used to show that only a few primary elements can be considered. They are C, Si, Ti, Fe, Cr and V. Other elements, such as W can be used in limited quantities. Moreover, all of the evaluations made up to present show the importance of the presence of typical tramp impurities present in these metals, such as Al, Ni, Ag, Co, Nb and others, that are detrimental because of their poor radiological properties.

4.Main issues in development of Low Activation Materials

The most intensive development in the past fifteen years has been that of the ***ferritic-martensitic steels*** (Low activation steels or LAS), based on the 7-10CrWVTa composition and which has led to the production of large casts in Japan (F82H steel) and in Europe (the EUROFER97 steel). These steels have reasonable thermophysical properties and, from irradiation experience in fast reactors to well over 100 dpa [6], a substantial resistance to swelling and high temperature embrittlement. Moreover, they have good compatibility with either water or He coolants and Li-breeders. They are being developed for a temperature window up to 773 K.

A critical issue in these steels is the existence of a ductile to brittle transition temperature (DBTT), which increases with irradiation to temperatures well above room temperature, making the steel unusable as a structural component. It has been shown that reducing the Cr content to less than 9 % strongly decreases the sensitivity to this phenomena [7] and in Europe a number of LAS families (OPTIFER, OPTIMAX) have been developed on this basis. It has also been shown that a positive consequence of using pure materials and clean processing is that low DBTT temperatures are obtained in the unirradiated steel, which increase only moderately after irradiation. A typical data set is that obtained for the difference in DBTT, measured from Charpy tests, between the virgin and irradiated condition (ΔDBTT) in the F82H and OPTIMAX A LAS, shown in Fig. 1. In both cases, the DBTT is below room temperature after irradiation to 2.5 dpa.

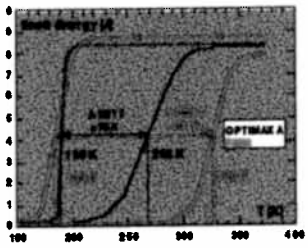

Figure 1:Shift of the DBTT for the F82H and OPTIMAX A steels after 2 dpa irradiation

There are a number of issues still open regarding the behavior of these LAS:

(i) Although the normal tensile properties are practically not affected, there is an increasing body of evidence showing that, contrary to what was expected in this temperature region, the presence of He induces an additional shift in the DBTT, already at low He contents [8]. There is a yet no clear unerstanding of what mechanism is operative

(ii) Although the actual reactor is expected to operate in a quasi-continuous mode, the design of intermediate or demonstration machines operates still in a pulsed fashion (1000 s pulses in ITER). Such mode introduces mechanical damage through fatigue. As it is important to understand the actual dynamical situation under irradiation, which is nearer to the behavior of the material in the reactor, in-beam fatigue tests have been performed in the F82H steel under a 590 MeV proton beam irradiation [9].

(iii) The effects of ferromagnetism on plasma stability have to be investigated.

Titanium alloys have a number of properties that make them attractive structural material candidates for fusion reactors. High strength-to-weight ratio, intermediate strength values, good fatigue and creep rupture properties, small modulus of elasticity, high electrical resistivity, heat capacity, low coefficient of thermal expansion, low long-term (< 10 years after shutdown) residual radioactivity (after V and Cr, Ti has the fastest decay rate), a high corrosion resistance together with good compatibility with coolants such as lithium, helium and water, high workability and good weldability and commercial availability with established mine and mill capacity are some of the favorable properties [10]. Because of the numerous current applications of titanium alloys in the aerospace and medical domains, there exists an extended properties database and industrial experience on these materials. Ti-alloys can be divided into three major classes determined by their phase constituency, they are referred to as the alpha (α), beta (β) and alpha/beta (α/β) alloys, where the α phase is hcp and the β phase is bcc. The alloying elements used in the titanium system can be divided into two classes according to which phase the element stabilizes. The substitutional α stabilizers are Al, Zr and Sn, while the β stabilizers are V, Cr, Mn, Fe, Co, Ni and Mo. Furthermore, the intermetallic TiAl has also been proposed in the Japanese program. Leguey et al. [11] have recently reported results after irradiation with 590 MeV protons (mean dose rate: $3x10^{-6}$ dpa.s^{-1}; mean He production rate: 50 appm/dpa) of pure Ti, for irradiation doses ranging between 10^{-3} and 10^{-1} dpa. Proton-irradiation at 330 K induces a significant increase in the critical stress measured at 0.2% plastic strain [11] and a decrease in the work hardening rate, as shown in Fig. 2. Hardening is of the order of about 40% per dpa for a dose of 0.03 dpa. It clearly relates to the irradiation-induced formation of a high density of defect clusters observed with transmission electron microscopy (TEM). About 20% of the observed defects were identified as dislocation loops with a mean apparent size of 5 nm. No clear correlation could be established between ductility and irradiation dose, due to large scattering in the measurements. However, the total strain at fracture of all deformed specimens (irradiated or not) lies between 18 and 30%. The TEM observation of specimens irradiated to 0.03 dpa and deformed up to fracture shows the simultaneous annihilation of defect clusters as a result from interactions with mobile dislocations together with the formation of twins and dislocation cells. No void formation was observed. A comparison of the mechanical properties of the α -Ti-5Al-2.4Sn and $\alpha+\beta$ Ti-6Al-4V alloys has been performed by Marmy et al. [12] also after irradiation with 590 MeV protons. In the unirradiated alloys it was found that the resistance to tensile deformation of both alloys is very similar. The critical stress measured at 0.2% plastic strain, $\sigma_{0.2}$, has a mean value of about 800 MPa at ambient temperature (that is about 40% higher than that exhibited by a 9CrWV low activation ferritic/martensitic steel) and 450 MPa at 500°C (the same value as that of the ferritic/martensitic steel). Both alloys exhibit good ductility. The total elongation of the $\alpha+\beta$ alloy, between 15 and 20%, is slightly higher than that of the α alloy, whatever the test temperature between 20 and 500°C. After proton irradiation, see Fig. 3, hardening and loss of ductility are observed in both alloys. However, these phenomena are much stronger for the $\alpha+\beta$ alloy than for the α alloy. In fact, irradiation at 623 K affects the $\alpha+\beta$ alloy strongly, with an increase of about 40 % in the yield strength and a 65 % decrease in tensile elongation, while the α alloy irradiated under the same conditions shows only very little hardening and about 3% reduction in elongation. The embrittlement of the $\alpha+\beta$ alloy is probably associated with the presence of a radiation induced phase precipitation observed in TEM. Similar phase instability under irradiation in the Ti6Al4V has already been observed by a number of investigators. Probably the biggest disadvantage of titanium and its alloys in a fusion environment is their high chemical affinity with hydrogen which leads to hydrogen embrittlement and a expected large tritium inventory. Early work established that for impact embrittlement, a critical level of hydrogen concentration was required and that the onset of embrittlement was probably associated with precipitation of the hydride phase [13]. Subsequently, it has been shown that additions of aluminum raise the critical level of hydrogen for embrittlement and this was tentatively attributed to an increase in the solubility limit [14]. The hydrogen solubility in titanium was first estimated to be less than 100 wppm below 523 K [15]. In general, the alloys that consist primarily of α phase have a lower solubility for hydrogen than alloys that are primarily β phase. In the case of $\alpha+\beta$ alloys, the solubility increases with increasing amounts of β phase. The three major sources of hydrogen isotopes in a fusion reactor environment are [10]: hydrogen produced in the metal by neutron transmutation reactions,

interactions with the deuterium and tritium (D-T) fuel in the plasma chamber and interactions with tritium in the breeding material.

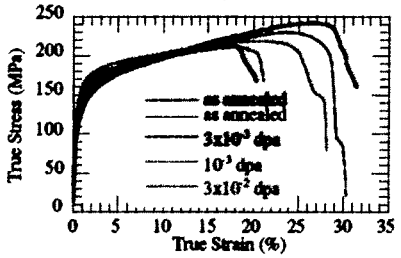

Figure 2: Tensile curve on pure Ti before and after proton irradiation

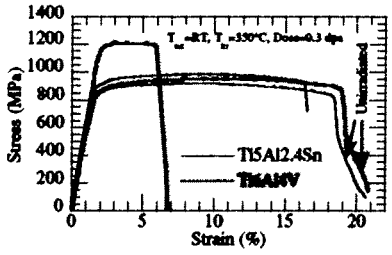

Figure 3: Tensile curve of Ti alloys, unirradiated condition and after 0.3 proton irradiation

Therefore, in order to make practical use of titanium alloys for fusion applications, hydrogen barrier coatings are necessary to prevent hydrogen intake and eventual embrittlement of the material. Preliminary attempts of depositing a graded coating with a Cr_2O_3 +(Si or Ti)O_2 top layer on the Ti-5Al-2.4V α-alloy have been recently performed at the Materials and Surface Department of SULZER Innotec AG. These coatings have been tested for structural integrity and hydrogen permeation and appear quite promising [16].

vanadium alloys are also considered [17] because of their low thermal expansion which coupled to a low elastic modulus leads to low thermal stresses and a high heat flux capability. Their compatibility with pure Li makes them a good choice for a liquid lithium coolant breeder blanket concept. The typical operating window of this design, from 623 to 1023 K and 1 MPa pressure, requires high temperature strength and good creep properties, conditions that are fulfilled by the V-(4-5)Cr-(4-5)Ti [18]. The feasibility of fabricating components from the alloy is being demonstrated by its use in the DIII-D RDP, for which a 1200 kg cast has been produced and worked into rod, plate and sheet. Postirradiation results [18] after irradiation at temperatures below 600 K show strong radiation hardening and a reduction of the uniform strain to values below 1% and an upward shift of the in the DBTT of the order of 560 K. The uniform irradiation increases at higher irradiation temperatures: is 6% after irradiation at 873 K. A correlation can be made indicating that brittle fracture behavior occurs whenever the yield strength exceeds 700 M Pa.
The development of electrically insulating walls for coolant channels is a critical issue for self-cooled liquid metal systems. Of the candidate coatings AlN deposited by vapor deposition have been shown unstable, while CaO coatings exhibit good electrical resistance during exposure to Li at 700 K.

Fibre reinforced SiC-SiC ceramic composites have gained strong interest in the fusion materials community due to their good low activation and decay heat properties at short and intermediate decay times, coupled to high mechanical strength for temperatures up to 1273 K. Their microstructure consists of SiC embedded in a SiC matrix through a fiber-matrix interphase and are typically synthesized by the chemical vapor infiltration (CVI) process. They have a good compatibility with He, which makes them primary candidates for a high temperature, He cooled blanket. Early irradiation results [19] indicated a rapid degradation of the mechanical properties already at doses of ≈ 1 dpa, due to dimensional instability of the fiber and carbon interphase that leads to delamination. The present generation of SiC composites, with low oxygen, quasi-stoichiometric SiC fibers of enhanced crystalline perfection seem to have much improved properties after irradiation [20]. A number of critical issues are at present of concern:

(i) The relatively low thermal conductivity of SiC composites and the fact that it is further reduced by irradiation. This has already much improved in the materials produced with the new Hi Nicalon-S fibers in which a thermal conductivity value of the order of 50 W/mK has been measured.
(ii) Void swelling in the temperature window of application.
(iii) The (n,x) cross-sections in Si are about one order of magnitude higher than for LAS or V-alloys (about 150 appm He per dpa). The effects of this large amount of He at high temperatures is as yet unknown.

(iv) The CVI process produces a microstructure that has about 10% porosity and is therefore permeable to gases.
(v) Technologically, methods for fabricating large components and of joining the composite to itself and to other metals need to be developed.

6. Conclusions

- In order to realize the potential safety and environmental advantages of fusion, ***low activation materials*** are being developed within a large international collaboration. The materials choice in this case is based not only on adequate mechanical properties, behavior under irradiation, and compatibility with other materials and cooling media, but also on their ***radiological properties***.
- The alternative alloy classes being studied are ferritic-martensitic steels, V and Ti alloys and SiC-SiC ceramic composites. At present, the ferritic-martensitic steels have achieved the greatest technological maturity.
- Common to all the alternatives is the lack of irradiation in a fusion relevant neutron environment, which limits our knowledge of the behavior of these materials in the proper reactor conditions (by example, on synergistic He effects on embrittlement, creep and swelling). Therefore, the availability of an ***adequate neutron source***, such as the proposed International Fusion Materials Irradiation Facility (IFMIF) is of primary importance for the future development of the program.
-

Acknowledgements
The present work has been supported by the European Fusion Technology Programme.

References

[1] D.R. Harries, "Ferritic Martensitic Steels for Use in Near Term and Commercial Fusion Reactors", Proceedings of the Topical Conference on Ferritic Alloys for Use in Nuclear Energy Technologies, Snowbird, Utah, June 19-23, 1983.
[2] K. Ehrlich, Phil. Trans. R. Soc. Lond. A 357 (1999) 595.
[3] D.R. Harries, G.J. Butterworth, A. Hishinuma, F.W. Wiffen, J. Nucl. Mater. 191-194 (1992) 92.
[4] R.A. Forrest, J.C. Sublet, FISPACT-97 User Manual, UKAEA FUS 358 Report, 1997.
[5] R.A. Forrest, J. Kopercky, "The European Activation System (EASY)", IAEA Advisory Group Meeting on FENDL-2, Vienna, November 1991.
[6] D.S. Gelles, J. Nucl. Mater. 233-237 (1996) 293.
[7] R.L. Klueh and G.J. Alexander, J. Nucl. Mater. 233-237 (1996) 336.
[8] R. Lindau, A. Möslang, D. Preininger, M. Rieth and H.D. Röhrig, "Influence of He on impact properties of reduced-activation ferritic-martensitic steels", Proc. Intern. Conf. On Fusion Reactor Mater. (ICFRM8) Sendai, Japan, October 1997.
[9] P. Marmy, "In beam fatigue properties of the F82H steel", Proc. Intern. Conf. On Fusion Reactor Mater. (ICFRM9), Colorado, USA, September 1999.
[10] J.W. Davis and D.L. Smith, J. Nucl. Mater. 85 & 86 (1979) 71.
[11] T. Leguey, C. Bailat, N. Baluc and M. Victoria, to be submitted at the MRS Symposium on 'Microstructural Processes in Irradiated materials', Fall Meeting 2000.
[12] P. Marmy, Report on ITER TASK BL 14.2: Titanium Alloys Irradiation Testing (2000).
[13] C.M. Craighead, G.A. Lenning and R.I. Jaffee, Trans. AIME 194 (1952) 1317.
[14] L.W. Berger, D.N. Williams and R.I. Jaffee, Trans. AIME 212 (1958) 509.
[15] G.A. Lenning, C.M. Craighead and R.I. Jaffee, Trans. AIME 200 (1954) 367.
[16] T. Leguey, Private comunication.
[17] S.J. Zinkle, H. Matsui, D.L. Smith, A.F. Rowcliffe, E. van Osch, K. Abe and V.A. Kazakov, J. Nucl. Mater. 258-263 (1998) 205.
[18] B.A. Loomis and D.L. Smith, J. Nucl. Mater. 212-215 (1994) 799.
[19] P. Fenice, A.J. Frias Rebelo, R.H. Jones, A. Kohyama and L.L. Snead, J. Nucl. Mater. 258-263 (1998) 215.
[20] A. Kohyama, this Conference.

Design of ITER-FEAT RF Heating and Current Drive Systems

G. Bosia 1), K. Ioki 1), N. Kobayashi 1), P.Bibet 2), R.Koch 3), R.Chavan 4), M.Q.Tran 4), K. TAKAHASHI 5), V.Vdovin 6)
1) ITER Joint Central Team, Boltzmannstrasse 2, 85748 Garching,
2) DRFC/STID/FCI, CE Cadarache BP n°1, 13108 St Paul Lez Durance
3) Plasma Physics Laboratory, ERM/KMS, 30 Av. de la Renaissance, 1040 Brussels
4) CRPP, Ass. Euratom – Conf. Suisse, PPB, EPFL 1015 Lausanne
5) RF Heating Laboratory, JAERI Naka-machi, Naka-gun, Ibaraki-ken 311-01 JAPAN
6) Kurchatov Institut for Atomic Energy, Moscow
e-mail, bosiag@iterg.itereu.de

Abstract. Three RF Heating and Current Drive (H & CD) systems are designed for ITER-FEAT: an Electron Cyclotron (EC), an Ion Cyclotron (IC) and a Lower Hybrid (LH) System. The launchers of the RF systems use four ITER equatorial ports and are fully interchangeable. They feature equal power outputs (20 MW/port), similar neutron shielding performance, and identical interfaces with the other machine components. An outline of the final design is given in the paper.

1. Introduction

The achievement of the main ITER-FEAT operation regimes has set new challenges to the design of Heating and Current Drive (H&CD) Systems. ITER-FEAT is a driven machine, whose performance rests, for a large part, on auxiliary heating system availability and performance. Three RF auxiliary heating systems: Electron Cyclotron (EC), Ion Cyclotron (IC), Lower Hybrid (LH) and (negative ion) a Neutral Beam Injection (NBI) system have been developed during EDA and their design has been revised in the last year, to fulfil the latest ITER requirements.

The key issues of the reference scenario are to deliver sufficient central heating power to access the H-mode regime, to rise the plasma temperature as the density is increased to a plasma pressure adequate for the requisite fusion power, and to maintain burn by controlling excursions about the operating point and pressure driven instabilities. Steady state operation requires an active current profile control, necessary to access enhanced confinement regimes, in which a large fraction of the plasma current is generated via the bootstrap effect. The onset of neoclassical tearing modes (NTM) potentially poses serious challenges to ITER high-β operation and provisions for active control by ECCD appears at present to be unavoidable.

The reduced contribution of α-particles to bulk plasma heating requires further optimization of the heating systems and a more flexible approach in their use. A graded implementation of the H&CD power is now foreseen in ITER, with different options, depending on the evolution of the experimental program.

H&CD systems are also required to heat non-fusion plasmas in early operating phases, for example, to commission the divertor target plates. They are used for plasma initiation assisted start-up and soft-landing. They have capability of controlling sawteeth, to induce plasma rotation, and can provide ancillary services such as wall conditioning.

The reduction of ITER size has decreased number and dimensions of the ports available, and increased the competition for access to plasma. For the heating systems, this is reflected as a general increase of the design power density. Four equatorial ports are now assigned to RF systems and four additional upper ports are used for ECCD NTM stabilization.

2. General design features

A modular approach is adopted in the design of the RF launchers located in the equatorial ports. They are designed as interchangeable plugs with the same nominal installed power (20 MW/port), similar neutron shielding/activation performance, identical vacuum/tritium confinement boundaries and interfaces with the VV port, and the same remote maintenance requirements, interface and procedures.

The launcher assemblies are supported by the same mechanical structure, (cantilevered at the port closure plate and otherwise disconnected from the other port components), providing a standardized interface with vacuum vessel and blanket. At the plasma end, the RF plugs are flush with the blanket first wall and therefore shielded from conduction heat loads. A gap of 20 mm is allowed all around the plug perimeter from the port walls and an overlap of 30 mm of the adjacent blanket modules (dogleg) avoids direct neutron streaming in the gap. The nominal separation between plasma separatrix and the first wall in equilibrium condition is 12 cm.

For all systems, the primary confinement boundary is located at the vacuum vessel closure plate and a secondary vacuum extends up to the cryostat closure plate. Single-disk, water-cooled ceramic windows are used in each wave-guide or coaxial line. The dielectric window materials are different in different systems: BeO is used for IC and LH and polycrystalline diamond for EC.

The RF systems are designed to make maintenance operations simple, in situ and in the hot cell. All RF launcher assemblies are initially delivered fully commissioned thoroughly tested to full performance in test stand and leak tested and the integration in the port requires installation and sealing of the closure plate only. The plasma facing components are all easily detachable, to be replaced in hot cell in case of damage. The first wall is built in copper alloy, plated by a 3 mm Be layer, with cooling holes lined with 0.5 mm 316 SS LN, and welded to a base plate supported from top and bottom of the launcher frame

In all systems, a water cooled 316 SS LN nuclear shield limits the average activation level outside the primary closure plate to a level below 100 μSv/hour, 2 weeks after shutdown, sufficient to allow hands-on maintenance at that port closure plate location. A vacuum wave guide/transmission line assembly is located outside the primary vacuum boundary, in the inter-space between VV and cryostat closure plates.

High voltage regulated DC Power Supply Units, similar in design and specifications, are required for the main supply of the RF power sources (gyrotron oscillators for EC, multi-stage amplifiers for IC and klystron amplifiers for LH). Complex networks of plant parameter monitoring, control and data acquisition interface the RF systems with ITER central Control and Data Acquisition System (CODAC). Standardization in this area is also sought, to minimize costs and to simplify operation.

3. Electron Cyclotron System

The electron cyclotron system uses an equatorial port to initially deliver a power of 20 MW at 170 GHz for the H&CD and 2 MW at 120 GHz for plasma start-up assist. A second equatorial port is reserved for further power extension. Four upper ports are available to accommodate up to 30 MW of RF power at 170 GHz for Neo-classical Tearing Mode (NTM) stabilisation. Complementary beam steering capabilities are available in equatorial and

upper port launchers: the beams can be toroidally steered ± 12.5° in the former and poloidally steered ± 5° in the latter.

The equatorial launcher (Figure 3a) consists of a front shield, 3 sets of steerable mirrors,

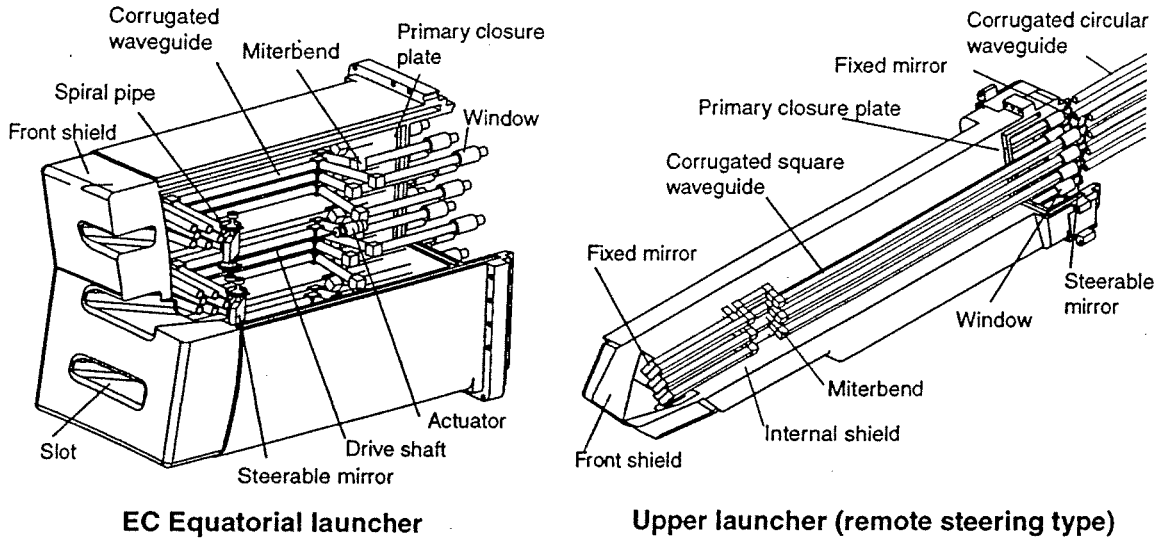

FIG. 3 a) Equatorial Launcher, b) Upper launcher

collecting 8 RF beams each, 24 circular corrugated wave-guides, miter-bends, diamond windows located at the port primary closure plate of the launcher. The front shield reduces the high-energy neutron flux and plasma radiation on the internal elements, has 3 horizontal injection slots and is segmented several modules. The steerable mirrors are supported by bearings at a pivot end and water-cooled to accommodate RF power loss (about 50 kW/mirror), plasma radiation and nuclear heat.

A CVD diamond disc is used as a primary vacuum window in each line, owing to its low dielectric losses ($\tan\delta = 2 \times 10^{-5}$) and high thermal conduction (~2000 W/m°K), which allows a simple edge cooling of the disc. The RF power is transmitted from the window to the steerable mirror by standard corrugated circular wave-guides with an inner diameter of 63.5 mm and miter-bends installed in the frame with the internal shield structure.

In the upper launcher, shown in Figure 3.b), the same beam-mirror concept is used. Here a particular emphasis is devoted to an accurate focussing of the RF power on m=2 and m=3/2 plasma flux rational surfaces by injecting 6.7 MW of RF power from 8 corrugated wave-guides on four individually steered mirrors.

A complementary concept of "remote steering" (RS) is being developed in parallel for the geometry of this launcher, with the use of corrugated square cross-section wave-guides, a fixed exit mirror and (out-vessel) steerable mirror installed at an input of the wave-guide

4. Ion Cyclotron System

The IC H &CD system has been re-designed in order to substantially upgrade its power handling at constant RF voltage. A power of 20 MW is launched from an equatorial port (with a second port reserved for power upgrade) in the frequency range f = 35-55 MHz, which encompasses all important ion IC heating scenarios as shown in Table 4.1:

Table 4.1 Ion Cyclotron resonance for ITER-FEAT

Resonance	Frequency (MHz)	Comments
$2\Omega_T=\Omega_{He3}$	53	Second Harmonic and minority heating
Ω_D	40	Minority heating
FWCD	55	On axis current drive

The IC array (Figure 4.a) still consists of an array of 4x2 elements fed by 8 coaxial transmission lines each carrying a nominal RF power of 2.5 MW.

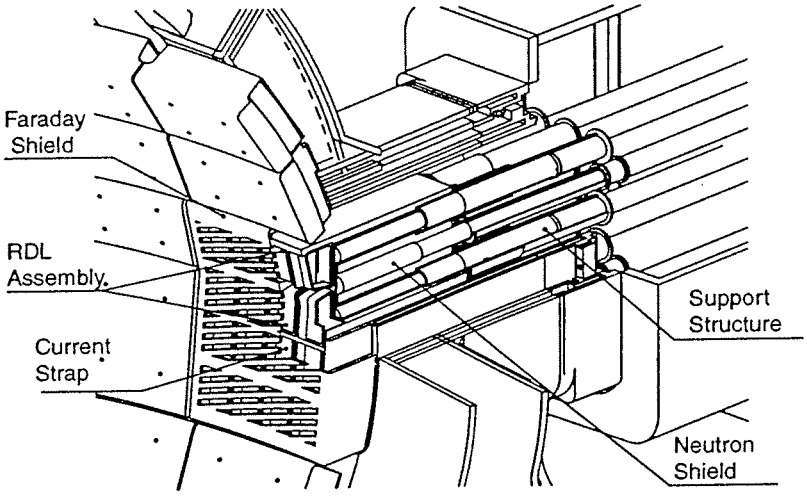

FIG. 4 a) Layout of IC array,

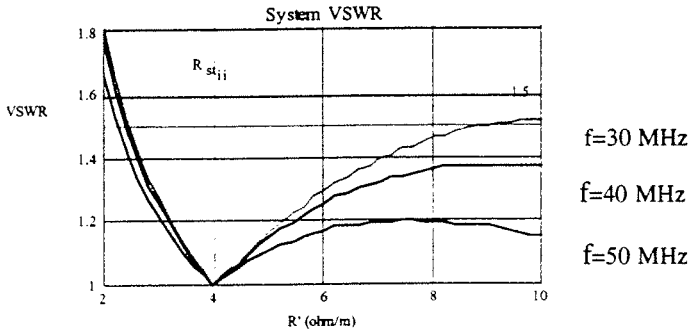

b) WSRW as function of load (R') and frequency (f)

Space limitations in the reduced size ports have imposed changes in the mechanical design. A variation of the Resonant Double Loop [1]concept used earlier has been adopted, with the series tuning reactance located at the input of the double loop, allowing a more convenient mechanical arrangement for the current straps, which are now self supporting. Short straps are used in order to decrease the operating voltage at the plasma interface and to improve its structural resistance

The tuning elements are short-circuited coaxial sections of variable length, supported by stub-like dielectric spacers and running in the port. The variable short circuits are tubular sections extruding from the neutron shield and can be individually maintained without disassembling the plug from the port.

The highest voltage regions are located about one meter away from the plasma interface. The electric field on plasma end is reduced to ~ 3.5 kV/mm at a power density of 9.2 MW/m^2. Calculations show that, with a judicious choice of the tuning network impedance, a large tolerance to load variations (such as ELMs, etc), is to be expected. (Figure 4.b) From the above one deduced that a power transfer efficiency < 95% can be obtained, over the whole range of loads and frequencies.

6. Lower Hybrid System

The LH system is designed to deliver a power of 20 MW at 5 GHz using a single equatorial port. The launcher is powered by 8 main transmission lines (MTL), connected to 24, 1 MW klystrons by means of combining units, to accommodate transmission losses of the order of 0.7 dB.

The launching structure (Figure 5) is composed of 4 passive/active multijunction (PAM) stacks, operating at a $N_{//0} = 2$ value of the radiated spectrum. Each PAM stack is made of 24 active and 25 passive quarter wavelength wave-guides. For an injected power of 20 MW, the power density in the wave-guide is 33 MW/m^2.

The splitting/phasing network of each PAM stack is composed of 4 rows of 3 TE_{10} to TE_{30} mode converters, each feeding 8 PAM wave-guides. A limited flexibility in $N_{//}$ ($1.9 < N_{//} <$

2.1) is obtained with this layout, by a toroidal phase variation of ± 90° around the nominal phase offset. Sections of standard oversize wave-guides connect the output of the four groups

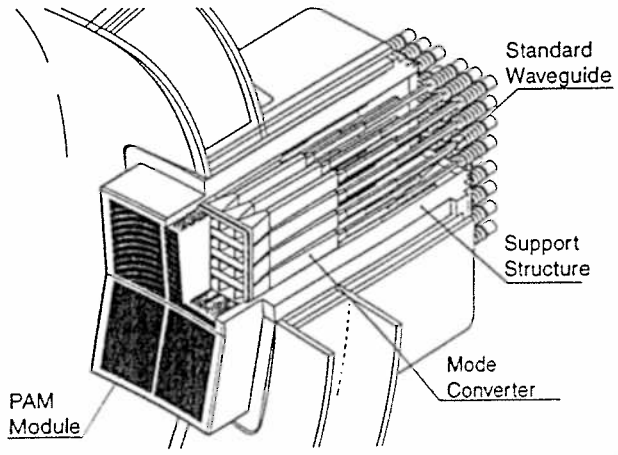

FIG 5. Lower Hybrid Launcher

of mode converters to 48 double-disk, RF windows, isolating the primary vacuum from the secondary one.

The 48 inputs are connected, by means of a set of 24 matched hybrid junctions, and six rectangular-to-four-sector transformers, to the output of six main transmission lines (MTL) made oversized circular wave guide, operated in the TE_{10}° mode at reduced RF losses. Each MTL is fed by 4 klystrons via a combining network (CN) composed of 4 symmetric rectangular-to-sector transformers.. Mode filters to suppress axisymmetrical TE_{0n} modes to damp high order TE_{nm} and TM_{nm} modes. Miter bends are used in the wave-guide.

The LH transmitter layout consists of three stages: a low power solid state RF source (20 dBm) connected to a solid state driver (10 W), followed by the klystron amplifier (1 MW).

7. Conclusions

The design of ITER RF auxiliary heating and current is currently being completed. The design effort has mainly addressed issues related to the in-vessel components, including manufacturing, installation, testing, survival in the reactor environment, plant control and operation, remote handling, and hot cell maintenance. The overall group of RF H&CD systems offers prospects for an efficient, reliable, and flexible service.

8. References

[1] D.J.Hoffman et al, Proc VII Topical AIP Conf., 159, 302 (1987)